Spring 2016

Experimental Analysis of Turbulent Structures and the Effects of Non-Equilibrium on an Axial Vortex

Michael P. Thompson
Old Dominion University

EXPERIMENTAL ANALYSIS OF TURBULENT STRUCTURES AND THE EFFECTS OF NON-EQUILIBRIUM ON AN AXIAL VORTEX

by

Michael P. Thompson
B.S. Applied Physics, Appalachian State University

A Thesis Submitted to the Faculty of
Old Dominion University in Partial Fulfillment of the
Requirements for the Degree of

MASTER OF SCIENCE

AEROSPACE ENGINEERING

OLD DOMINION UNIVERSITY

May 2016

Approved by:

Robert Ash (Director)

Drew Landman (Member)

Shizhi Qian (Member)

ABSTRACT

EXPERIMENTAL ANALYSIS OF TURBULENT STRUCTURES AND THE EFFECTS OF NON-EQUILIBRIUM ON AN AXIAL VORTEX

Michael P. Thompson
Old Dominion University, 2016
Director: Dr. Robert Ash

Examples of the axial vortex include, dust devils, trailing line aircraft wake vortices, and tornadoes. Some of these vortices can prove hazardous to individuals and property. This necessitates that studies be conducted to understand their structure and to attempt to develop mathematical models of the flow physics involved. A wide variety of experimental techniques have been used in the past to study the vortex, with flow visualization and hotwire anemometry being chosen for this experiment. There have been many inadequate mathematical models proposed in the past. The experimental results obtained were compared to the work of Ash, Zardadkhan and Zuckerwar (2011) taking into account the effects of non-equilibrium pressure forces on the flow. Their work used an eddy viscosity model to satisfy closure of the Navier-Stokes equation. The applicability of this model was further accessed in the experiment.

For the purpose of this experiment a bi-wing vortex generator was constructed. The vortex generator was designed without a central body in an attempt to minimize the velocity deficit created by its wake. This was instead replaced with a small cylinder containing a bevel gear system to link the movement of one wing to the other so prices adjustments could be made simultaneously. In the experiment Flow Visualization via smoke injection into the wind tunnel was used to observe the structure of the vortex. These

observations were used to determine which vortex generator and wind tunnel setting yielded the largest most stable vortex. With the vortex generator set at an angle of attack of ±12º hotwire surveys employing a TSI 300 anemometer paired with an X-wire hot-film probe were then conducted on vortices at tunnel settings of 30 m/s and 40 m/s

Velocity profiles consistent with axial vortices were observed in the hotwire surveys. These profiles, when compared to the profiles generated taking into account non-equilibrium pressure effects, indicated that pressure relaxation and therefore non-equilibrium forces had a meaningful effect on the axial vortices. The Reynolds stress data obtained in the experiment also indicated that the Reynolds stress follow a trend consistent with the eddy viscosity model though it was impossible to obtain fully conclusive results due to the x-films inability to obtain the "axial-azimuthal" Reynolds stress correlation. Further study is required to give a more comprehensive view of the effects of non-equilibrium conditions on axial vortices.

This thesis is dedicated to the friends and family who made it possible.

ACKNOWLEDGMENTS

Dr. Robert Ash for serving as my advisor and committee chair

Dr. Drew Landman for serving as a member of my committee

Dr. Shizhi Qian for serving as a member of my committee

Brendan Wiedow, Ken Torro for being a great roommates

Colin Thompson for being a great brother helping with Photoshop

Heather Clifton for programing support.

Nomenclature

α	Angle of hotwire sensing element
Dh	Horizontal vortex diameter
Dv	Vertical vortex diameter
dF	Uncertainty in F
dU	Uncertainty in magnitude of flow velocity
$d\theta$	Uncertainty in flow angle
dE'	Uncertainty in temperature adjusted voltage reading
du	Uncertainty in the x velocity
dv	Uncertainty in the y velocity
$d\bar{u}$	Uncertainty in mean x velocity
$d\bar{v}$	Uncertainty in mean y velocity
$\boldsymbol{\nabla}\Omega$	Gravitational potential
E1	Voltage from channel 1 of the daq
E2	Voltage from channel 2 of the daq
ε	Eddy viscosity
$\dot{\varepsilon_{xy}}$	Strain rate
F	Any function

η_P Pressure Relaxation Coefficient

η_v Bulk viscosity

Γ_0 Circulation of the vortex

K Yaw calibration coefficient

M number of variables in the equation

μ Dynamic viscosity

ν Kinematic Viscosity

ν_{turb} Turbulent Viscosity

ρ Density of the fluid

P Pressure

$P(r)$ Pressure at location a distance from the center of the vortex

P_∞ Far field pressure

ψ Stream function

r Distance from the center of the vortex

r_{core} Radius of the vortex core boundary

R_Γ Circulation based Reynolds number

RH Relative humidity

T_{tunnel} Temperature of the wind tunnel

T_{cal}	Teamprature at hotwire calibration
t	Time since the vortex was created
θ	Angle of the velocity vector
U	Flow velocity magnitude
U_{eff}	Effective cooling velocity
u	X component of velocity
u’	Fluctuations of the X component of velocity
u_m	Measured velocity from the hotwire in the u direction
u_i	Ith component of velocity
$\overline{u_i}$	Ith component of mean velocity
u_i'	Ith component of velocity fluctuations
V	Wind tunnel velocity
v	Y component of velocity
v’	Fluctuations of the y component of velocity
v_m	Measured velocity from the hotwire in the v direction
$\boldsymbol{v}$	Velocity vector
v_θ	Azimuthal velocity
$v_{\theta,max}$	Maximum azimuthal velocity

w	Z component of velocity
w’	Fluctuations of the Z component of velocity
x	Horizontal coordinate direction
x_i	Ith component of position
x-ctr	Horizontal vortex center in relation to tunnel center line
X_i	Variables in an equation
y	Vertical coordinate direction
y-ctr	Vertical vortex center in relation to tunnel center line
$\bar{Z}$	Distance from the vortex generator
z	streamwise coordinate direction

TABLE OF CONTENTS

LIST OF TABLES

LIST OF FIGURES

CHAPTER I

INTRODUCTION

Axial vortices are important fluid phenomena. Examples of axial vortices include trailing line aircraft wake vortices, dust devils, waterspouts, and tornadoes. Understanding the structure of the core region of these vortices is important because of its influence on vortex coherence and lifetime. These vortices can be hazardous to following aircraft in the case of trailing line aircraft wake vortices, and to individuals and structures in the case of tornadoes. The persistence of these vortices contributes to the severity of the hazard they produce. To date, it has not been possible to mathematically model the flow physics needed to accurately predict the strength or the lifetime of these vortices. This is due in no small part to the fact that all of these naturally-occurring vortices are associated with large-scale flows, and thus include turbulent structures. It has also been difficult to garner a sufficient experimental understanding of these vortices because, with the exception of trailing line vortices and vortices generated in wind tunnels, the flows are not fixed to a spatial location, making it difficult to conduct repeatable experiments. In cases where repeatable experiments were possible, several experimental techniques have proved useful. These techniques include flow visualization, Particle Image Velocimetry (PIV), and hotwire anemometry. These techniques allowed the generation of a more comprehensive picture of the vortex structure. The measured velocity profiles were then useful in comparison with mathematical models, such as the Rankine Vortex and the Lamb-Oseen Vortex, to determine their efficacy. For the purposes of this experiment, flow visualization was used to determine the approximate location of the rotational axis of the evolved vortices, their core dimensions and visual indications of the stability of the core region as these axial vortices progressed downstream in a wind tunnel. Hotwire anemometry was then used to resolve detailed velocity profiles. The resulting mean velocity

profiles were compared with those predicted by an exact solution to the Navier-Stokes equations incorporating non-equilibrium pressure contributions derived by Ash, Zardadkhan and Zuckerwar (2011). The vortices produced in the present experiments were turbulent, enabling this investigation to examine the applicability of a simple eddy viscosity turbulence model that was employed in the non-equilibrium theory. Consequently, hot film turbulent Reynolds stress measurements were an important aspect of this research.

1.1 Mathematical Vortex Model

A variety of mathematical vortex models have been developed through the years. The simplest of these models is the Rankine vortex (Rankine, 1869). Rankine assumed that the vortex could be approximated using two zones, a rigidly rotating central core region and an outer region approximated as a potential vortex. The Rankine vortex velocity model is therefore given by:

$$v_\theta(r) = \frac{\Gamma_0}{2\pi r_{core}} \frac{r}{r_{core}} \quad for\ r \leq r_{core}, \tag{1}$$

and

$$v_\theta(r) = \frac{\Gamma_0}{2\pi r} \quad for\ r > r_{core}. \tag{2}$$

The Rankine vortex effectively predicts the azimuthal velocity profile for physical vortices for the two zones; however it is incapable of predicting the transition between the two zones. Because of the shear stress discontinuity between the juncture of the two zones, the model equations are not physically realistic. Observed azimuthal velocity profiles should closely match the azimuthal velocity profile generated by these equations away from the core boundary. However because of the discontinuous nature of the velocity profile, the velocity structure will differ greatly in close proximity to the core boundary. The Rankine vortex is also only valid for steady flow, meaning it cannot account for the effects of turbulence on the vortex or time periodic events such as the ingestion of fluid into the core region from the outer "potential flow" region. The core region is

modeled as a rigidly rotating solid body which is inconsistent with experimental observations.

The Lamb-Oseen vortex was developed assuming that a potential vortex, with its infinite centerline velocity, was suddenly injected into a viscous fluid, and allowed to decay over time due to viscous effects (Lamb, 1932). This theoretical solution generates a continuous, unsteady function predicting the azimuthal velocity, immediately after the introduction of a line vortex line and is given by:

$$v_\theta(r,t) = \frac{\Gamma_0}{2\pi r}\left[1 - e^{\left(\frac{-r^2}{r_{core}(t)}\right)}\right] \tag{3}$$

where the core radius varies with time according to

$$r_{core}(t) = \sqrt{4\nu t} \tag{4}$$

The drawbacks to this model are its time dependence and the limiting singularity at the center line. Because of its continuous nature, this model should be better at predicting the velocities around the core boundary, although it still tends to greatly overestimate the size variation. Again, like the Rankine vortex, the Lamb-Oseen Vortex cannot properly deal with unsteady phenomena such as turbulence or other time dependent flow structures. Thus it will only be valid for average velocity profiles.

Ash, Zardadkhan and Zuckerwar (2011) considered the influence of non-equilibrium pressure forces on the flow behavior of a simple axial vortex. This effect emerges when Hamilton's Principle of Least Action is employed to introduce non-equilibrium thermodynamic effects. Their variational equations incorporated conservation of mass, energy and species constraints, and resulted in non-equilibrium pressure and density contributions to the Navier-Stokes equation as.

$$\rho\frac{D\boldsymbol{v}}{Dt} = -\boldsymbol{\nabla}\left[P - \eta_P\frac{DP}{Dt}\right] - \rho\boldsymbol{\nabla}\Omega + \boldsymbol{\nabla}\left[\left(\eta_v - \frac{2}{3}\mu\right)\boldsymbol{\nabla}\cdot\boldsymbol{v}\right] + \boldsymbol{\nabla}\times(\mu\boldsymbol{\nabla}\times\mathbf{v}) + 2[\boldsymbol{\nabla}\cdot(\mu\boldsymbol{\nabla})]\boldsymbol{v} \tag{5}$$

In index notation, assuming that the pressure relaxation coefficient, volume viscosity and dynamic viscosity are constant, and neglecting body force, the ith component of the conservation of momentum equation becomes

$$\rho\frac{\mathrm{Du_i}}{\mathrm{Dt}} = -\frac{\partial \mathrm{P}}{\partial \mathrm{x_i}} + \eta_\mathrm{P}\frac{\mathrm{D}}{\mathrm{Dt}}\left(\frac{\partial \mathrm{P}}{\partial \mathrm{x_i}}\right) + \mu\frac{\partial^2 \mathrm{u_i}}{\partial \mathrm{x_i^2}} + \eta_\mathrm{P}\left[\frac{\partial \mathrm{u_k}}{\partial \mathrm{x_i}}\frac{\partial \mathrm{P}}{\partial \mathrm{x_k}} - \frac{\left(\eta_\mathrm{v} + \frac{1}{3}\mu\right)}{\eta_\mathrm{P}}\frac{\partial}{\partial \mathrm{x_i}}\left(\frac{1}{\rho}\frac{\mathrm{D}\rho}{\mathrm{Dt}}\right)\right] \tag{6}$$

The bracketed term in that equation has been linked to the production of sound in incompressible flows. While that effect has not been isolated, when the bracketed expression is multiplied by the pressure relaxation coefficients observed in air, the term becomes negligibly small. Simplifying the equation to

$$\rho\frac{Du_i}{Dt} = -\frac{\partial P}{\partial x_i} + \eta_P\frac{D}{Dt}\left(\frac{\partial P}{\partial x_i}\right) + \mu\frac{\partial^2 u_i}{\partial x_i^2} \tag{7}$$

Ash et al.(2011) examined a steady, incompressible, axial vortex where the only non-zero component of velocity was the azimuthal component, whose solution was given by.

$$v_\theta(r) = \frac{\Gamma_0}{\pi}\frac{2^{\frac{3}{2}}}{R_\Gamma\sqrt{\nu\eta_P}}\frac{\frac{r}{r_{core}}}{\left(\frac{r}{r_{core}}\right)^2 + 1} \tag{8}$$

or

$$v_\theta(r) = 2v_{\theta,max}\frac{\frac{r}{r_{core}}}{\left(\frac{r}{r_{core}}\right)^2 + 1} \tag{9}$$

Equation (9) was found to be the same form as the widely used empirical fit for mean aircraft trailing line vortex velocity profiles, identified by Burnham and Hallock.(1982). Ash et al (2011)

found that as the pressure relaxation coefficient was decreased toward zero, the azimuthal velocity tended to infinity on the axis and the core radius (where the azimuthal velocity was maximum) tended to zero, resulting in a potential vortex. For large values of the pressure relaxation coefficient, the solution approached a rigidly rotating body.

Ash et al (2011) utilized the experimental velocity and pressure measurements in dust devils obtained by Sinclair (1969) to infer differences between the effects of pressure relaxation and turbulence on the mean vortex velocity structure. Squires (1965) had utilized an eddy viscosity model in estimating the influence of swirl Reynolds number on the structure of high-Reynolds number trailing line aircraft vortices. Experimentally determined turbulence statistics have been obtained in order to determine how Reynolds stress distributions in the vicinity of the vortex core can be correlated with the mean azimuthal velocity profile in a manner similar to the implied eddy model to assess its applicability. That comparison will discussed later.

Since the theory was restricted to a constant density fluid, the exact solution allowed a direct integration to predict the pressure distribution within the vortex. Given that P_∞ is the far field (ambient) pressure, the radial variation in pressure is given by:

$$P_\infty - P(r) = 4\frac{\mu}{\eta_P}\frac{1}{\left(\frac{r}{r_{core}}\right)^2 + 1} \tag{10}$$

In the vortex core, the predicted magnitude of this pressure deficit is twice the magnitude of the pressure deficit predicted using the incompressible Bernoulli equation at the radius of the maximum azimuthal velocity. The difference is attributed to the Bernoulli equation predicting that the centerline pressure of a rigidly rotating vortex returns to the far field pressure while the pressure

relaxation theory predicts that the pressure continues to decrease, and the minimum pressure occurs on the vortex centerline.

Using American National Standards Institute acoustical reference data, Zuckerwar and Ash (2009) estimated the pressure relaxation coefficient in air as a function of temperature and relative humidity. That behavior is compiled in Table 1. In addition to the dust devil data, the authors employed experimental vortex data from turbulent aircraft and wind tunnel trailing line vortex experiments to validate their theory. Those comparisons are summarized in Table 2. The authors assumed that turbulent effects could be incorporated using an eddy viscosity model that varied linearly with circulation, similar to Squire (1965). However, they stated that this assumption required experimental verification.

RH (%)	0	20	40	60	80	100
Temperature (K)						
273.15	43.38	2.58	1.31	0.88	0.66	0.53
283.15	50.52	1.78	0.91	0.61	0.46	0.37
293.15	58.23	1.28	0.64	0.43	0.32	0.26
303.15	66.50	0.93	0.47	0.31	0.23	0.18
313.15	75.31	0.69	0.34	0.23	0.17	0.13
323.15	82.64	0.52	0.26	0.17	0.12	0.10

Table 1 Estimates of the pressure relaxation coefficient with temperature and relative humidity, based on Acoustic data (ANSI 1995; Ash et al. 2011)

Experiment	$\Gamma_0\left(\frac{m^2}{s}\right)$	R_Γ	$r_{core}(m)$	$v\left(\frac{m}{s^2}\right)$	$\eta_P(\mu s)$
NASA C-130 (Delisi et al. 2003)	200	2,100,000	0.34	15.1×10^{-6}	0.0134
NOAA B-757 (Garodz and Clawson 1993)	40.55 (16 s)	380,500	0.061	16.96×10^{-6}	0.0121
9° C; 74% RH					(0.53)
NOAA B-757 (Garodz and Clawson 1993)	35.41 (35 s)	330,200	0.274	17.07×10^{-6}	0.323
10.5° C; 52% RH					(0.72)
NOAA B-767 20	37.46 (59 s)	356,800	0.091	16.71×10^{-6}	0.0311
7° C; 51% RH					(0.84)
NOAA B-767 (Garodz and Clawson 1993)	43.53 (25 s)	381,600	0.244	18.16×10^{-6}	0.180
21° C; 51% RH					(7.0)
Piper Cherokee (McCormick Tangler, and Sherrier 1968)	10.2	105,000	0.02, 0.03	15.4×10^{-6}	0.0990
McAlister and Takahashi (1991)	8.5	81,600; 51,000	0.009	15.6×10^{-6}, 15.6×10^{-6}	0.0308, 0.177
Graham (1996)	2.2	23,200		15.2×10^{-6}	0.0803

Table 2 Pressure relaxation coefficient estimate in vortex experiments (Ash et al 2011**)**

Abuharaz and Ash (2014) expanded upon this work utilizing a state variable model based on the equations of motion derived by Ash, Zardadkhan and Zuckerwar (2011). The state variable stability model inferred maximum observed turbulent velocities, magnitude of pressure

fluctuations, turbulence intensities and the radial locations of regions expected to exhibit the most intense turbulence. That model identified three vortical flow zones: (1) a laminar region near the vortex axis; (2) an unsteady, turbulent region in close proximity with the maximum mean azimuthal velocity; and (3) an outer region that displayed the characteristics of a potential vortex. It was found that non-equilibrium pressure effects tended to strengthen the vortex resulting in larger pressure differences between the core and outer region. This model served as a useful basis on which to plan the tests conducted in this experiment, since the theory provided a basis for estimating the frequencies of turbulence that could be observed.

1.2 Turbulence Modeling

Turbulence, the self-generating, irregular, random, and unsteady fluctuations in fluid motion, has proven to be a difficult phenomenon to mathematically describe. In the study of turbulence, it is necessary to formulate a means of closing the Navier-Stokes equations. The simplest way to achieve this is the introduction of eddy viscosity (Prandtl 1925). Eddy viscosity closes the Reynolds averaged Navier-Stokes equations by assuming that the Reynolds Stresses can be related to gradients in the mean flow velocities. Specifically, if the Reynolds-averaged Navier-Stokes equations (RANS) are written:

$$\frac{D\overline{u_J}}{Dt} = \nu\nabla^2\overline{u_J} - \frac{\partial\left(\overline{u_i'u_J'}\right)}{\partial x_i} - \frac{1}{\rho}\frac{\partial\bar{p}}{\partial x_j}, \tag{11}$$

and the Reynolds stress terms are modeled assuming that

$$-\overline{u_i'u_j'} = \varepsilon\left(\frac{\partial\overline{u}_\iota}{\partial x_j} + \frac{\partial\overline{u}_J}{\partial x_i}\right) - \frac{1}{3}\overline{u_\iota u_\iota}\delta_{ij} \tag{12}$$

Combing these two equations results in an essentially laminar flow model, given by

$$\frac{D\overline{u}_J}{Dt} = \frac{\partial}{\partial x_i}\left(\nu_t\left[\frac{\partial\overline{u}_\iota'}{\partial x_j} + \frac{\partial\overline{u}_J'}{\partial x_i}\right]\right) - \frac{1}{\rho}\left(\bar{p} + \frac{1}{3}\overline{u_\iota u_\iota}\delta_{ij}\right) \tag{13}$$

where the turbulent viscosity, ν_t, is

$$v_t = v + \varepsilon \tag{14}$$

For an isolated vortex, Squire (1965) proposed that this eddy viscosity could simply be based on the characteristic vortex circulation (Γ), i.e.

$$\varepsilon = a\Gamma \tag{15}$$

A goal of this thesis was to test the applicability of this model via experiment.

1.3 Experimental Axial Vortex Observations

Burnham and Hallock (1982) performed multiple observation campaigns characterizing actual aircraft wake vortices in the vicinity of airports. Their observations yielded an empirical model for the azimuthal velocity profiles given by

$$v_\theta(r) = \frac{\Gamma_0}{2\pi r}\frac{1}{1+\left(\frac{r}{r_{core}}\right)^2} \tag{16}$$

This correlation was the best curve fit for the velocity profiles compiled through years of characterization experiments. Since the Burnham-Hallock Vortex is an empirical fit generated from data based on actual aircraft wake vortices observations, this model will most closely match their gathered experimental data. However, since the method of vortex generation for the experiments reported in this thesis is different, the structure of the experimentally-generated vortex will likely be different, contributing to a difference between this model and observed velocity profiles.

Bandyopadhya et al (1991) used hotwire anemometry to study the effect of free stream turbulence on the behavior of the core region of an axial vortex generated with a bi-wing generator in a wind tunnel, similar to the present experiments. They found that the inner core did not rotate like a solid body, as assumed in the Rankine vortex model, but contained instead rotating regions

with low turbulence levels that periodically ingested fluid from outside of the core region and partially re-laminarized the ingested fluid.

Romeos (Romeos, et al, 2009, Romeos and Panidis, 2010) studied bi-wing-generated axial vortices in a wind tunnel similar to the setup employed by Bandyopadhya et al (1991), but without a wake-generating center body. Their detailed hotwire anemometry measurements focused mainly on the early stages of vortex development. In the initial stage of vortex formation, they observed two co-rotating vortices shed from both inner wing junctures. These vortices, when in close proximity to one another, tended to influence each other, beginning to braid together into a single vortex. It was again observed that Rankine's solid body rotation model was unsuitable in characterizing the action of these vortices.

Downstream from the vortex development zone, Romeos and Panidis (2010) probed cross sections of the vortex flow field at several chord length distances downstream from the vortex generator, in order to study the evolution of the primary vortex as it progressed downstream. The area occupied by the vortex cores was associated with a large streamwise velocity deficit, and the largest measured velocity deficit was approximately 55% of the wind tunnel free stream velocity, as observed 0.3 chord lengths behind the bi-wing generator. Farther downstream, the axial velocity deficit had diminished to approximately 25% of the free stream velocity. Two distinct regions of minimum velocity were observed at distances between 0.3 and one chord length behind the vortex generator, indicating that the co-rotating vortices generated by the two wing junctures had not yet merged into the single vortex that is observed farther downstream. Farther downstream, there is only one region of minimum axial velocity, relative to the wind tunnel velocity, indicating that the two shed vortices have merged into a single vortex. Initially, the merged vortex cross section had

an elliptical shape, evolving subsequently into an approximate circular streamline pattern at the downstream station that was farthest from the bi-wing generator.

1.4 Hot-Film Anemometry

Hot-wire anemometry was first employed in the United States by H.L. Dryden and A.M.Kuethe (1929). They have credited J.M. Burgers of the Netherlands with the early development of this technique. This measurement technique has been used for many years to measure unsteady fluid velocities and subsequent turbulence statistics. Hot wire anemometers rely on velocity- and temperature-dependent convective heat transfer and predictable sensor resistance variation with temperature to establish a relationship between instantaneous fluid velocities and the voltage or current required to maintain a heated sensor element in a cooler flowing fluid.

The two primary operating modes employed by hotwire anemometers are constant current anemometry (CCA) and constant temperature anemometry (CTA). CCA adjusts the applied voltage to control the current flow through the sensor wire in order to maintain a constant current. As a result, when the fluid velocity fluctuates, the wire temperature fluctuates and the associated sensor resistance changes, requiring that the applied voltage be adjusted in order to maintain a constant current. CTA maintains the temperature (wire resistance) at a constant value by varying the voltage and associated current to maintain a constant resistance. Hence, the cooling rate changes as a result of velocity changes requiring the sensor current to change in order to maintain a constant resistance. CTA systems are considered to be superior to CCA systems since that approach tries to maintain a constant sensor temperature and automatically accounts for thermal inertia, eliminating the need for complicated dynamic calibrations.

Two common types of sensor elements are utilized in hot-wire anemometry. Metallic hot wire sensors are fabricated typically from a single strand of tungsten or platinum-coated tungsten

wire. Hot film sensors are fabricated by coating a small-diameter, cylindrical ceramic or quartz substrate with a conductive material such as platinum. The advantage of the hot film sensor design is that it produces a more resilient sensing element that is less susceptible to destruction or degradation from particle impacts. Hot film sensors are also easier to clean when contamination occurs. However, metallic hot wire sensors generally exhibit higher frequency sensitivity to velocity fluctuations than do hot film sensors. Hence, for applications characterized by high frequency phenomena, including high noise levels or, when the sensor must be positioned in close proximity to a surface, metallic hot wire sensors are preferred.

Bruun (1995) has described the operation of many different types of sensor probes and probe configurations. The simplest probe design is a single wire, mounted between two support pins. Single wires can only detect unsteady velocities that are perpendicular to the axis of the sensor wire, regardless of the orientation of the velocity vector in that plane. If there is a primary flow direction, a single-axis sensor can be aligned to measure that velocity component. The second most common sensor configuration is the "X-wire" geometry, in which two sensor wires (or films) are mounted on pins so that they are angled at plus and minus 45 degrees with respect to the primary flow direction. X-wires can measure two velocity components and are sensitive to velocity fluctuations in both directions. X-film sensors were used in this experiment. Three-wire probes are sensitive to velocity fluctuations in all three flow-directions, while multi-sensor probes are used in a wide variety of configurations to attempt to determine the velocity gradients in all three coordinate directions. (Bruun 1995)

In recent years, larger multi-sensor arrays of hotwires have been used to acquire data. These arrays are configured employing various geometrical patterns and numbers of sensors. The use of these larger arrays of wires has usually been prompted by the need to study instantaneous spatial

derivatives of the velocity and other flow characteristics, such as vorticity. The number of sensing wires in these arrays ranges from four sensors to more than 20, although on average they contain 11 or 12 (Romeos, Lemonis, Panidis, and Papailiou 2009; Romeos and Panidis 2010; Vukoslavcevic and Wallace 2013). The design of these multi-sensor systems is constrained primarily by spatial resolution and accuracy. To increase spatial resolution, the sensors must be arrayed together as closely as possible; however due to interactions between the separate wires, the overall accuracy can drastically decrease. The ideal balance of resolution with accuracy appears to be at a separation of between 2 and 4 Kolmogorov length scales.(Romeos, Lemonis, Panidis, and Papailiou 2009) Comparisons of data generated by a conventional X-wire and a 12-wire array yielded results that were considered to be the same within the uncertainty of the devices.

A major disadvantage in employing hotwire probes to characterize axial vortices is an inability to deal with large out-of-plane velocities (Romeos, Lemonis, Panidis, and Papailiou 2009). Vukoslavcevic and Wallace (2013) demonstrated with direct numerical simulation of a channel flow, an 11-sensor probe intended to measure velocity gradients. That probe was called an xp probe, and was found to be most suitable for that type of measurement. The sensors were arranged so that they resembled an array of three X-wires at the vertices of a triangle with five single-wire sensors, oriented to obtain the third component of velocity as seen in Figure 1 and Figure 2. They also found that just four sensing wires arranged so that an X-wire with a single wire on each side, along the out of plane axis, was able to capture the velocities and therefore the Reynold stresses accurately

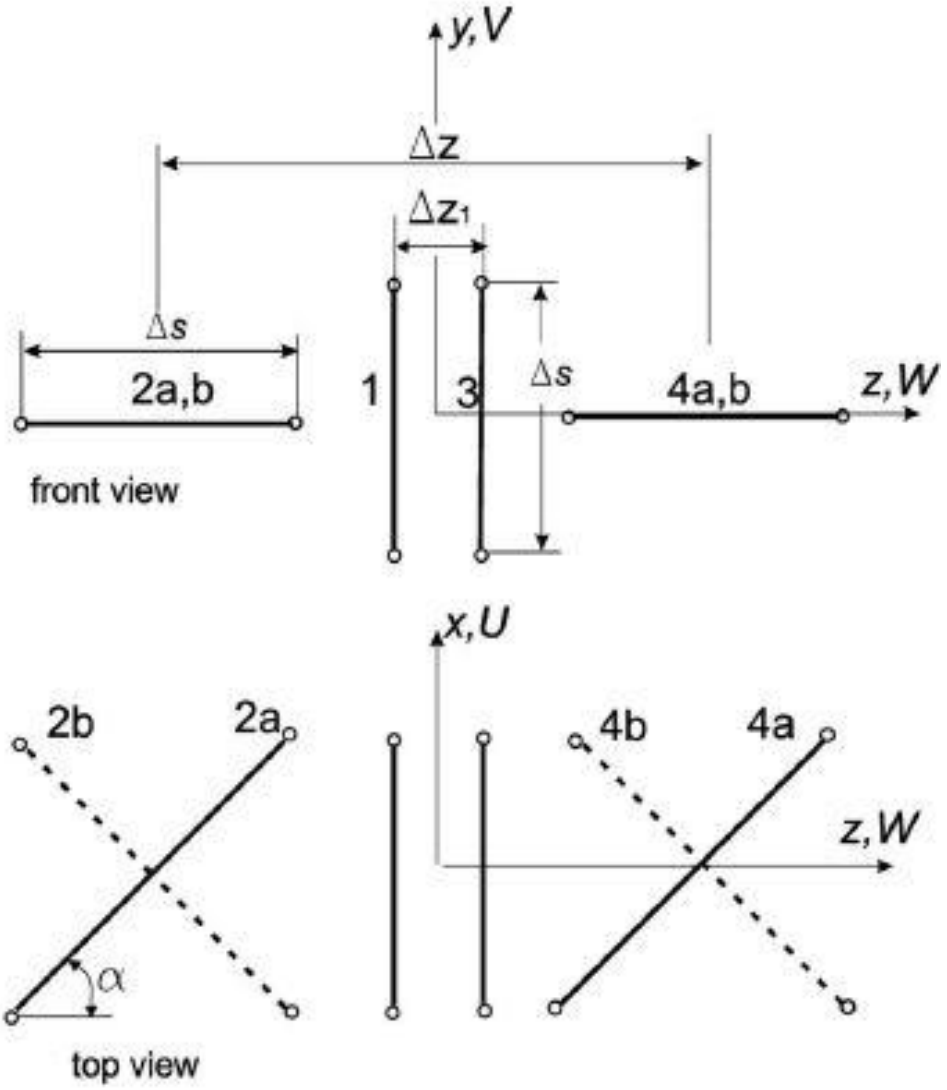

Figure 1 XP probe configuration (Vukoslavcevic and Wallace 2013)

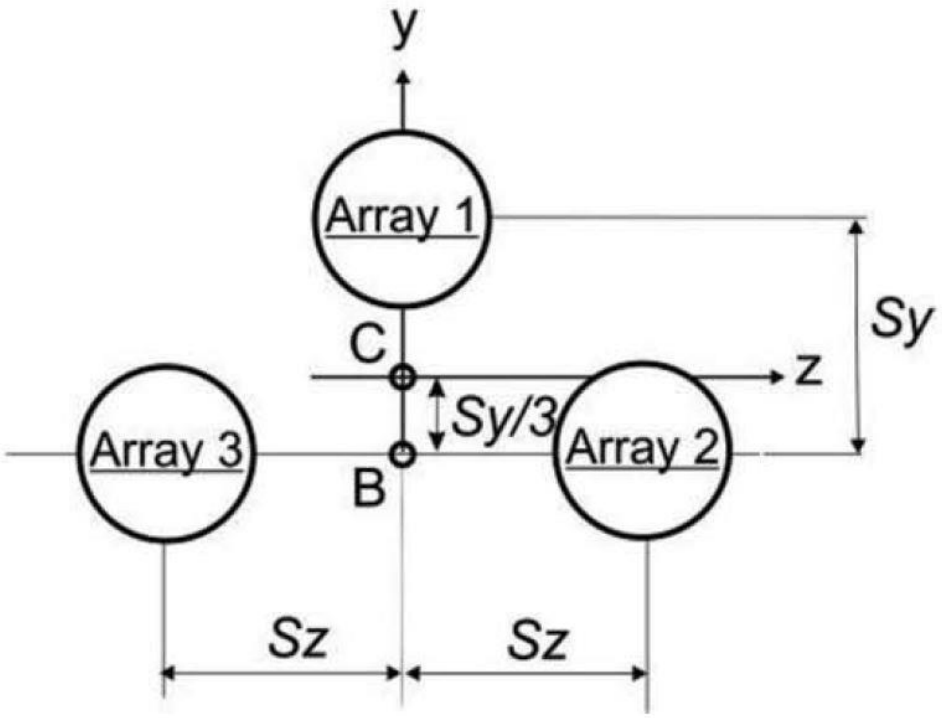

Figure 2 Arrangement of Xp-probe arrays (Vukoslavcevic and Wallace 2013)

In this experiment, an X-wire sensor geometry was chosen since the primary concern was the mean velocity distributions and Reynolds stresses. Romeos showed that results using an X-wire survey were the same as those acquired with a four-sensor array within the uncertainties of the apparatus (Romeos, Lemonis, Panidis, and Papailiou 2009). Although it was determined later that measuring the third (out-of-plane) component of velocity would have enabled isolation of the radial-azimuthal component of the Reynolds stress it was not feasible to construct or purchase an appropriate three-wire or four-wire probe. In an attempt to overcome this limitation, the hotwire surveys were repeated with the X-wire rotated by 90 degrees from the first survey to capture the third component of velocity.

High turbulence levels are known to distort X-probe velocity measurements (Hinze, 1975). These errors, called crossflow errors, are induced by the cooling effects from unsteady fluid motion along and transverse to the sensing element axes. The axial vortices produced in this study include a large axial velocity component resulting from the wind tunnel flow. When the X-probe is oriented to measure the axial and radial velocity components in the vicinity of the vortex rotational axis, where the radial velocity component must be zero, the mean rotational and axial turbulent velocity components can produce large mean velocity errors. In an effort to estimate the actual radial velocities in these experiments, a method similar to that of Shabbir, Beuther, George (1995) was developed and employed.

1.5 Flow-Visualization

In experimental fluid dynamics it is desirable to make a normally transparent fluid flow visible for observation. This is done with one of two goals, the first of which would be to observe the interaction of solid bodies with the fluid flow; while the second goal is to study the entire flow field (Merzkirch 1974, 1979, 1987). Visualizing surface flow patterns is often accomplished by introducing a substance that will interact with the flow while remaining attached to the surface of the object. This substance could be a dyed oil, spread over the surface. Another approach is to attach one end of a piece of yarn or string to the surface acting as tufts to indicate the flow direction along the surface. Other, more advanced methods detect local mass transfer or heat transfer from a surface produced by the flow (Maltby and Keating 1962; Settles and Teng 1983). Whole flow field visualization is achieved by introducing some form of tracer particle in the fluid flow. This can be achieved by introducing a die in water flows, or smoke in air flows. In the case of airflows, such as in the present experiment, smoke can be generated in multiple ways such as vaporizing mineral oil, combusting straw or tobacco, or generating a mist via chemical reaction (Brown; 1953;

Maltby and Keating 1962 b; Mueller 1980). A single path line through the fluid can be traced if the smoke is generated at a single point upstream from the desired observation zone. In a closed circuit wind tunnel the flow can become saturated with smoke in most cases, rendering flow visualization useless. However, in the present experiment, saturating the wind tunnel flow with smoke proved to be useful. Employing a laser sheet to illuminate an axial wind tunnel cross section, made it possible to determine where the smoke was ejected from the core region of the vortex. By locating the "smoke hole" at a given axial wind tunnel location, it was possible to identify and isolate the desired hotwire survey region.

CHAPTER II

EXPERIMENTAL SETUP

Experiments were conducted in the Old Dominion University Low Speed Wind Tunnel, which will simply be called the *wind tunnel* in the remainder of this thesis. The wind tunnel layout, shown schematically in Figure 3, is a closed-circuit design without active temperature control. The wind tunnel is powered by a 125 horsepower (93 kW) variable frequency, speed-controlled AC electric motor and incorporates two test sections. Wind speed control is achieved by varying the frequency of the voltage supplied to the motor, utilizing a Labview-based speed control program. The larger, low-speed test section is seven feet (2.13 m) wide by eight feet (2.44 m) high, extends seven feet (2.13 m) in the flow direction and is separated from the high-speed test section by a contoured contraction. The large-scale, low-speed test section is capable of maintaining flow speeds no greater than 12 m/s, with associated turbulence levels of 0.8 %; the high-speed test section can maintain flow speeds ranging from 12 m/s up to 55 m/s, with turbulence levels of 0.2%. The high-speed test section was utilized in these experiments, and is four feet (1.219 m) wide by three feet (0.914 m) tall and extends eight feet (2.44 m) in the flow direction.

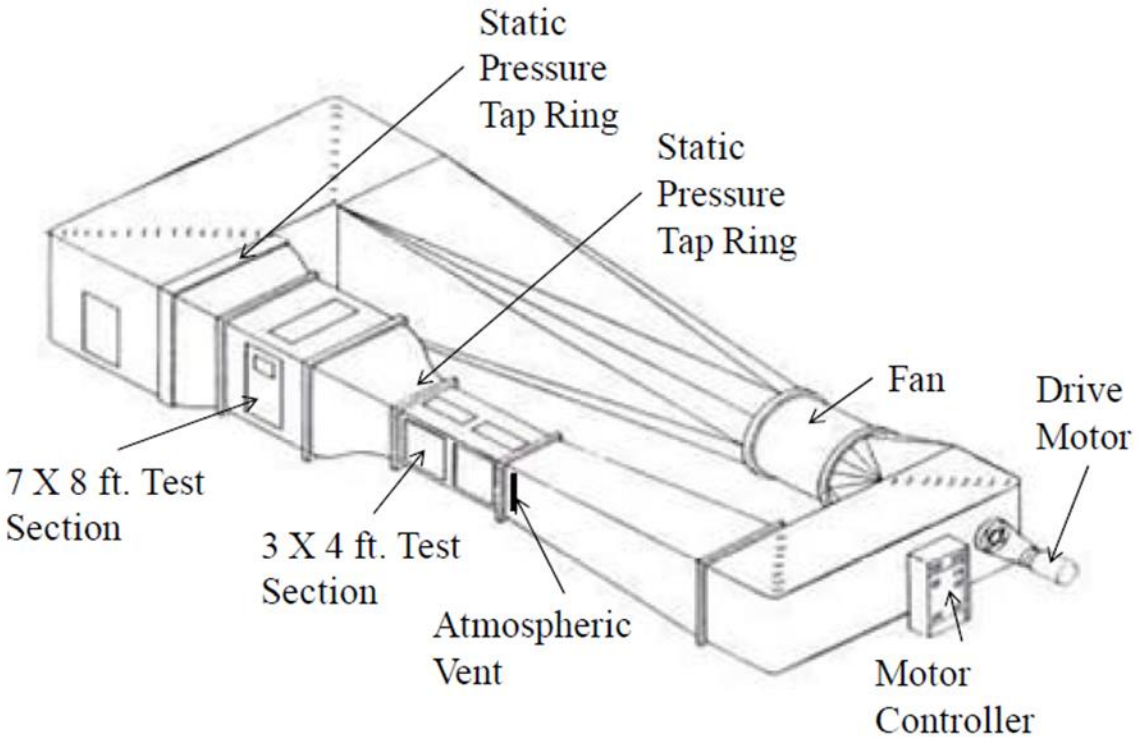

Figure 3 Schematic representation of the Old Dominion University Low Speed Wind Tunnel

A computer-controlled three-axis traverse system, available for operation within the high-speed test section, was employed in these experiments. The traverse system can be controlled to effect position adjustments of one millimeter or less in all three traverse-directions. The traverse system utilizes *MTS Temposonics* position transducers, capable of measuring position differences of 0.0025 mm.(MTS 1989, 2014). Traverse system position control was achieved utilizing a *National Instruments* SCXI 1160 relay module and an SCXI 1324 terminal block, coupled with Labview software.

2.1 Vortex Generator Design

Preliminary tests were performed employing a bi-wing vortex generator that was designed and fabricated by an undergraduate engineering capstone design team. That vortex generator had a cylindrical center body with a spherical nose and a streamlined tail. However, the airfoil angle-of-attack could not be adjusted in a repeatable manner, and the resulting axial vortex developed rather slowly, as indicated by large axial velocity deficits measured in the vortex core region throughout the wind tunnel test section. It is possible that the axial wake flow deficit region, produced by the center body, was responsible for the slow axial vortex development. On that basis, a new, adjustable bi-wing vortex generator capable of producing repeatable angles of attack was needed, in order to vary vortex strength and assess influences of bi-wing configuration and wind tunnel speed on the overall development and vortex structural behavior. The new bi-wing vortex generator, designed and fabricated as part of this thesis, will be described herein.

The primary factors considered in the new design were ease of angle-of-attack adjustment and requisite repeatability. NACA 0012 airfoils were selected for the new design because of their common availability and the fact that they don't produce a pitching moment about the quarter-chord in the range of angles-of-attack that were of interest in this study. Although an instrumented center body may be required to measure the static pressure along the vortex centerline, or to minimize the axial velocity deficit, the bi-wing generator that was employed successfully by Romeos et al.(2009, 2010) did not incorporate a center body, and the data they produced was considered to be of acceptable quality. A bevel gear system, shown in Figure 4, one inch long (25.4 mm) and one half inch (12.7 mm) in diameter was incorporated in the design, so that adjustment of the upper airfoil angle-of-attack produced an equal, but opposite angle-of-attack adjustment for the lower airfoil. The vortex generator mount, shown in Figure 4, includes setscrews

on each side of the airfoils, in order to maintain the desired angle-of-attack setting. The entire bi-wing generator was mounted in the wind tunnel as shown in Figure 3.

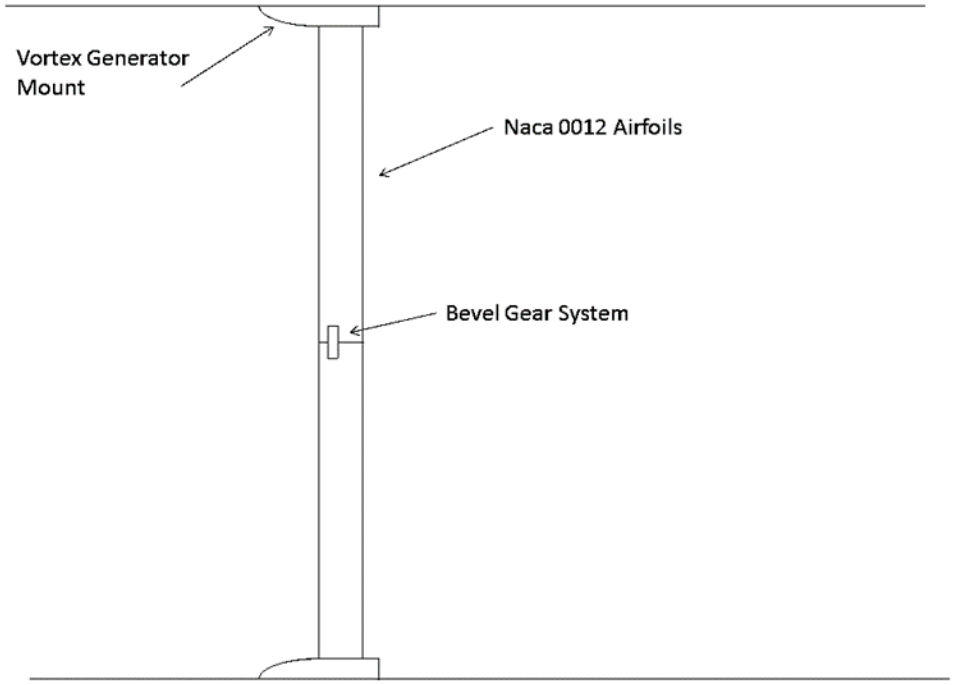

Figure 4 Vortex Generator installation in test section

2.2 Hotfilm Setup and Calibration

The hot film anemometer employed in these experiments was a TSI IFA 300 unit, utilizing TSI 1240-20 X-film probes. Even though the sensors were platinum-coated quartz filaments, it is common practice to refer to these transducers as "X-wires" and that term will be employed interchangeably in this discussion. The anemometer was controlled using LabVIEW software

through a National Instrument data acquisition card (DAQ) paired with a National Instruments BNC-2110 terminal block.

Two TSI 1240-20 X-wire probes were calibrated at NASA Langley Research Center (LaRC) utilizing the LaRC anemometer calibration facility (Jones 1994). That calibration facility consisted of a small, open-jet wind tunnel, incorporating air flow velocity, density, and total temperature control. Air from the 300 PSI (2 MPa) facility air supply, reduced to 100 PSI (0.7 Mpa) utilizing two control valves, provided the calibration flow. Fine velocity adjustments were made using a third control valve located upstream from a settling chamber. The settling chamber contained three screens to reduce flow turbulence. Interchangeable nozzles could be employed as flow contractions, thus varying the calibration speeds. The calibration tests supporting the present study utilized the LaRC three quarter inch diameter (19 mm) subsonic nozzle. A resistance temperature detector (RTD) and static pressure tube were positioned in the mouth of the nozzle exit to measure the calibration air temperature and static pressure. The calibration data were acquired using a National Instrument high speed A/D converter at the LaRC facility.

Calibration of the X-wires was a three-step process. The first calibration matrix was produced by measuring the voltages required to maintain constant temperatures for calibration velocities ranging from 1 to 70 m/s, while the X-probe was aligned so that the flow direction was at ±45 degrees with respect to the axes of each of the two sensing elements. This arrangement resulted in a flow that was solely perpendicular to one of the two sensitive normal directions. The calibration air flow temperature was monitored and controlled to ensure near-constant air temperature during testing. A second calibration matrix was produced employing constant flow velocities while the X-probe axis was varied over a range of angles along the axis of the second sensitive direction, ranging from -30^{o} to +30^{o}, relative to the direction of flow, while controlling

the air temperature. The resulting calibration matrices were used to construct empirical models for the magnitude of the flow velocity vector and its orientation angle with respect to a horizontal (stream wise) axis. The first empirical model related the measured voltages to the magnitude of the velocity vector (U); the second related the angular orientation of the velocity vector to the X-probe axis (θ).

Designating the measured voltage from the sensing element connected to channel 1 of the DAQ as E1, and the other sensing element connected to channel 2 of the DAQ as E2, fourth-order regression equations were developed for the velocity magnitude (U) and the flow angle (θ). The velocity correlation was represented

$$U = -102.09148 + 84.23043E_1 + 186.98250E_2 - 230.04044E_1E_2 + 29.20907E_1^2 - 57.10394E_2^2 + 104.87856E_1^2E_2 + 0.65039E_2^2E_1 - 34.54407E_1^3 + 30.86361E_2^3 - 122.33950E_1^2E_2^2 + 64.47648E_1^3E_2 + 78.38884E_2^3E_1 - 11.19545E_1^4 - 22.22053E_2^4 \quad (17)$$

The instantaneous flow angle correlation was represented using:

$$\theta = 139.41006 - 1940.40154E_1 + 1572.11E_2 + 165.63895E_1E_2 + 1503.55790E_1^2 - 1324.98385E_2^2 + 913.30708E_1^2E_2 - 978.19664E_2^2E_1 - 813.68172E_1^3 + 744.38795E_2^3 - 278.39448E_1^2E_2^2 + 76.67594E_1^3E_2 + 302.84769E_2^3E_1 + 70.56388E_1^4 - 152.90984E_2^4 \quad (18)$$

The response surfaces created by the calibration equations are plotted in Figures 5 and 6, incorporating the model points used in generating the correlation equations for U and θ, respectively.

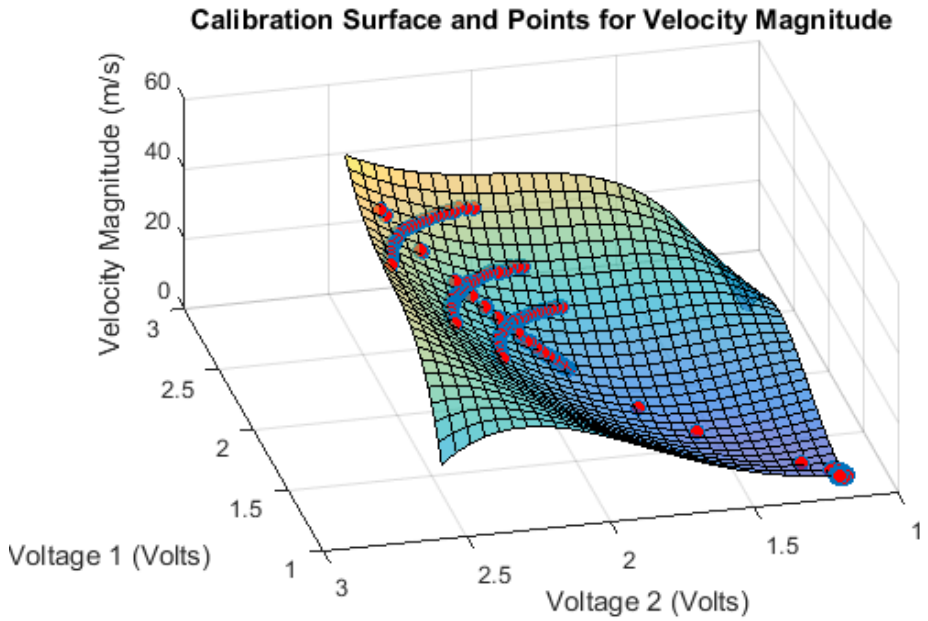

Figure 5 Response surface with model points plotted for the velocity magnitude U. Experiments conducted inside region of the response surface that was investigated in calibration

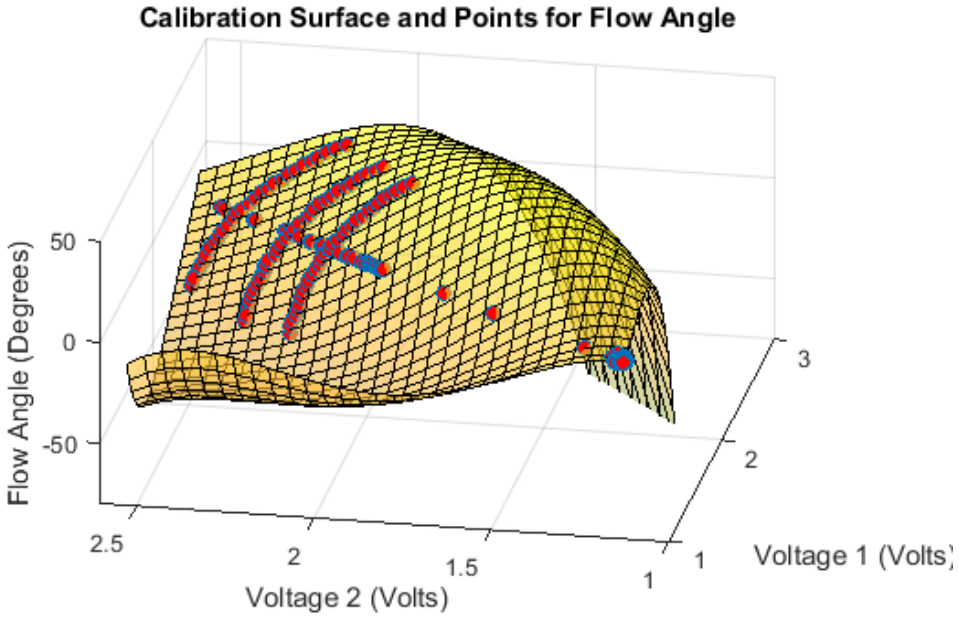

Figure 6 Response surface with model points plotted for the flow angle θ. Experiments conducted inside region of the response surface that was investigated in calibration.

A third calibration matrix was produced in the ODU low-speed wind tunnel, employing constant flow velocities with the probe axis aligned with the flow, while varying the air temperature between 20 ºC and 38 º C. This matrix was employed to produce a linearized wind tunnel temperature correction model, equation (19), for the anemometer output voltages at each wind tunnel speed setting. The slopes of these temperature correction equations were then employed to correct the voltage output so that the measured data could be related directly to the temperature at which the probe was calibrated. This was an important consideration since the wind tunnel temperature could not be controlled.

$$E' = m(T_{cal} - T_{tunnel}) - E_m \tag{19}$$

2.3 Flow Visualization

In order to obtain repeatable hotwire survey data, it was necessary to ascertain the spatial location and stability of the vortex rotational axis within the wind tunnel test section. That was accomplished using flow visualization heated mineral oil smoke. Smoke could also be employed to investigate the spatially-varying core behavior, since the central region of the core ejects the smoke particles, creating a visible smoke-free "hole." In that way it was possible to determine the approximate location where the vortex transitioned from a near-rigidly-rotating central core region to an outer potential flow region. In addition, it was necessary to observe the dynamic behavior of the vortex core region and assess visually the degree to which the local core region oscillated. Undesirable dynamic core axis behavior could be avoided utilizing flow visualization over the expected speed and angle-of-attack setting range.

A series of flow visualization tests were conducted. As shown in Figure 7, the ejected smoke region around the vortex axis was nearly free of smoke, making it possible to employ a

solid state laser and cylindrical lens to produce an illuminated laser sheet spanning different wind tunnel test section cross sections, isolating the smoke-free core region of the vortex.

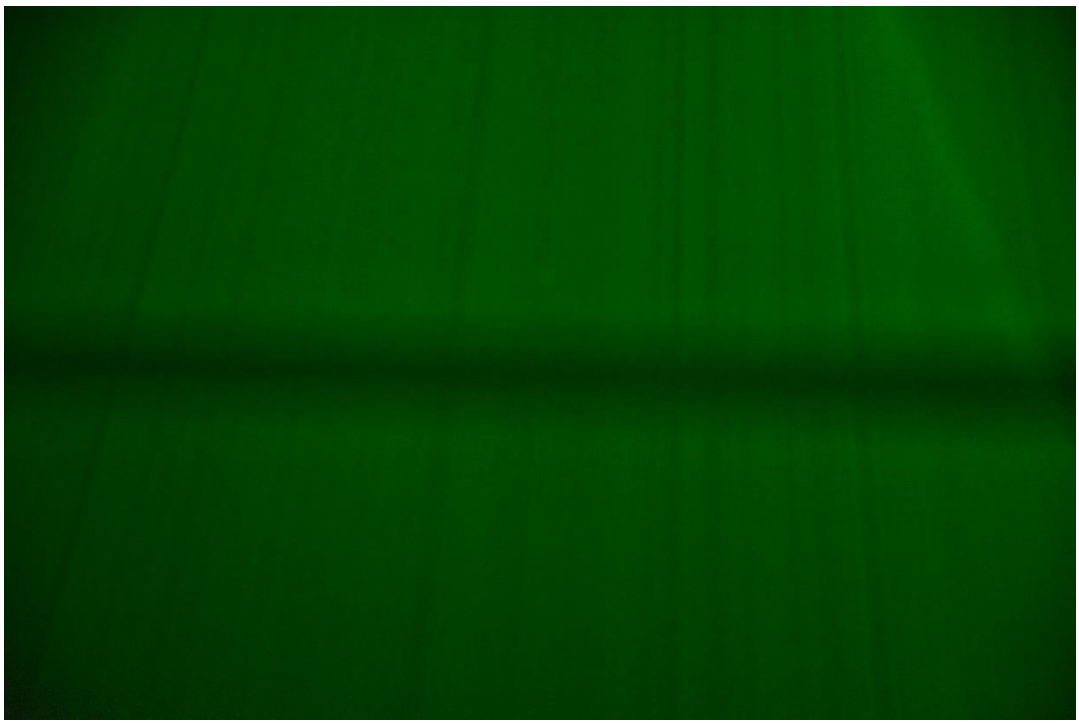

Figure 7 Example of the observed smoke-free vortex core region in the stream wise direction at an angle of attack of 12 degrees and a tunnel speed of 30 m/s.

The first set of tests were conducted with the laser sheet aligned along the wind tunnel flow axis in the stream wise direction, producing the dark "particle-free" line shown in Figure 8. The bi-wing angles of attack were then varied through ±4, ±8 and ±12 degrees and a sequence of approximately 15 images were taken in quick succession in order to determine which angles of

attack produced the most stable vortices. As will be discussed in the Results section, each frame in a series was analyzed by counting the number of smoke-free pixels in the vertical direction, in order to estimate the diameter of the vortex and locate its nominal centerline. Each frame in a series was then compared to the other frames in that series in order to assess any vortex variability and unsteadiness. Once the particular bi-wing angle of attack was established, a single image at each wind tunnel speed was obtained, in order to compare nominal core locations and diameters at each wind tunnel speed. This was done to assess any variability in the vortex size and axial location for each test series.

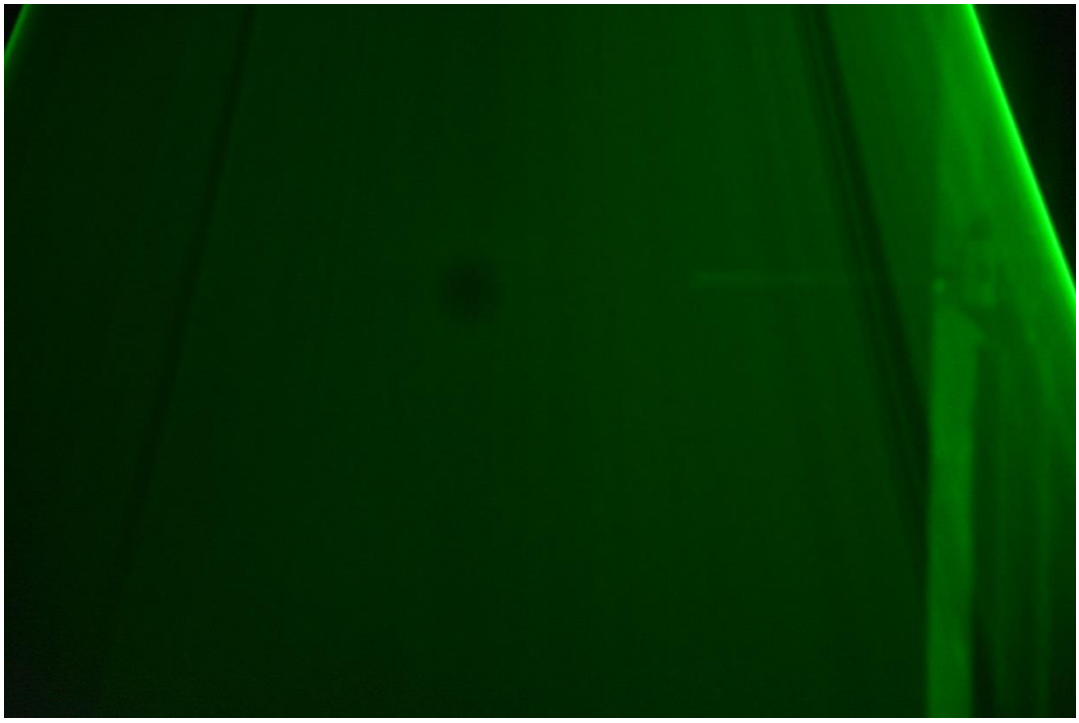

Figure 8 Example of spanwise flow visualization at a bi-wing angle of attack of ±12º and a tunnel speed of 40 m/s; 14 chord lengths downstream of the vortex generator

By rotating the laser sheet 90° so that it was perpendicular to the flow-direction, it was possible to examine the local vortex symmetry visually. The smoke-free vortex core can be seen clearly in the cross flow plane in Figure 8 Based on the visual stream wise observations, angles of attack of ±12° were selected for the detailed studies. That bi-wing configuration provided the most stable vortex behavior with the largest core diameters, at wind tunnel speeds of 30 and 40 m/s. The baseline tests repeated the same visualization sequence used during the stream wise tests. In order to assess repeatability and document the flow in the spanwise plane at the selected bi-wing configuration and associated wind tunnel test speeds the bi-wing generator was returned to the desired test configuration and a single image was taken for comparison with the earlier baseline image series.

Since the hot wire sensing element was mounted in a TSI 1241 probe at the end of a (4.6 mm diameter) probe support, it was necessary to determine the influence of the hotwire probe support geometry on the overall vortex core structure in the vicinity of the sensing element. To do this, pairs of photos were taken at each wind tunnel speed with the camera and illuminated laser sheet in fixed positions. One image was taken with the sensor probe in position and the other image was taken when the probe was removed. Images similar to the one shown in Figure 9 were produced when the sensing probe was located within the local vortex core with the laser sheet centered, and aligned in the stream wise direction. As can be seen in the figure, reflections from the sensor probe contaminated the vortex core region along the probe axis. However, the observable local smoke-free core diameters, measured along the vortex axis, could again be estimated utilizing pixel counts. These tests were also conducted with the laser oriented in the crossflow direction as illustrated by Figure 10 while glare from the probe support was less severe

in this case it did cast a sizable shadow making it impossible to estimate the full smoke-free diameter near the probe tip. Again images were captured with the probe present and not present at each speed setting. The local diameter of the vortex was then determined via pixels for both sets. At the cross sections near the sensing element tip, upstream from the probe support, there appeared to be only minimal distortion of the visual smoke-free region. A detailed analysis will follow in the next section.

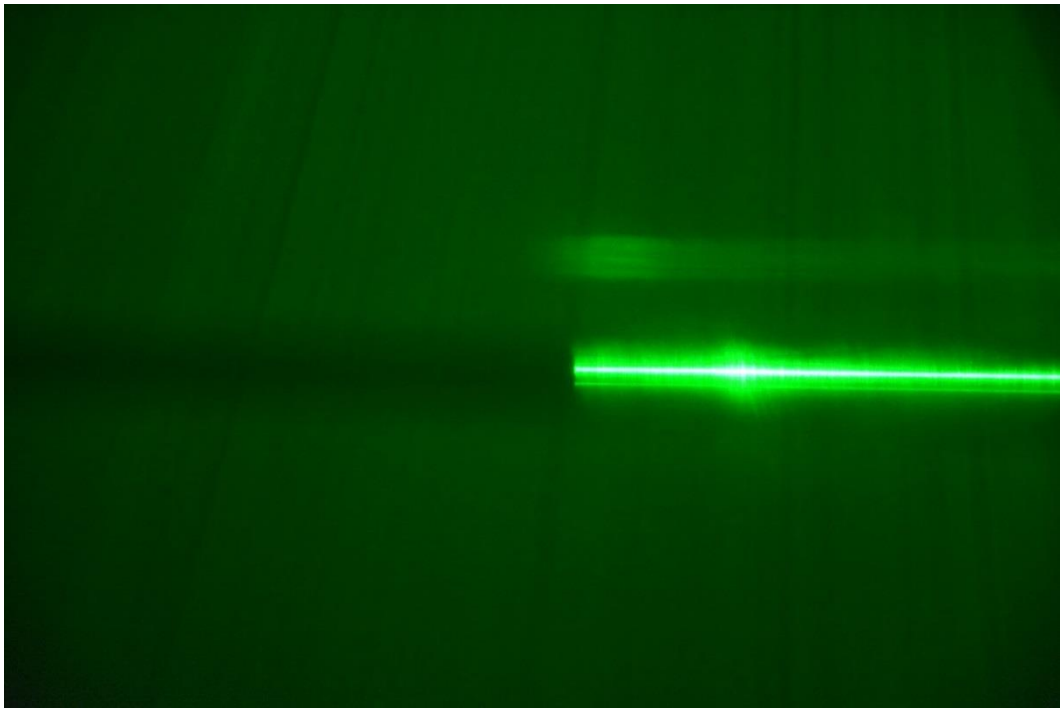

Figure 9 Image showing example of probe insertion during stream wise flow visualization at an angle of attack of 12 degrees and a tunnel speed of 30 m/s

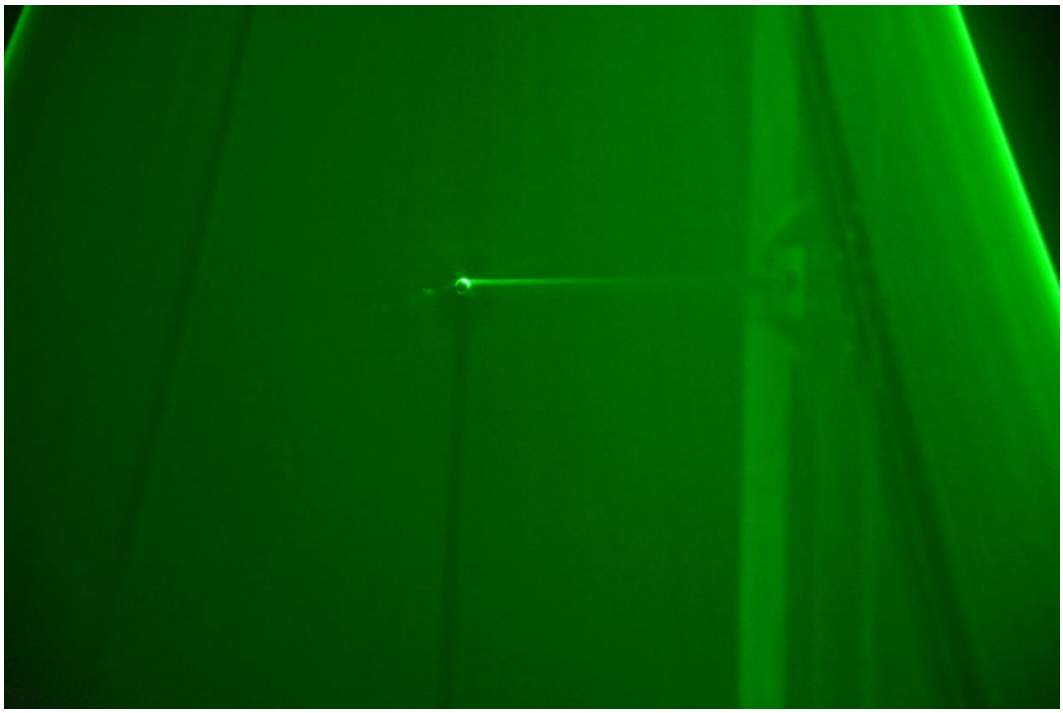

Figure 10 Image showing example of probe insertion during crossflow visualization at an angle of attack of 12 degrees and a tunnel set speed of 30 m/s at a location 14 chord lengths downstream of the vortex generator

2.4 Hot Wire Survey

In order to characterize the turbulent structure of the vortex core region, it was necessary to resolve low-frequency turbulent energy content. Consequently, the length of each data record, at a given measurement location, had to be sufficient to characterize the low-frequency turbulence. Based on the lowest predicted frequency values from the Abuharaz state variable model (Abuharaz and Ash, 2014), a 10-second record was considered to be sufficient. Data were acquired at a sample rate of 100 kHz, which was the maximum achievable for two-channel records, in order to

provide fluctuation data at the smallest possible scales. This allowed frequency resolution up to 50 kHz.

Data were generated at each downstream survey plane utilizing a rectangular 20 cm by 17 cm survey area, centered on the nominal vortex rotational axis. After the X-probe sensing element was positioned in the grid plane, utilizing the computer-controlled traverse system, 10-second velocity records were obtained at pre-selected survey locations. Utilizing a best-estimate of the vortex axis location, the X-probe was moved in 2 mm steps, within the central 4 cm by 4 cm region of the larger surveying area. Horizontal survey traverses were initiated at the outer edge of the survey area, 10 cm from the rotational center. Outside of the central 4 cm by 4 cm area, measurements were taken at 5 mm intervals between ± 2 cm and ± 5 cm, then at 1 cm intervals between ± 5 cm and ±10 cm. When a full-width horizontal traverse was completed, the traverse system was commanded to translate vertically, by 2 mm, then proceed to the inner 4 cm by 4 cm sensing area, taking measurements every 2 mm. Since the 5 mm outer measurement spacing interval was only surpassed in the vertical direction, after every third vertical step, it was only when two successive vertical inner area sweeps were completed, that the subsequent (third) vertical translation survey was expanded to cover the entire 20 cm survey width, while utilizing the overall measurement spacing intervals just laid out. Figure 11, illustrates the survey grid in relation to the tunnel spatial coordinate system.

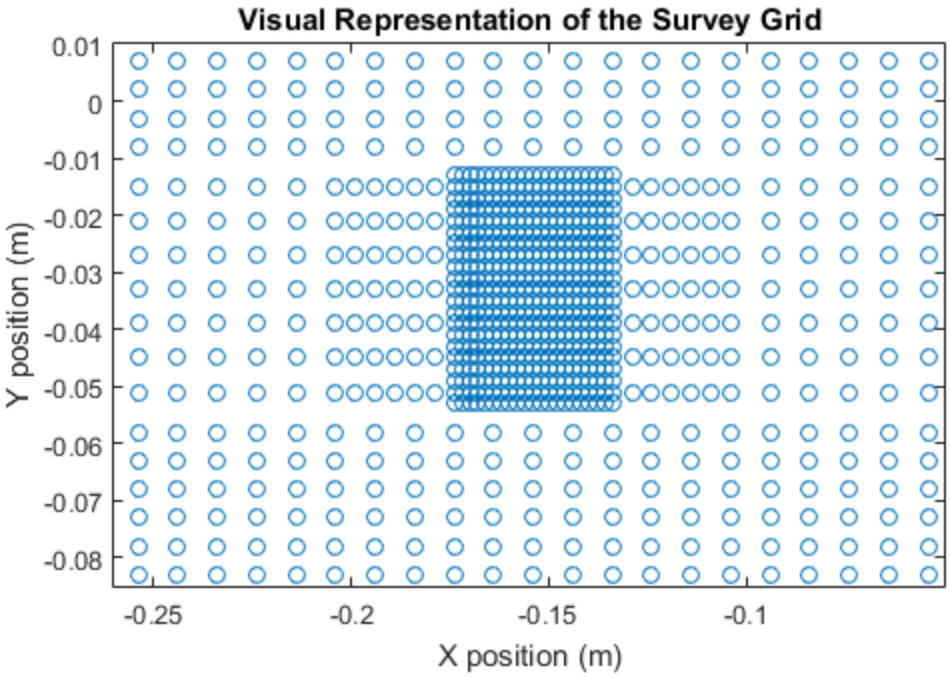

Figure 11 Survey grid in relation to tunnel coordinate system

Many of the axial vortex characteristics can be scaled utilizing the bi-wing geometry (Romeos, Lemonis, Panidis, and Papailiou 2009, Romeos and Panidis 2010). In the present study, the wing chord was 5 inches (c = 127 mm), and that chord length was employed as the axial reference dimension. Consequently, the downstream location of the survey planes have been presented using $\bar{z} \equiv (z - z_o)/c$. That representation will be used throughout the remainder of this thesis. The first survey plane was located 7 chord lengths downstream from the trailing edges of the vortex generator, and the two subsequent survey planes were located 10.5 and 14.0 chord lengths downstream. At each survey plane, measurements were taken with wind tunnel test speeds of 30 m/s and 40 m/s. Initially, a 20 m/s wind speed was planned, but the flow visualization studies showed that the resulting vortex was highly unstable and moved erratically.

2.5 Uncertainty Analysis

An uncertainty analysis was conducted using the Taylor Series method of uncertainty propagation for multiple variables as described in Coleman and Steele (2009). The general equation for uncertainty propagation was

$$dF = \sqrt{\sum_{i=1}^{M} \left(\frac{\partial F}{\partial X_i}\right)^2 dX_i{}^2} \tag{20}$$

As applied to this experiment, uncertainty propagation started with the temperature correction

$$dE' = \sqrt{\left(m(T_{cal} - T_{tunnel})\right)^2 dE^2 + (E-m)^2 (dT)^2} \tag{21}$$

This was applied to both voltages, E1 and E2, in the calibration equations. The uncertainty was then propagated through the calibration equations resulting in the following relations:

$$dU = \sqrt{\left(\frac{\partial U}{\partial E_1}\right)^2 dE_1^2 + \left(\frac{\partial U}{\partial E_2}\right)^2 dE_2^2} \tag{22}$$

$$d\theta = \sqrt{\left(\frac{\partial \theta}{\partial E_1}\right)^2 dE_1^2 + \left(\frac{\partial \theta}{\partial E_2}\right)^2 dE_2^2} \tag{23}$$

Propagating the error through the trigonometric functions to separate the components of velocity results in the following uncertainties for each sample of each velocity component.

$$du = \sqrt{(\cos\theta)^2 dU^2 - (U\sin\theta)^2 d\theta^2} \tag{24}$$

$$dv = \sqrt{(\sin\theta)^2 dU^2 + (U\cos\theta)^2 d\theta^2} \tag{25}$$

The final step of propagating the error was to propagate it through the process of taking the mean, resulting in

$$d\bar{u} = \frac{\sqrt{\sum du^2}}{N} \tag{26}$$

$$d\bar{v} = \frac{\sqrt{\sum dv^2}}{N} \tag{27}$$

Equations 26 and 27 were used to generate the error bars used in the plots in the sections that follow.

CHAPTER III

EXPERIMENTAL RESULTS

3.1 Flow Visualization

Analysis of images captured during flow visualization experiments was conducted using *Adobe Photoshop* in an effort to quantify any observed core region fluctuations, and ascertain spatial stability of the vortex. With the laser oriented in the stream wise direction making visible the X-Z plane a series of approximately 15 photos were taken in rapid succession at each bi-wing angle of attack at 30 and 40 m/s. The indicated diameter of the vortex in each image was then determined by establishing edges of the smoke-free vortex core region, employing a one-pixel-wide line, shown as a red line in the subsequent images, superimposed on the image where the change between darkened and bright pixels occurred and counting the number of darkened pixels in the interval between the bounding lines. The location of the vortex centerline was then established by counting the number of pixels from the pixel located midway between the bounding lines to the top of the frame at a point approximately centered in the frame. An annotated example of this process can be found in Figure 12. The results of this analysis follows.

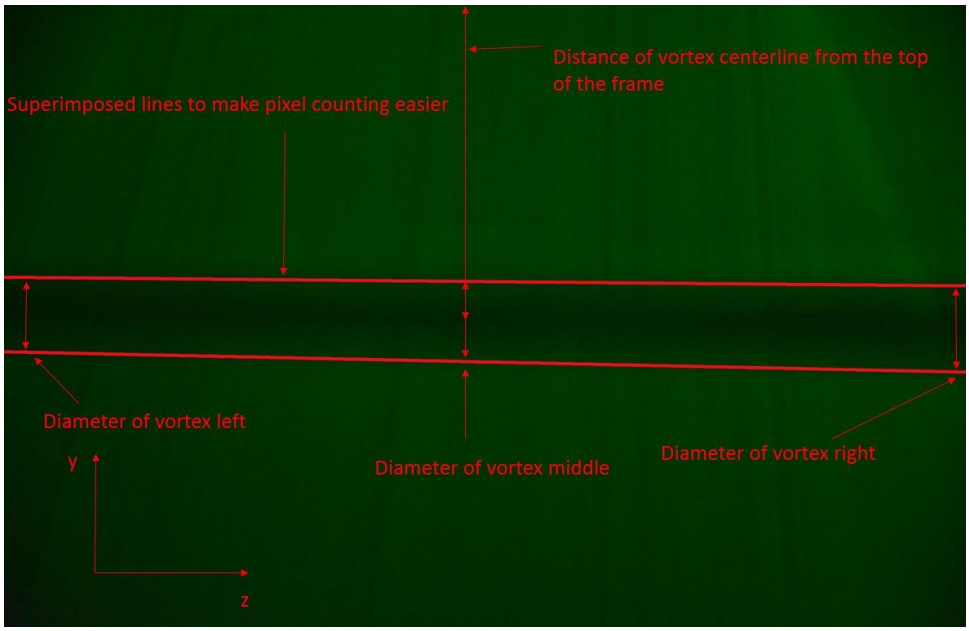

Figure 12 Annotated example of the analysis of flow visualization photos at 12 degrees angle of attack and a tunnel setting of 40 m/s

Figure 13 Streamwise flow in the x-z plane at 4 degrees angle of attack and 40 m/s

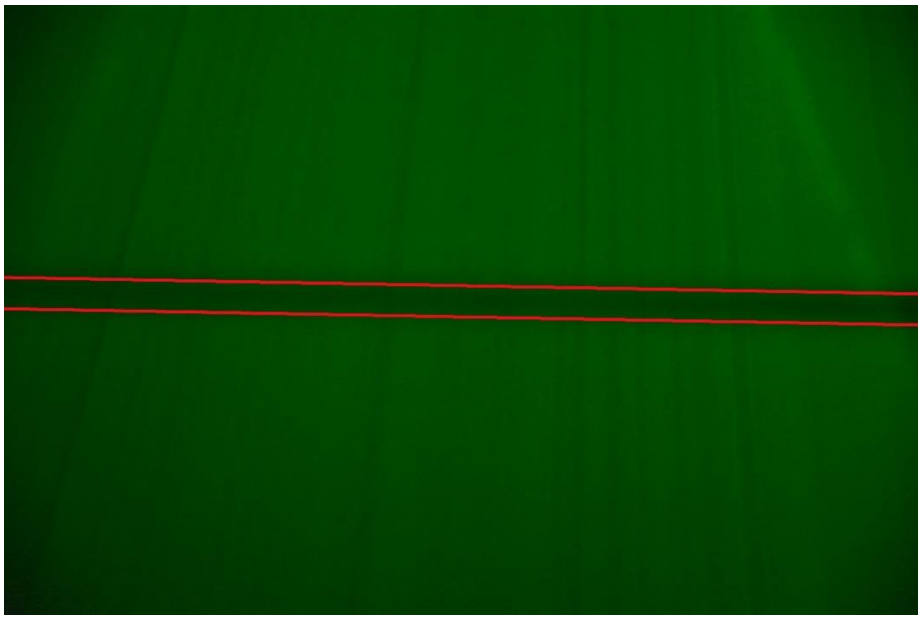

Figure 14 Streamwise flow visualization at 8 degrees angle of attack and 20 m/s

Photo id	Left side	Right side	Middle	Distance From Top of Frame
dsc0596	197.9	191.9	197.9	1841
dsc0597	197.9	191.9	191.9	1895
dsc0598	197.9	191.9	191.9	1841
dsc0599	197.9	191.9	191.9	1859
dsc0600	191.9	197.9	197.9	1829
dsc0601	191.9	197.9	197.9	1805
dsc0602	191.9	197.9	197.9	1835
dsc0603	197.9	197.9	191.9	1817
dsc0604	191.9	197.9	197.9	1817
dsc0605	191.9	197.9	197.9	1823
dsc0606	191.9	191.9	197.9	1853
dsc0607	197.9	197.9	197.9	1835
dsc0608	191.9	197.9	197.9	1865
dsc0609	197.9	197.9	197.9	1847
Average pixel count	194.9	195.75	196.18	1840.14
Pixel Standard Deviation	3	2.87	2.71	22.32

Table 3 Statistics gathered from streamwise flow visualization at 8 degrees angle of attack and a tunnel velocity of 20 m/s

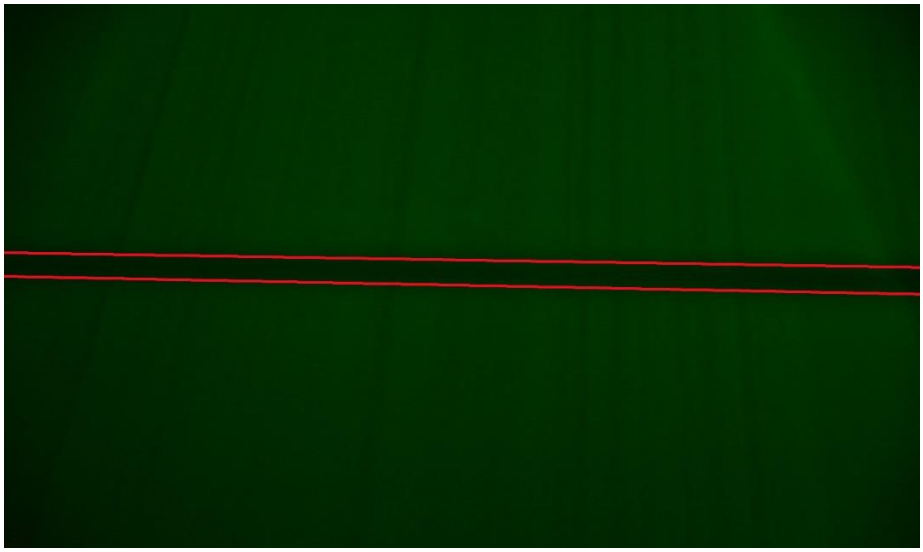

Figure 15 Streamwise flow visualization at 8 degrees angle of attack and 30 m/s

Photo id	Left side	Right side	Middle	Distance From Top
dsc0614	167.92	191.9	185.91	1883
dsc0615	143.93	137.93	131.93	1883
dsc0616	179.9	197.9	197.9	1847
dsc0617	197.9	149.93	167.92	1877
dsc0618	173.91	155.92	161.92	1829
dsc0619	149.93	131.93	143.93	1835
dsc0620	173.91	137.9	161.92	1841
dsc0621	173.91	155.92	161.92	1859
dsc0622	155.92	125.94	137.93	1853
dsc0623	179.91	185.91	185.91	1835
dsc0624	167.92	197.9	185.91	1835
dsc0625	155.92	149.93	143.93	1871
dsc0626	167.92	191.9	191.9	1805
dsc0627	167.92	179.91	173.91	1835
Average pixel count	168.344	163.63	166.63	1849.14
Pixel Standard Deviation	13.31	25.29	20.55	22.17

Table 4 Statistics gathered from streamwise flow visualization at 8 degrees angle of attack and a tunnel velocity of 30 m/s

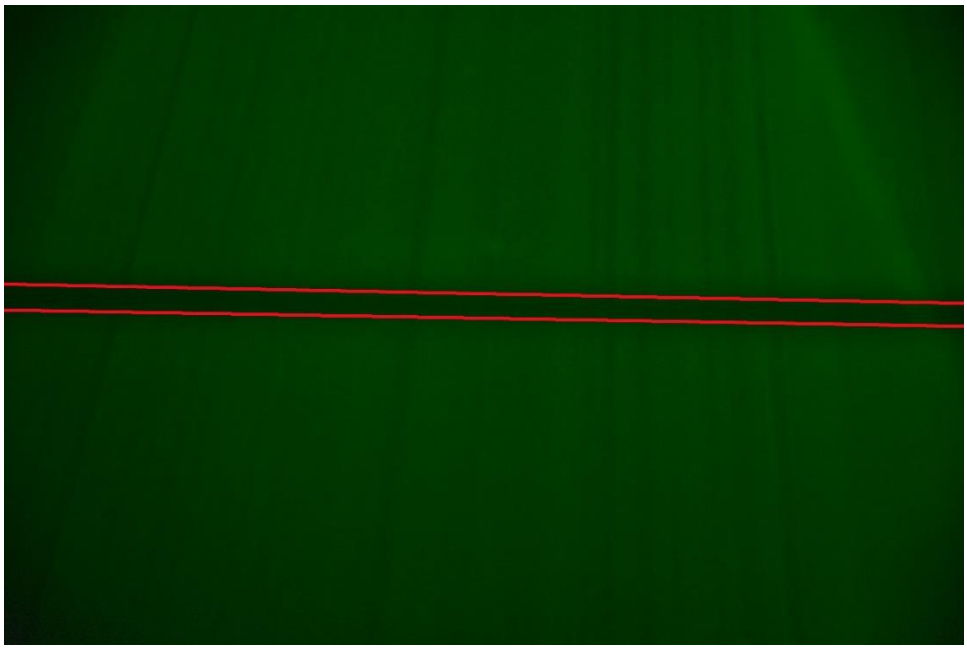

Figure 16 Streamwise flow visualization at 8 degrees angle of attack and 40 m/s

Photo id	Left Side	Right Side	Middle	Distance From Top
dsc0631	149.93	143.93	149.93	1811
dsc0632	191.9	197.9	185.91	1787
dsc0633	167.92	149.93	155.92	1787
dsc0634	167.92	155.92	155.92	1817
dsc0635	191.9	125.94	167.92	1793
dsc0636	149.93	125.94	131.93	1811
dsc0637	173.91	131.93	155.92	1811
dsc0638	125.94	143.93	143.93	1793
dsc0639	179.91	161.92	185.91	1775
dsc0640	185.91	179.91	185.91	1781
dsc0641	185.91	185.91	185.91	1805
dsc0642	179.91	161.92	173.91	1793
dsc0643	161.92	179.91	161.92	1805
dsc0644	131.93	137.93	131.93	1793
Average pixel count	167.49	155.92	162.35	1797.29
Pixel Standard Deviation	20.46	22.21	18.62	12.30

Table 5 Statistics gathered from streamwise flow visualization at 8 degrees angle of attack and a tunnel velocity of 40 m/s

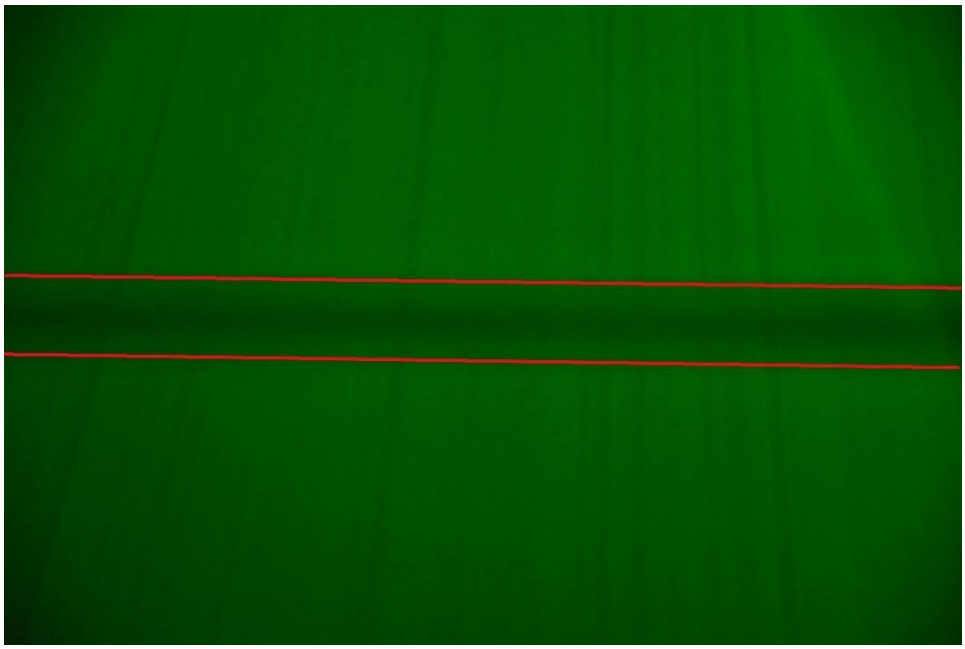

Figure 17 Streamwise flow visualization at 12 degrees angle of attack and 20 m/s

Photo id	Left side	Right side	Middle	Distance From Top
dsc0544	461.77	479.75	485.76	1775
dsc0545	497.75	497.75	497.75	1727
dsc0546	443.78	479.76	461.77	1769
dsc0547	491.75	491.75	491.75	1793
dsc0548	473.76	497.75	479.76	1685
dsc0549	449.78	431.78	455.77	1715
dsc0550	485.75	485.75	485.75	1757
dsc0551	497.75	497.75	497.75	1757
dsc0552	455.77	479.76	461.77	1799
dsc0553	491.75	479.76	521.74	1721
dsc0554	437.78	425.79	437.78	1799
dsc0555	473.76	443.78	461.77	1739
dsc0556	479.76	497.75	485.76	1805
Average pixel count	472.38	476.07	478.84	1757
Pixel Standard Deviation	19.98	24.50	21.41	36.23

Table 6 Statistics gathered from streamwise flow visualization at 12 degrees angle of attack and a tunnel velocity of 20 m/s

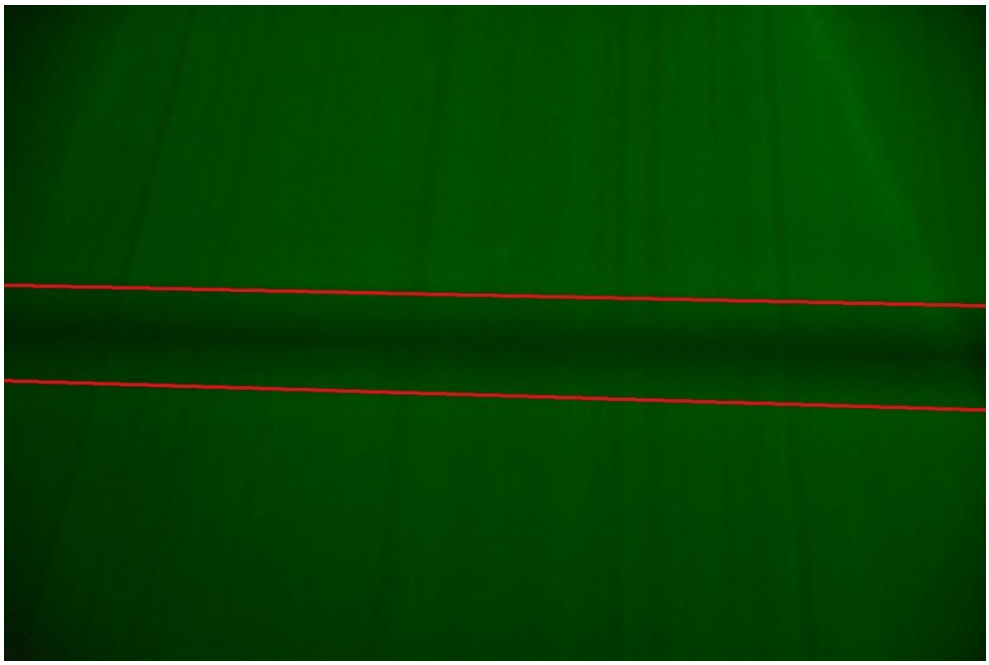

Figure 18 Streamwise flow visualization at 12 degrees angle of attack and 30 m/s

Photo id	Left Side	Right Side	Middle	Distance From Top
dsc0560	575.71	635.68	605.7	1751
dsc0561	563.72	593.7	575.71	1757
dsc0562	611.69	533.73	575.71	1787
dc0563	527.74	521.74	533.73	1775
dsc0564	569.72	581.71	563.72	1763
dsc0565	491.75	639.73	509.75	1799
dsc0566	569.72	527.74	551.72	1775
dsc0567	521.74	521.74	533.73	1787
dsc0568	485.76	479.76	485.76	1811
dsc0569	539.79	575.71	563.72	1757
dsc0570	557.72	569.72	569.72	1769
dsc0571	521.74	539.73	627.74	1757
dsc0572	509.75	503.75	633.73	1817
Average pixel count	542.04	555.73	563.88	1777.31
Pixel Standard Deviation	35.09	46.80	41.16	20.72

Table 7 Statistics gathered from streamwise flow visualization at 12 degrees angle of attack and a tunnel velocity of 30 m/s

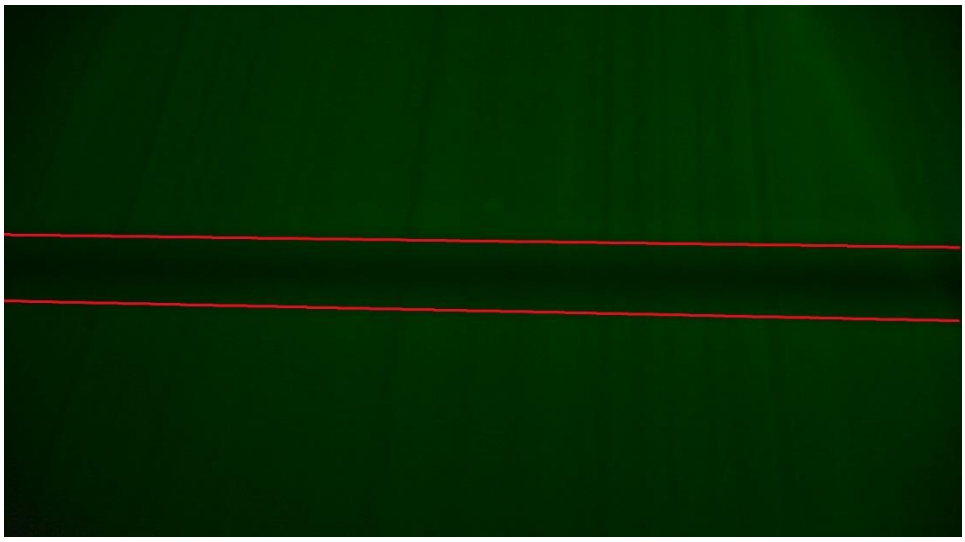

Figure 19 Streamwise flow visualization at 12 degrees angle of attack and 40 m/s

photo id	Left Side	Right Side	Middle	Distance From Top
dsc0574	455.77	521.74	497.75	1811
dsc0575	497.75	545.73	521.74	1781
dsc0576	491.75	545.73	515.74	1751
dsc0577	527.74	569.72	551.72	1751
dsc0578	521.74	599.7	563.72	1757
dsc0579	551.72	503.75	527.74	1751
dsc0580	503.75	545.73	539.73	1769
dsc0581	503.75	527.74	515.74	1751
dsc0582	539.73	563.72	539.73	1775
dsc0583	509.75	563.72	533.73	1769
dsc0584	455.77	479.76	473.76	1805
dsc0585	503.75	551.72	521.74	1763
dsc0586	491.75	527.74	509.75	1769
dsc0587	539.73	521.74	539.73	1757
dsc0588	491.75	545.73	527.74	1739
dsc0589	575.71	539.73	545.73	1793
dsc0590	539.73	569.72	551.72	1781
dsc0591	515.74	575.71	539.73	1781
Average pixel count	517.46	544.02	530.74	1768.57
Pixel Standard Deviation	29.07	29.76	20.87	17.04

Table 8 Statistics gathered from streamwise flow visualization at 12 degrees angle of attack and a tunnel velocity of 40 m/s

Only one observation was needed at the +/- 4 degrees angle of attack. As can be seen in Figure 13, there is not a usable vortex for measurement purposes at this angle of attack. At +/- 8 degrees angle of attack, the vortex was reasonably stable at both tunnel test speeds. However, the resulting vortex was considered to be too small. Vortex core size posed a problem because the smaller the vortex core diameter, the greater the flow distortion resulting from inserting the hot film probe. The vortex produced using +/- 12 degrees angle of attack and 20 m/s showed the largest instabilities, based on the sequential images, producing a standard deviation of 36.23 pixels. However the vortices at the other two speed settings and an angle of attack 12 degrees were the largest observed and had similar stability to those observed at 8 m/s, because of this it was decided that the hotwire survey would be conducted at an angle of attack setting of 12 degrees. Due to the extreme oscillations in vortex location at the 20 m/s wind speed, (and +/- 12 degree angle of attack setting), those flow surveys were abandoned.

Tests were then conducted with the laser sheet oriented in the cross flow direction, at the three planned downstream hotwire survey planes, for the ±12 degree bi-wing setting, at tunnel speeds of 30 and 40 m/s. The goal of these particular tests was to produce statistics to compare with the visual stream wise flow measurements. Since the camera position would be different for each survey plane, the physical meaning of a pixel would be different for each plane. As a result as a measure of the amount of change the most useful pixel statistic was the standard deviation behavior, because this gave an indication of overall vortex stability.

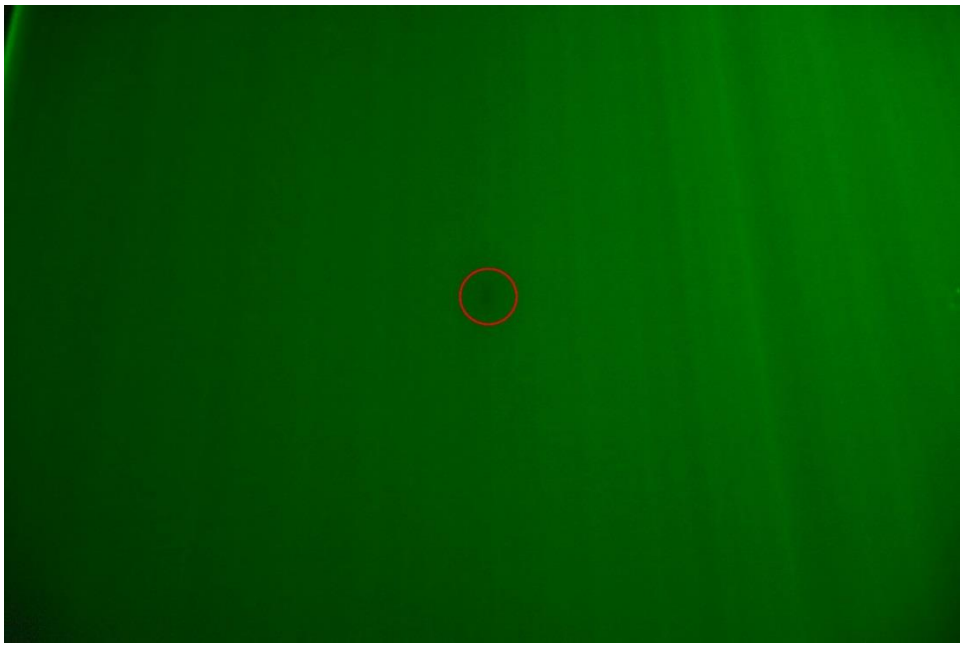

Figure 20 Crosswise flow visualization 7 chord lengths downstream from the vortex generator at 12 degrees angle of attack and 30 m/s

Photo id	Diameter	Distance From Top
dsc0884	304	1856
dsc0885	336	1808
dsc0886	344	1826
dsc0887	300	1840
dsc0888	328	1825
dsc0889	312	1824
dsc0890	336	1824
dsc0891	320	1818
dsc0892	304	1824
dsc0893	304	1816
dsc0894	304	1800
dsc0895	330	1816
Average pixel count	318.5	1823.08
Pixel Standard Deviation	15.04	13.76

Table 9 Statistics gathered from crosswise flow visualization 7 chord lengths downstream from the vortex generator at 12 degrees angle of attack and 30 m/s

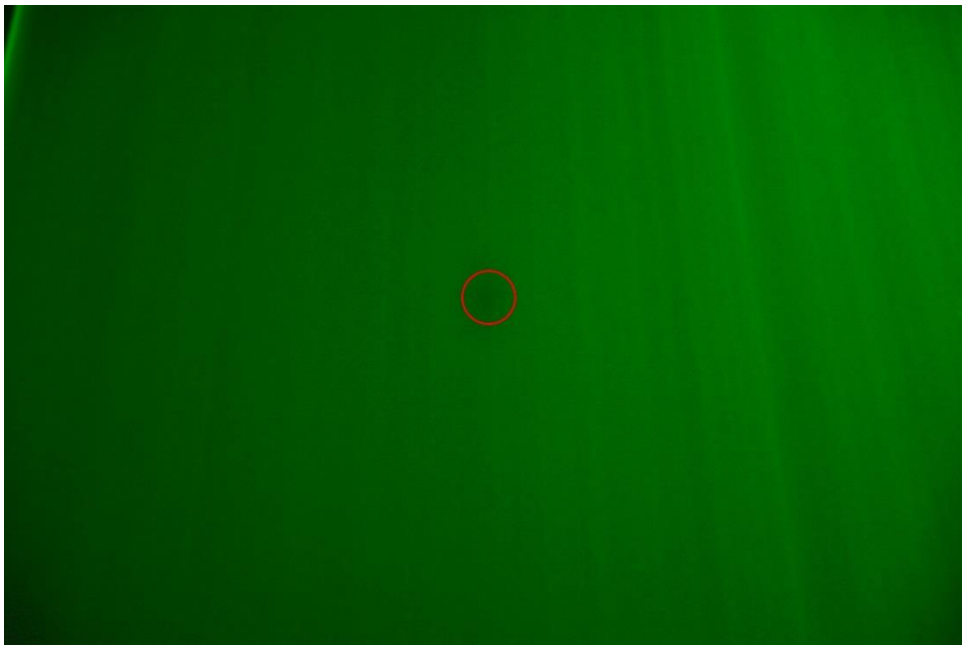

Figure 21 Crosswise flow visualization 7 chord lengths downstream from the vortex generator at 12 degrees angle of attack and 40 m/s

photo id	Diameter	Centers Distance From Top
dsc900	312	1832
dsc901	304	1800
dsc902	304	1816
dsc903	312	1808
dsc904	320	1808
dsc905	312	1808
dsc906	304	1800
dsc907	304	1808
dsc908	312	1800
dsc909	320	1800
dsc910	304	1816
dsc911	320	1800
dsc912	312	1800
dsc913	304	1816
Average pixel count	310.29	1808
pixel standard deviation	6.18	9.07

Table 10 Statistics gathers from crosswise flow visualization 7 chord lengths downstream from the vortex generator at 12 degrees angle of attack and 40 m/s

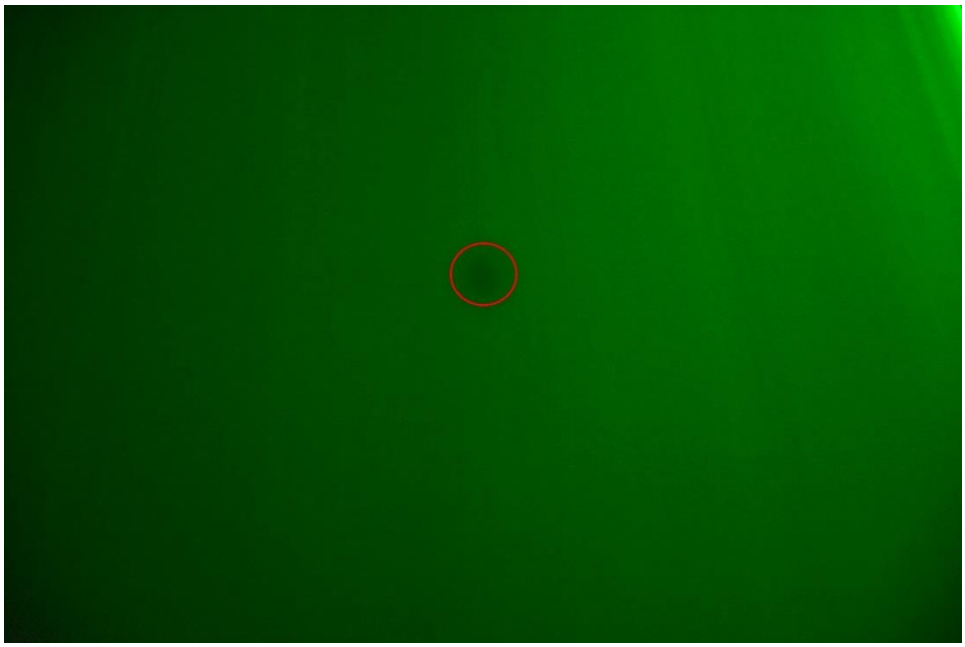

Figure 22 Crosswise flow visualization 10.5 chord lengths downstream from the vortex generator at 12 degrees angle of attack and 30 m/s

photo id	Diameter	Centers Distance From Top
dsc800	376	1704
dsc801	386	1688
dsc802	344	1672
dsc803	328	1648
dsc804	368	1688
dsc805	312	1680
dsc806	336	1672
dc807	336	1688
dsc808	336	1672
dsc809	344	1672
dsc810	344	1696
Average Pixel Count	346.36	1680
Pixel Standard Deviation	20.83	14.47

Table 11 statistics gathers from flow visualization 10.5 chord lengths downstream from the vortex generator at 12 degrees angle of attack and 30 m/s

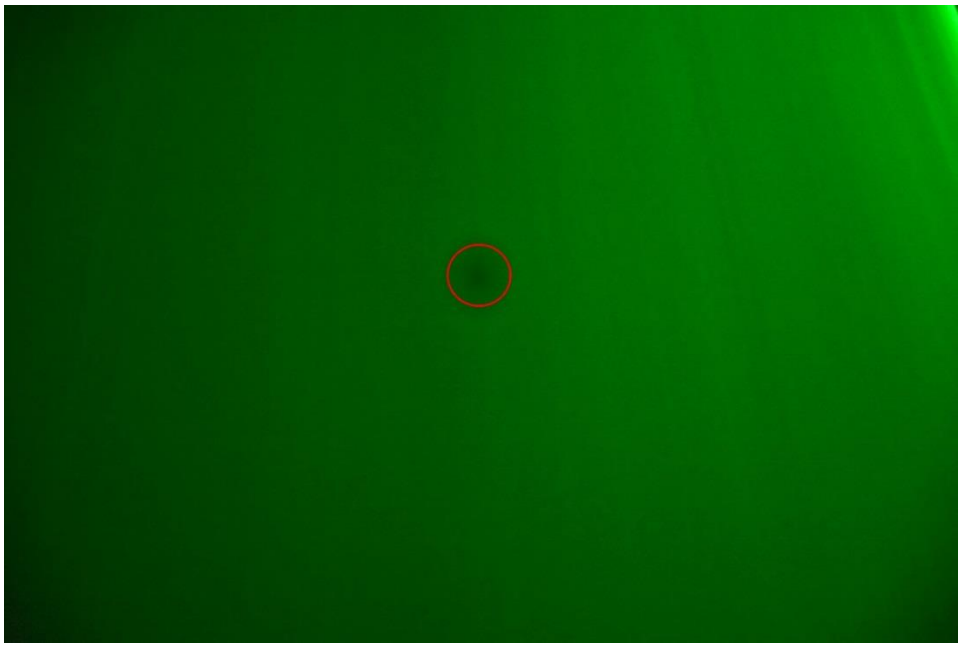

Figure 23 Crosswise flow visualization 10.5 chord lengths downstream from the vortex generator at 12 degrees angle of attack and 40 m/s.

photo id	Diameter	Centers Distance From Top
dsc813	376	1688
dsc814	347	1652
dsc815	359	1664
dsc816	335	1700
dsc817	359	1664
dsc818	395	1652
dsc819	374	1688
dsc820	359	1688
dsc821	383	1664
dsc822	395	1676
dsc823	347	1676
dsc824	371	1676
Average Pixel Count	366.67	1674
Pixel Standard Deviation	18.22	14.56

Table 12 statistics gathered from crosswise flow visualization 10.5 chord lengths downstream from the vortex generator at 12 degrees angle of attack and 40 m/s

Figure 24 Crosswise flow visualization 14 chord lengths downstream from the vortex generator at 12 degrees angle of attack and 30 m/s

photo id	diameter	Centers Distance From Top
dsc725	359	1568
dsc726	371	1592
dsc727	371	1580
dsc728	359	1616
dsc729	395	1568
dsc730	383	1604
dsc731	371	1616
dsc732	335	1604
dsc733	359	1640
dsc734	395	1616
dsc735	383	1616
dsc736	359	1604
Average Pixel Count	370	1602
Pixel Standard Deviation	16.58	20.69

Table 13 statistics gathers from flow visualization 14 chord lengths downstream from the vortex generator at 12 degrees angle of attack and 30 m/s

Figure 25 crosswise flow visualization 14 chord lengths downstream from the vortex generator at 12 degrees angle of attack and 40 m/s

photo id	diameter	Centers distance from top of frame
dsc740	347	1592
dsc741	335	1604
dsc742	383	1604
dsc743	335	1616
dsc745	371	1616
dsc746	371	1604
dsc747	383	1640
dsc748	371	1604
dsc749	347	1604
dsc750	359	1580
dsc751	359	1616
Average pixel count	360.09	1607.27
pixel standard deviation	16.54	14.55

Table 14 statistics gathered from flow visualization 14 chord lengths downstream from the vortex generator at 12 degrees angle of attack and 30 m/s

These flow visualization documentation tests were conducted with the camera at a different location for each of the three downstream planes. As a consequence, the mean diameter estimates at each survey plane cannot be compared directly. However, the most important statistic was the standard deviation of the dimensionless local diameter because it was a measure of the stability of the vortex at each test condition. The low standard deviations observed are comparable or smaller to the standard deviations observed during streamwise flow visualization. This confirms the assertion that the bi-wing generator configuration without a centerbody and at the selected hotwire wind tunnel test speeds produces the largest, most stable vortex structures.

In order to demonstrate that the vortex remained in approximately the same state after the vortex generators settings had been changed and returned to the desired settings. A single photo was taken at each speed setting once the angle of attack of ±12 degrees had been established, and the spatial location and diameter of the vortex were then determined via pixel counts. These data were then compared with the statistics obtained from the series of photos taken when the bi-wing generator and tunnel speeds matched the original baseline documentation conditions. Since the camera position and settings were not changed, it was possible to directly compare pixel counts.

Tunnel Speed	left side diameter	right side	middle	distance from top of frame
30 m/s	532	541	541	1797
40 m/s	535	583	553	1791

Table 15 Statistics from the single frames captured during streamwise flow after the vortex generator was returned to a ±12 degrees angle of attack configuration from a different setting

The results, summarized in Table 15 for "pixel diameters" along the length of the vortex and the distance in pixels of the center line from the top of the frame all fall within one standard deviation of the means observed when the vortex generator and tunnel was originally set to these conditions. This confirms the repeatability of the experimental set-up and associated test conditions.

To assess the distortion resulting from the hotwire probe, photos were taken with the blunt-nosed probe support positioned near the center of rotation in the survey plane and the smoke-free position and diameter were determined as before. The first photo was taken with the probe absent from the vortex, the probe support was then inserted into the approximate visual center of the vortex and a photo taken. The diameter and centerline location from each photo were then compared.

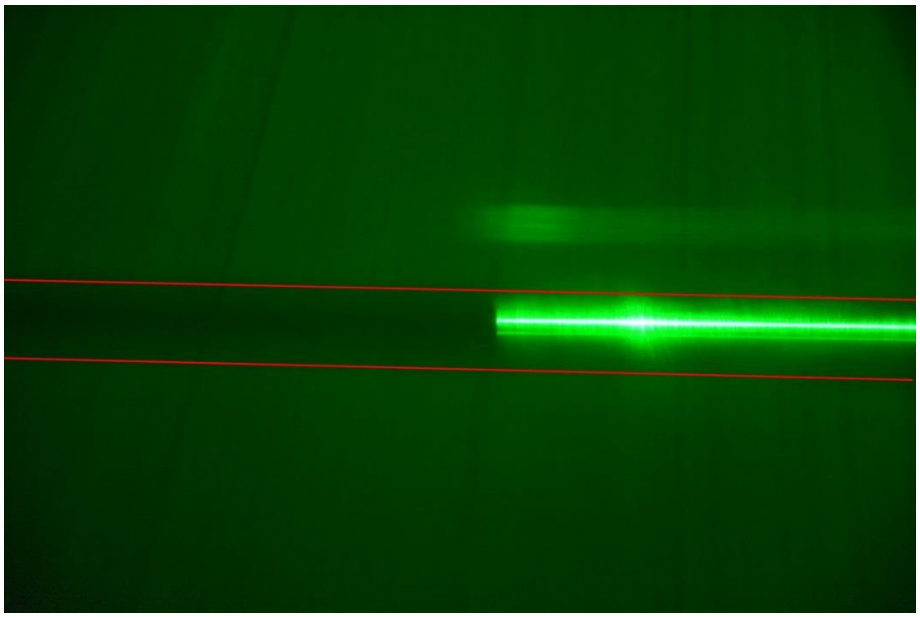

Figure 26 Probe support inserted into the vortex 12 degrees angle of attack and a tunnel speed of 30 m/s

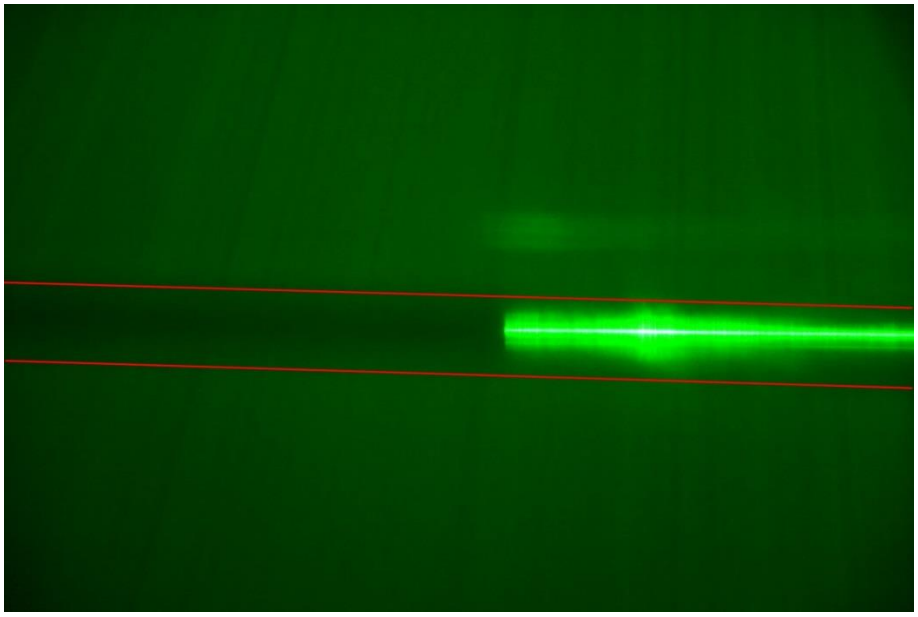

Figure 27 Probe support inserted into the vortex 12 degrees angle of attack and a tunnel speed of 30 m/s

Tunnel Speed	Probe Status	Left Side Diameter	Right Side Diameter	Middle Diameter	Distance From Top of Frame
30 m/s	Out	485.76	533.73	509.75	1835
	in	497	540	521.74	1952
40 m/s	out	528	548	532	1829
	in	532	572	560	1940

Table 16 Statistics gathered from before and after streamwise probe insertion

In these comparisons the observed vortex core region was found consistently to be larger. The magnitude of this difference varied from frame to frame, which indicated the mechanisms influencing the periodic change in vortex size were intact despite the disruption caused by the probe support. However on average the dilation caused by the probe support was less than 18.67 pixels at 40 m/s and 9.83 pixels at 30 m/s. Since the hotwire probe support was known to be 4.6 mm in diameter it was possible to determine that there were 0.02 mm per pixel. With this it was possible to determine that the dilantions were 0.2 mm at 30 m/s and 0.4 mm at 40 m/s. This variation will be nearly undetectable with the 2 mm spatial resolution of the hotwire survey and is thus considered to be a minor influence.

The process of comparing a photo from before probe support insertion to after probe support insertion was again conducted using photos with the laser oriented in the cross flow direction.

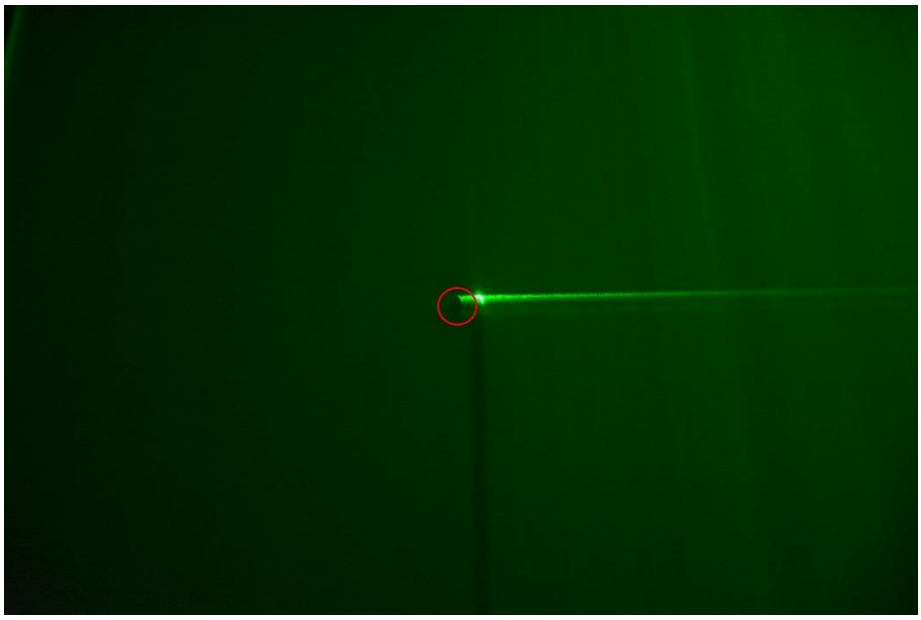

Figure 28 crosswise flow visualization during probe insertion 7 chord lengths downstream at a tunnel speed of 30m/s

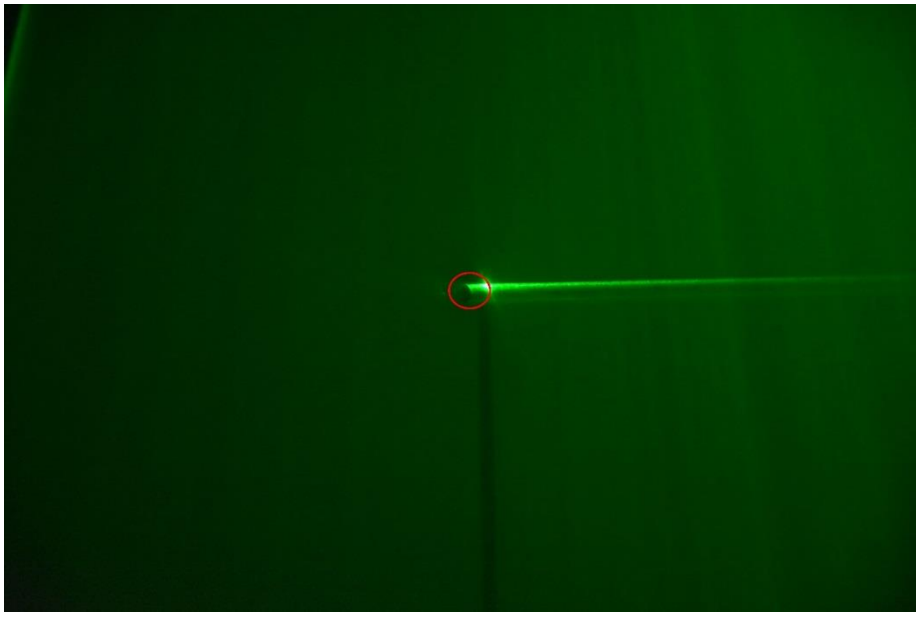

Figure 29 crosswise flow visualization during probe insertion 7 chord lengths downstream at a tunnel speed of 40m/s

Tunnel Speed	Probe Status	Diameter Of Vortex	Distance From Top
30 m/s	Out	251	1832
	in	275	1940
40 m/s	out	239	1829
	in	257	1865

Table 17 Statistics gathered before and after probe insertion during crosswise flow visualization, seven chord lengths downstream from the vortex generator

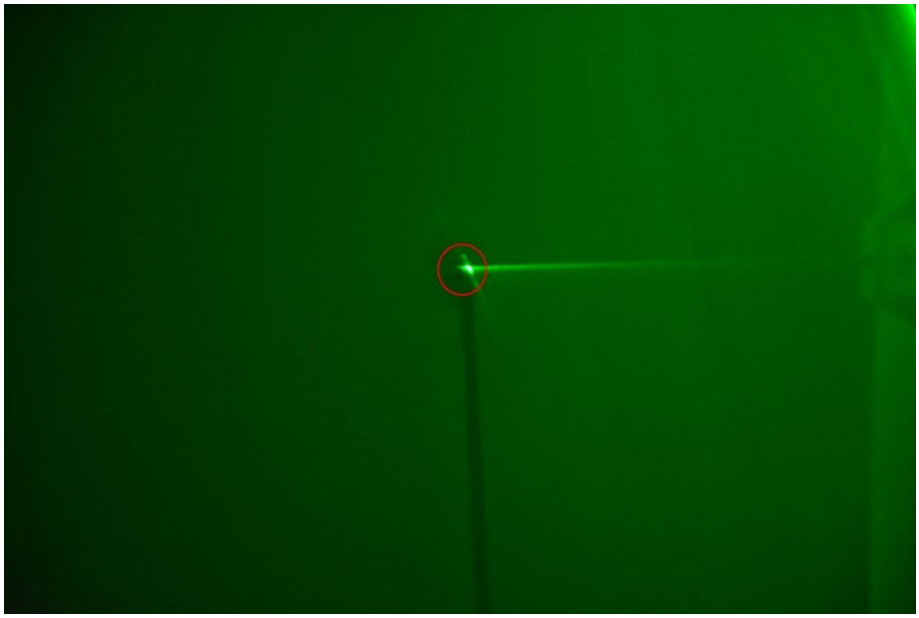

Figure 30 crosswise flow visualization during probe insertion 10.5 chord lengths downstream at a tunnel speed of 30m/s

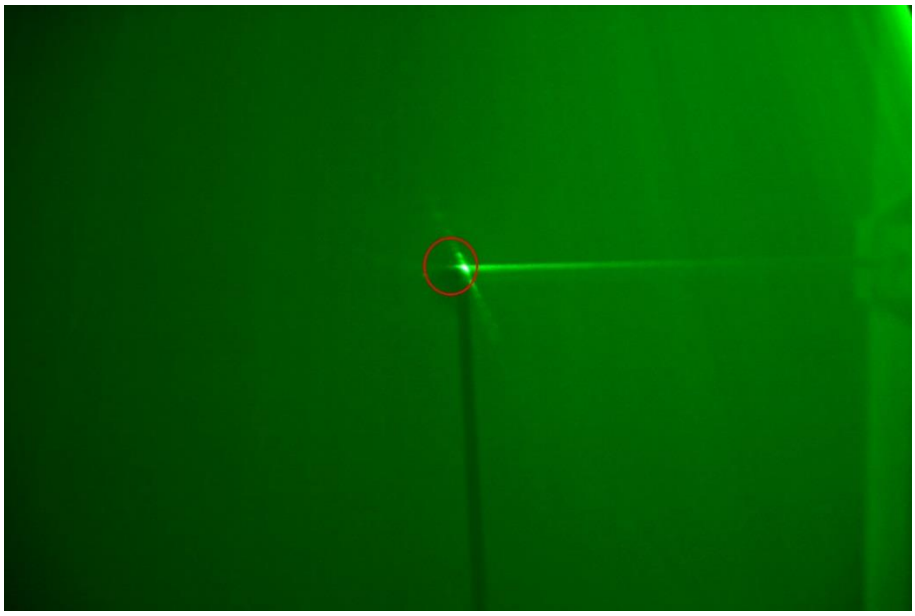

Figure 31 crosswise flow visualization during probe insertion 10.5 chord lengths downstream at a tunnel speed of 40m/s

Tunnel Speed	Probe Status	Diameter Of Vortex	Distance From Top
30 m/s	Out	335	1753
	in	389	1733
40 m/s	out	371	1736
	in	395	1724

Table 18 Statistics before and after probe insertion during crosswise flow visualization, 10.5 chord lengths downstream from the vortex generator

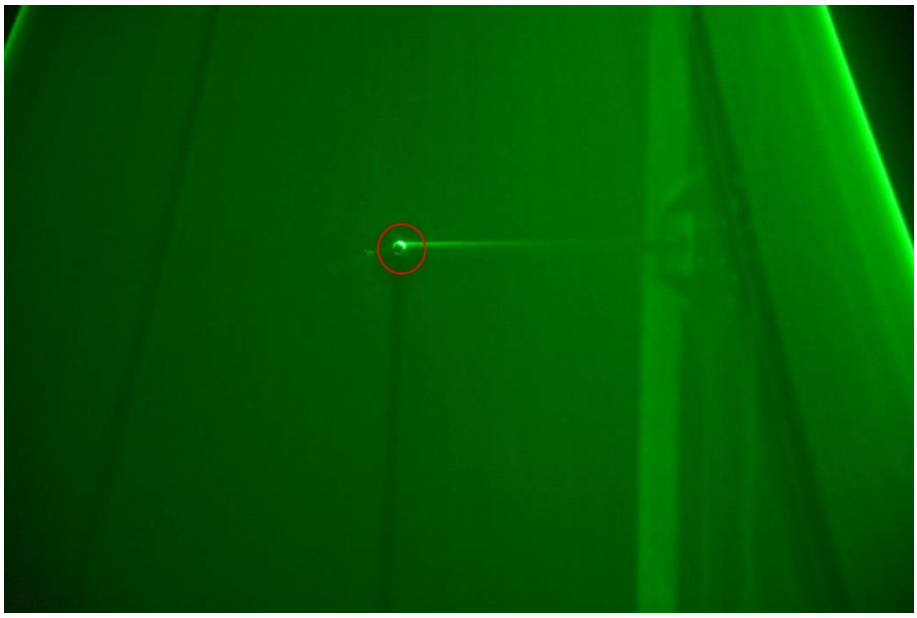

Figure 32 crosswise flow visualization during probe insertion 14 chord lengths downstream at a tunnel speed of 30m/s

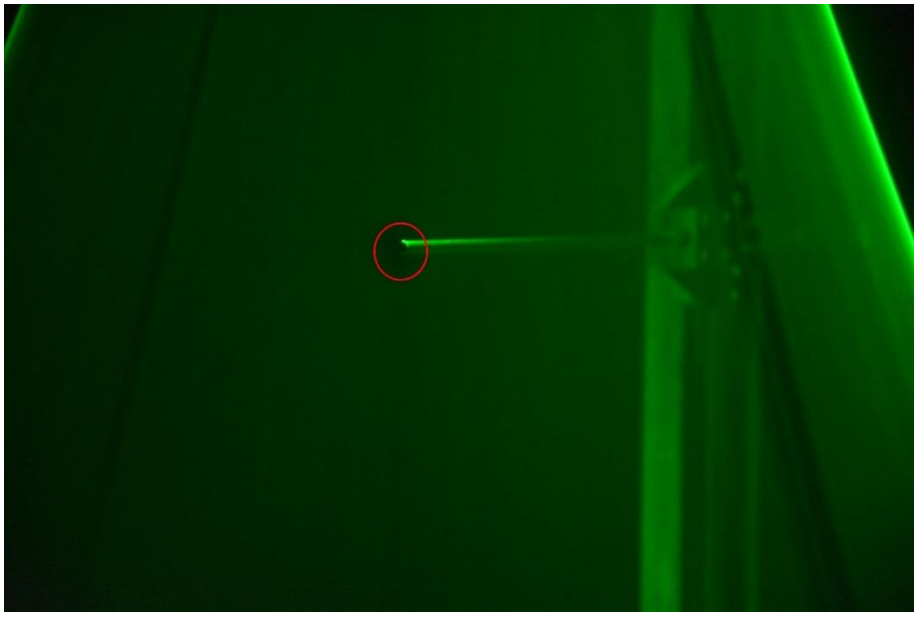

Figure 33 crosswise flow visualization during probe insertion 14 chord lengths downstream at a tunnel speed of 40m/s

Tunnel Speed	Probe Status	Diameter Of Vortex	Distance From Top
30 m/s	Out	323	1616
	in	347	1592
40 m/s	out	383	1604
	in	383	1592

Table 19 Statistics prior to and after probe insertion during crosswise flow visualization, 14 chord lengths downstream from the vortex generator

In all cases the results for the indicated core diameter expansion resulting from the probe insertion fell within the expected core diameter measurement uncertainties. In some cases, the image with the probe inserted had a smaller core diameter than the one observed before the probe was inserted. This indicated that the driving forces behind the diameter fluctuations observed in the image studies continued to be the dominant mechanism influencing the vortex, when compared with probe-derived distortion. Probe insertion has a minimal enough effect on the structure of the vortex to make detailed velocity studies with a hotwire anemometer possible.

3.2 Velocity Vector Fields

Plots of the spatial mean velocity vector distributions generated from the hotwire surveys were employed to establish the location of the rotational axis and then the structure of the axial vortex within a given survey plane. The vector plots were also used to evaluate the state of development of the vortex. If the wing root trailing vortices were not fully merged at a given downstream location, the vector plots exhibited multiple centers of rotation, as shown in Figure 34. That plot was generated from data collected in the survey plane located seven chord lengths downstream from the vortex generator trailing edges, with a wind tunnel velocity of 40 m/s. Figure 34 does not display the entire vector survey plane, focusing instead on the high-density survey locations near the center of the wind tunnel. When the shed vortex pairs have fully merged, the

full field, mean velocity vector plots exhibit clearly a single vortex center of rotation, as shown in Figures 35 through 39.

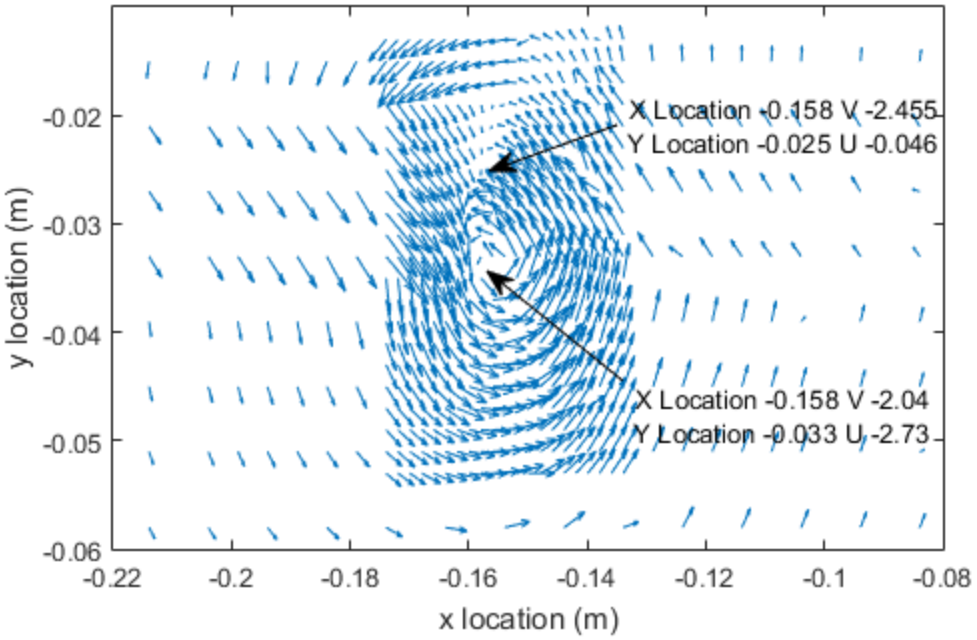

Figure 34 Mean velocity vector field seven chord lengths behind bi-wing generator, free stream velocity of 40 m/s displaying partially-merged co-rotating vortices

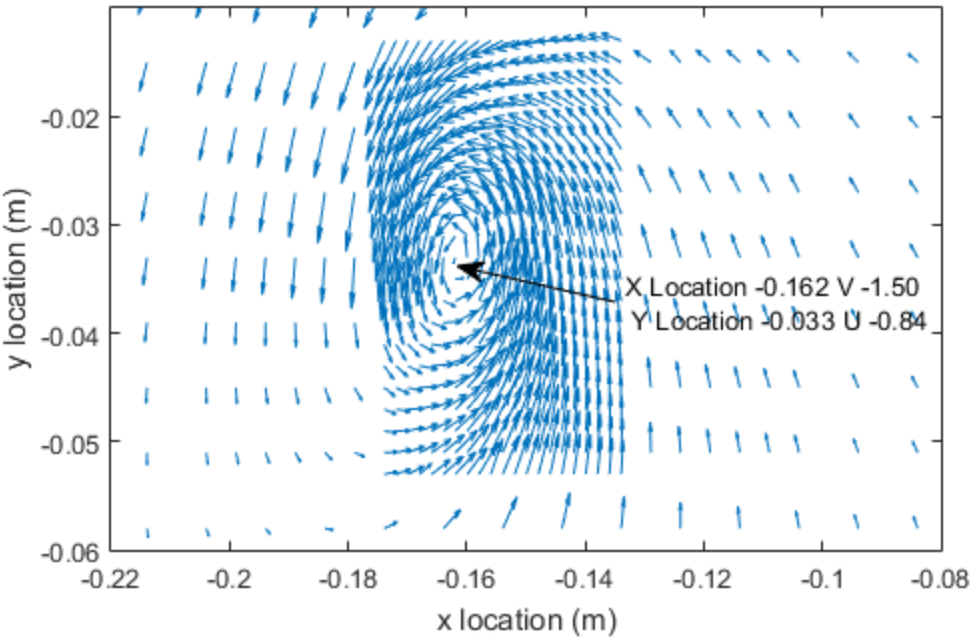

Figure 35 Mean velocity vector field at 7 chord lengths and a free stream velocity of 30 m/s, showing distinct center of rotation

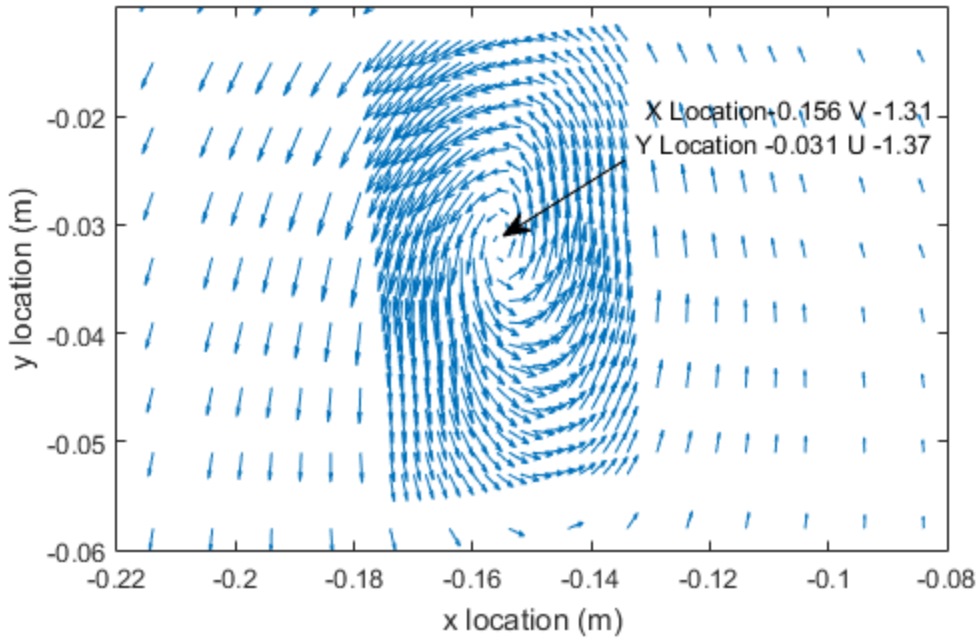

Figure 36 Mean velocity vector field at 10.5 chord lengths and a free stream velocity of 30 m/s, showing the center of rotation

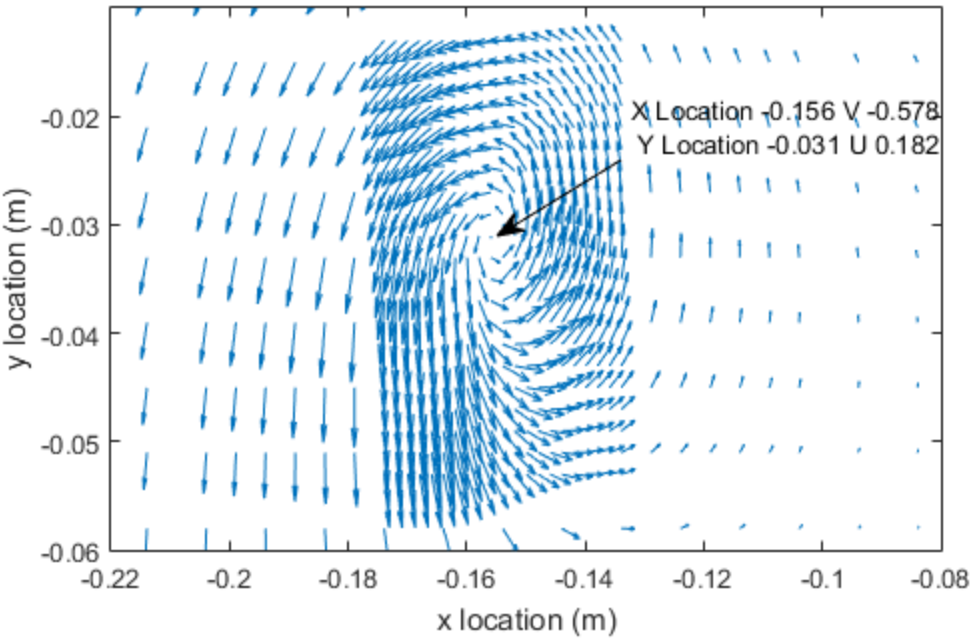

Figure 37 Mean velocity vector field at 14 chord lengths and a free stream velocity of 30 m/s, showing the center of rotation

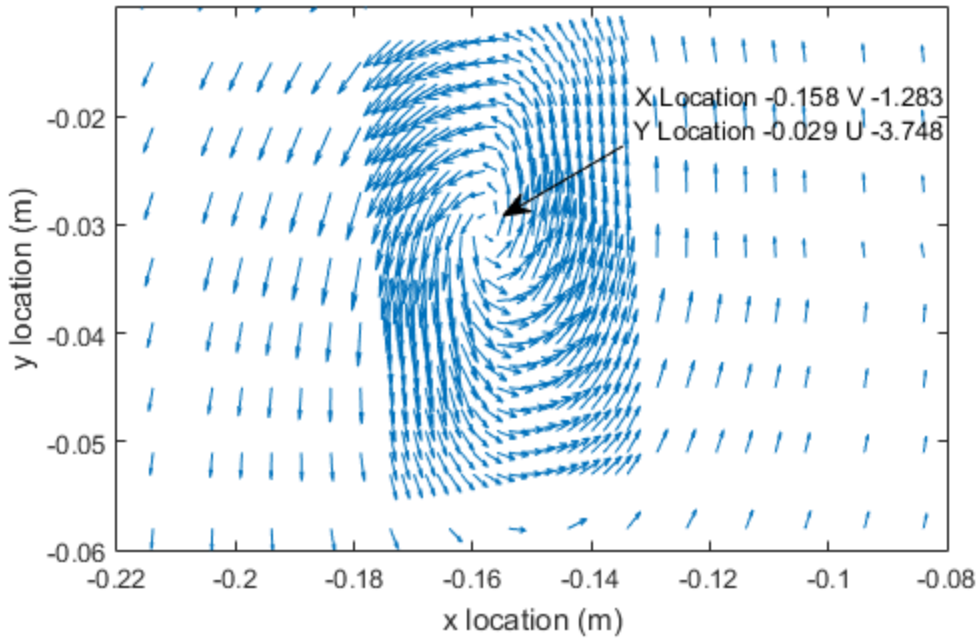

Figure 38 Mean velocity vector field at 10.5 chord lengths and a freestream velocity of 40 m/s, showing the center of rotation

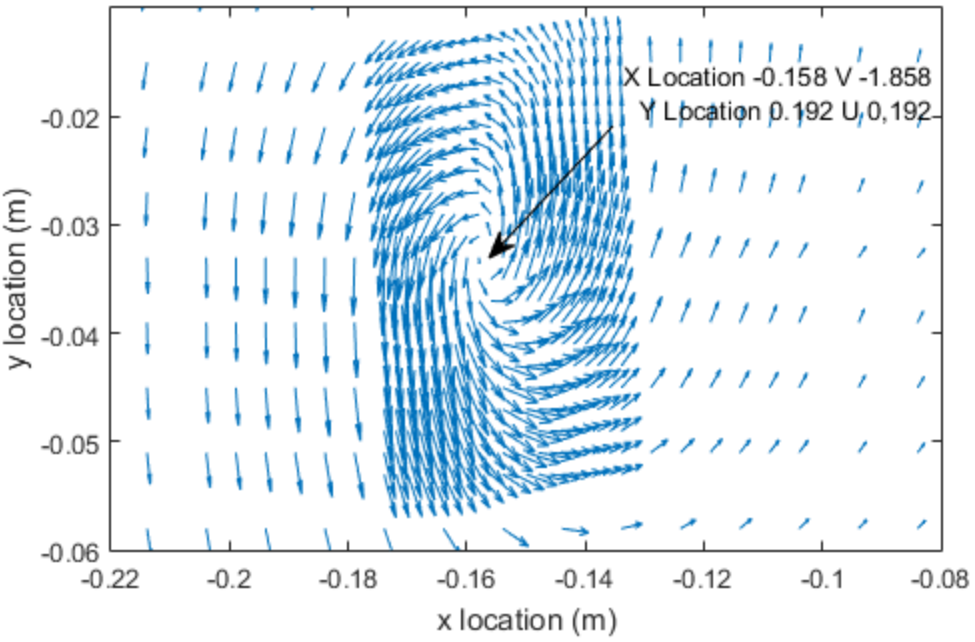

Figure 39 Mean velocity vector field at 14 chord lengths and a free stream velocity of 40 m/s, with the center of rotation shown

The high-density survey locations in the core region were evenly spaced at 2 mm intervals, both vertically and horizontally. On that basis, the actual center of rotation could only be resolved to within ±2 mm, and the rotational center was considered to be the grid location where the in-plane velocity magnitude was a minimum. . These approximate rotational axis locations varied slightly with respect to the wind-tunnel-fixed survey coordinates, but the rotational centerline locations were all within 4 mm of the wind-tunnel-based, cross sectional centerline. This indicated that the fully-developed axial vortices were spatially stable to within ± 2 mm. Variations in the location of the vortex centerline were slight but when they were observed, the vortex axis appeared to be migrating gradually toward the centerline of the wind tunnel. These spatial rotational axis

locations were used to fix local cylindrical coordinates and generate radial mean velocity surveys utilizing the x- and y- survey planes. Additionally, since this study was concerned only with so-called fully-developed axial vortices, the velocity surveys of interest were the fully-formed, single rotational axis profiles, and the survey displayed in Figure 34, located seven chord lengths behind the vortex generator, with a wind tunnel speed of 40 m/s, was excluded from more-detailed analysis.

3.3 Mean Azimuthal Velocity Profiles

The mean azimuthal velocity profile corresponds with the mean vertical velocity profile when the horizontal mean velocity survey axis passes through the minimum velocity point. This single line of survey data was useful because it represented the best approximation of the mean azimuthal velocity, v_θ, resulting from these X-wire surveys, since the vertical or v-component of velocity along that horizontal survey line corresponds with $v = v_\theta$. The mean span wise velocity profiles corresponded with the mean azimuthal velocity profiles along the vertical survey line that passed through the location of the minimum velocity. This single vertical survey line was useful because, like the horizontal survey line of vertical velocities that passed through the minimum velocity point, it represented the best approximation of the mean azimuthal velocity v_θ.

Since the pressure relaxation coefficient in air varies significantly with the temperature and relative humidity of the air, one goal of this research was to examine the influence of air temperature and relative humidity on the vortex structure. That influence can be inferred using the measured maximum swirl velocity and vortex core diameter. Consequently, the most-central vortex survey location and the locations of the maximum and minimum azimuthal velocity peaks, which define the core boundary, have been identified in the plots that follow. Figures 40 through

44 each contain the horizontal and vertical survey profiles that are the best approximations of the mean azimuthal velocities at those survey stations.

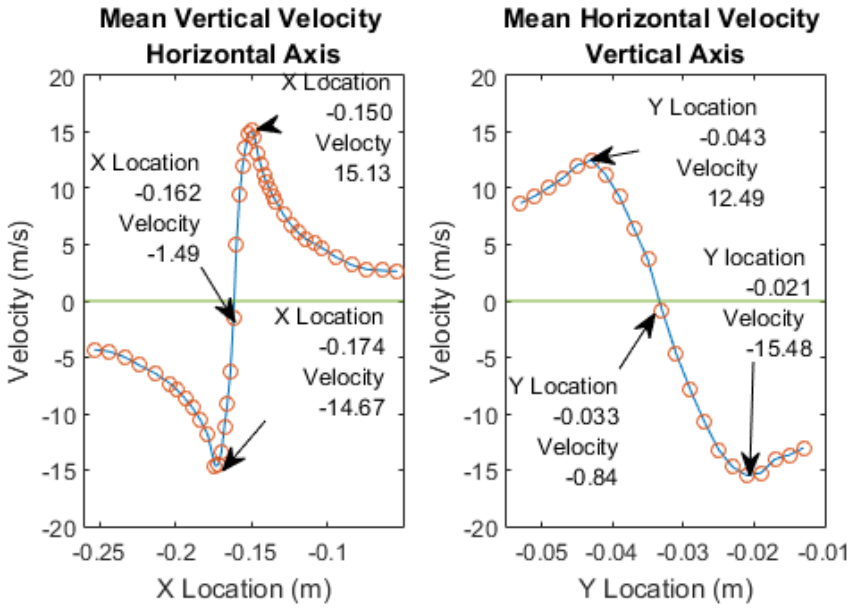

Figure 40 Mean vertical and horizontal velocity profiles along the x- and y- axes respectively at 7 chord lengths downstream of the vortex generator and a freestream velocity of 30 m/s. Along the x axis the nominal temperature was 25° C and the nominal relative humidity was 6.6%, along the y axis the nominal temperature was 27.8° C and the nominal Relative humidity was 8.3%

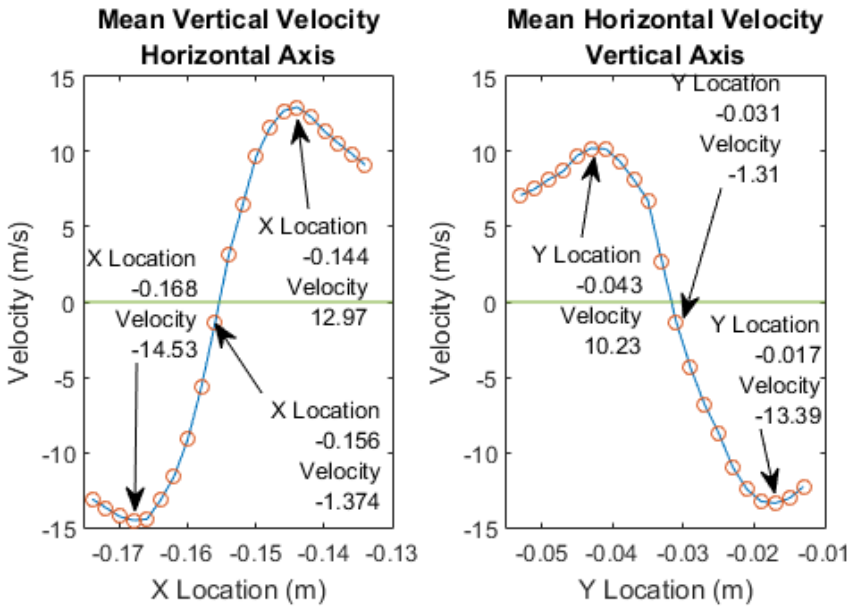

Figure 41 Mean vertical and horizontal velocity profiles along the x and y axis respectively at 10.5 chord lengths downstream of the vortex generator and a freestream velocity of 30 m/s. During the x axis survey the nominal temperature was 24.8° C and the nominal relative humidity was 32.1%, during the y axis survey the nominal temperature was 27.5° C and the nominal Relative humidity was 17.7%

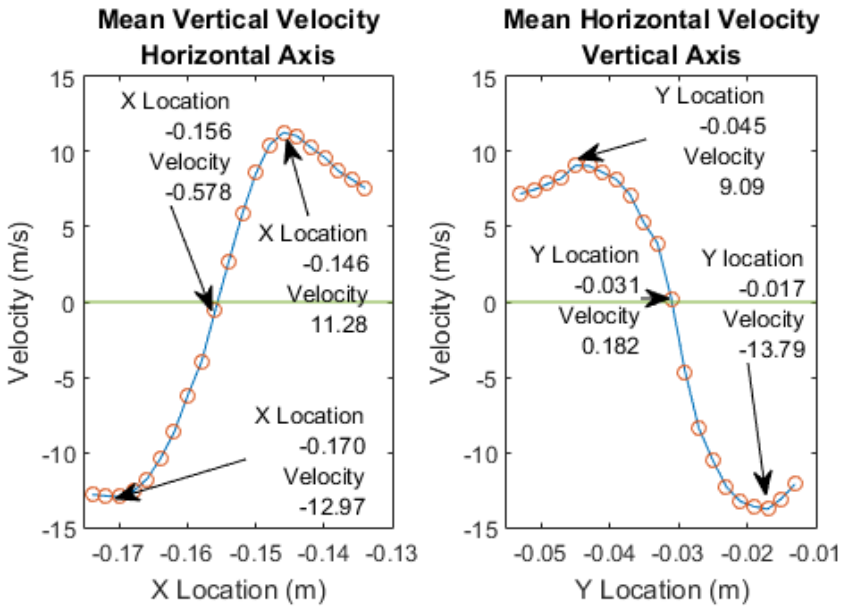

Figure 42 Mean vertical and horizontal velocity profiles along the x and y axis respectively at 14 chord lengths downstream of the vortex generator and a freestream velocity of 30 m/s. During the x axis survey the nominal temperature was 24.7° C and the nominal relative humidity was 17.9%, during the y axis survey the nominal temperature was 27.2° C and the nominal Relative humidity was 16.3%

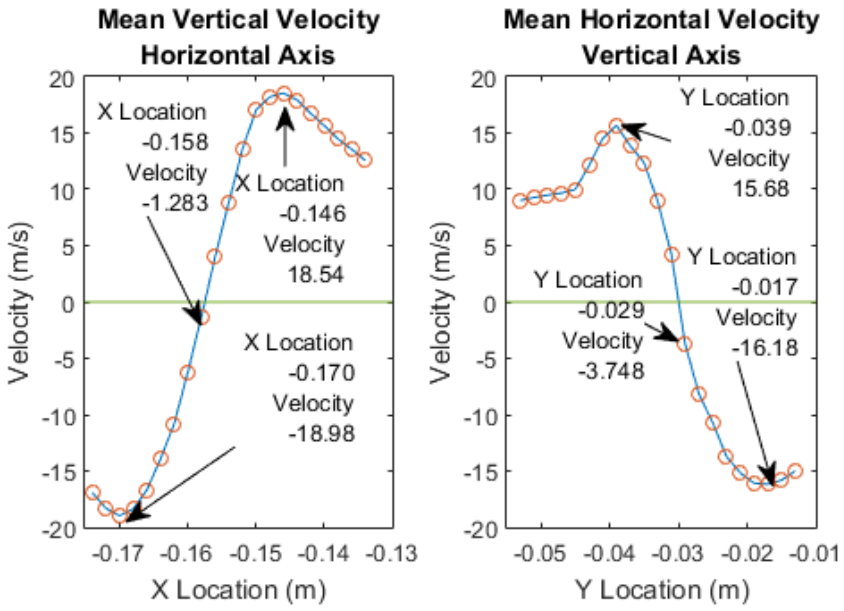

Figure 43 Mean vertical and horizontal velocity profiles along the x and y axis respectively at 10.5 chord lengths downstream of the vortex generator and a freestream velocity of 40 m/s. During the x axis survey the nominal temperature was 30.8° C and the nominal relative humidity was 14.1%, during the y axis survey the nominal temperature was 35.0° C and the nominal Relative humidity was 10.9%

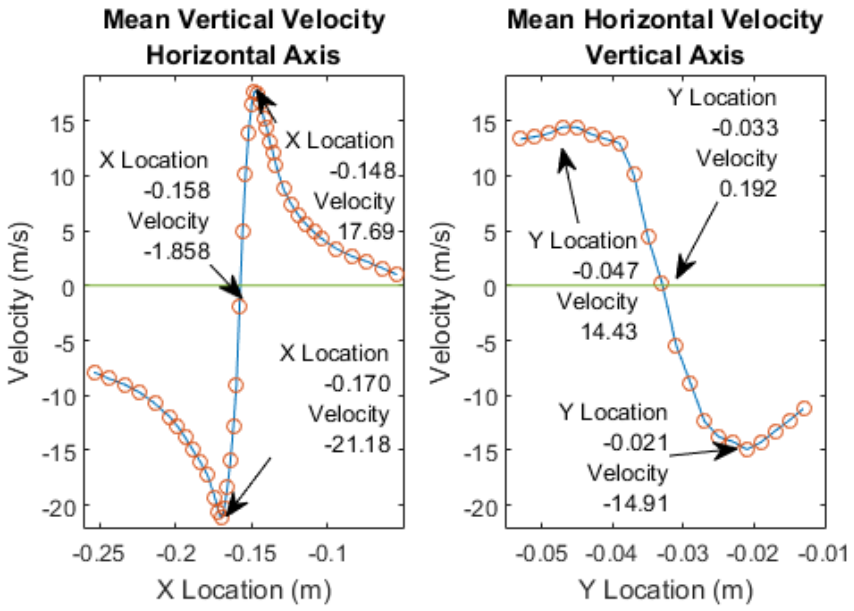

Figure 44 Mean vertical and horizontal velocity profiles along the x and y axis respectively at 14 chord lengths downstream of the vortex generator and a freestream velocity of 40 m/s. During the x axis survey the nominal temperature was 26.2° C and the nominal relative humidity was 13.7%, during the y axis survey the nominal temperature was 35.2° C and the nominal Relative humidity was 9.9%

As will be discussed later, the axial velocity component varies radially and with downstream location. Theoretically-based, steady-state azimuthal velocity profile models assume that the axial velocity is constant, usually zero, and there are fundamental questions related to how the axial velocity (deficit in this case) behavior is coupled with the azimuthal velocity component. However, it is instructive to examine how the vortex core size, based on the maximum azimuthal velocity peaks, varies with downstream distance. Those data are summarized in Table 20.

$\bar{Z}$	V	x-ctr	y-ctr	Dh	Dv
7	30 m/s	-162 mm	-33 mm	24 mm	22 mm
10.5	30 m/s	-156 mm	-31 mm	24 mm	24 mm
14	30 m/s	-156 mm	-31 mm	24 mm	26 mm
10.5	40 m/s	-158 mm	-29 mm	22 mm	22 mm
14	40 m/s	-158 mm	-33 mm	22 mm	26 mm

Table 20 Vortex statistics based on azimuthal velocity surveys

The hot-film velocity surveys were effected using horizontal traverses, followed by a vertical traverse at the end of each horizontal sweep. As a result, there is a large time interval, typically between 5 and 10 minutes depending on the number of data points collected, along a given row of the survey grid. Since the wind tunnel temperature increases over time, this time delay produces more scatter in results obtained along the vertical axis (separated by the time required to perform at least one horizontal survey sweep). Despite these temperature effects, the vortex at seven chord lengths downstream from the vortex generator, and at a wind tunnel velocity of 30 m/s, clearly displays the positive and negative peaks associated with a fully-developed axial vortex. As with the horizontal surveys, it was observed that the location of the vortex centerline was very close to the local wind tunnel centerline, allowing for the offset in the position of the bi-wing vortex generator. At 10.5 chord lengths downstream, the centerline location of the vortex shifted 2 mm towards the center of the tunnel, and, when compared with the vortex diameter measured at seven chord lengths, grew by 2 mm to 24 mm. At 14 chord lengths downstream from the vortex generator, the vortex centerline location, was the same as that observed at 10.5 chord

lengths. The vortex diameter at 14 chord lengths grew by an additional 2 mm, to 26 mm. The location of the vortex centerline shifted minimally at the stations observed at a tunnel velocity of 30 m/s. The shift in centerline location was consistent with the shift observed in the horizontal survey, further indicating that the vortex was stable spatially while moving gradually toward the center of the wind tunnel cross section. The diameter of the vortex gradually grew as it convected downstream. However, as the observed growth was small at approximately 2 mm every 3.5 chord lengths for a total growth of 4 mm in the entire length of the test section this was close to a fully developed axial vortex approximation.

At a wind tunnel speed of 40 m/s, the velocity survey, at seven chord lengths, showed that the flow had not fully merged into a single vortex and that survey was not analyzed beyond the vector plot. At a distance of 10.5 chord lengths, the centerline was observed to be in close proximity to the tunnel centerline, with the offset being due to the vortex generator not being exactly centered in the tunnel. At 14 chord lengths, the vortex axis had shifted 4 mm away from the tunnel centerline and had grown in diameter by 2 mm from the diameter measure at 10.5 Chord lengths and a tunnel velocity of 40 m/s. This growth was small enough over the distance that the vortex could be considered to approximate a steady, fully-developed flow condition. The shift away from the centerline was a change from other shifts observed. This could be due to a long period oscillation or some other phenomena that these measurements were unable to isolate.

3.4 Mean Axial Velocity Profiles

The mean streamwise or axial velocity profiles were useful in determining the magnitude of the velocity deficit created by the wake of the vortex generator and if the stream wise velocity is influenced by the azimuthal velocities, radial velocities or downstream location as it progresses down the wind tunnel. The horizontal and vertical surveys provided two different mean axial velocity perspectives. Figures 45 through 49 contain these profiles for each survey location and speed.

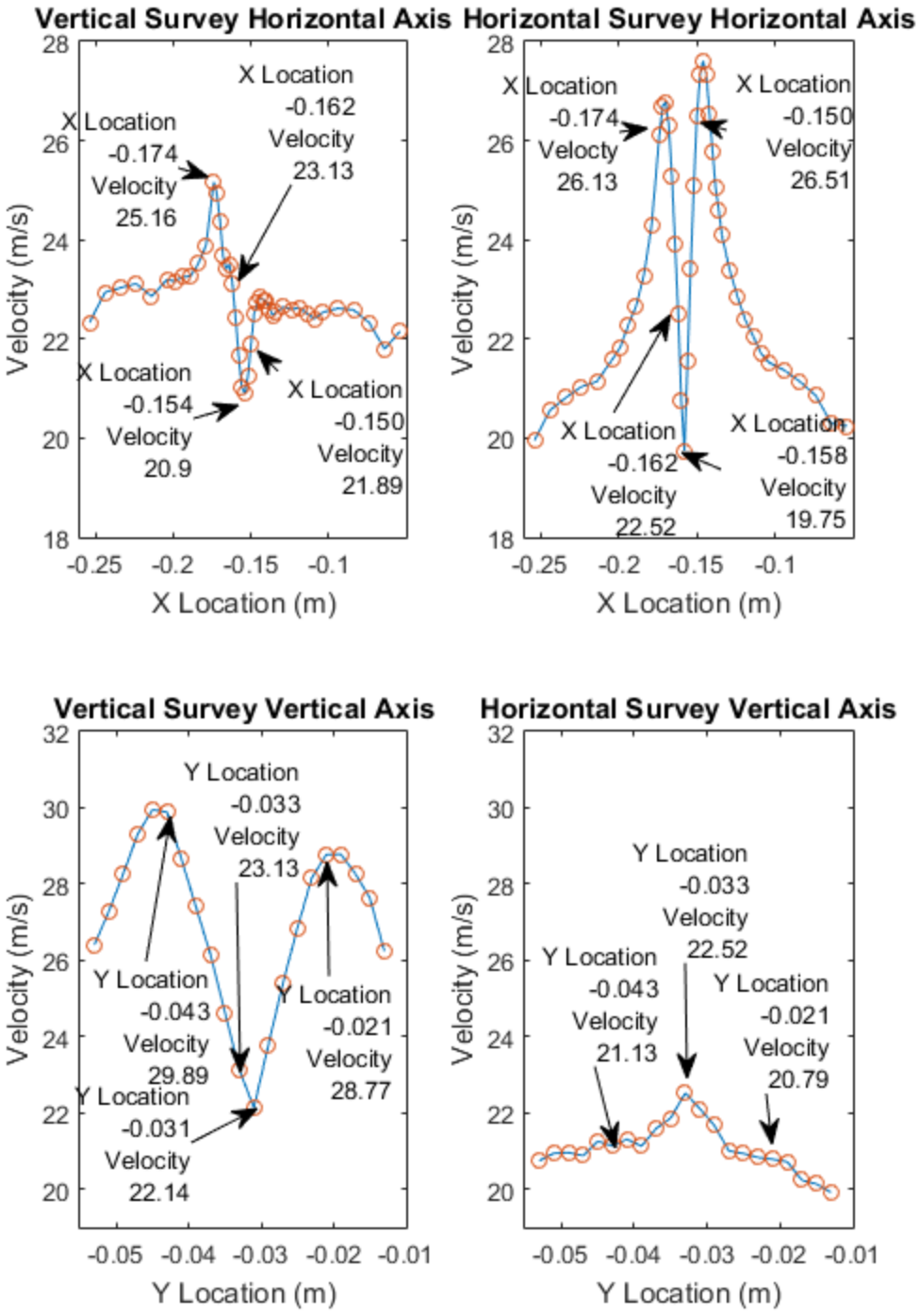

Figure 45 Mean axial velocity profiles at seven chord lengths downstream from the vortex generator and a tunnel velocity of 30 m/s. The locations of the peak azimuthal velocities, center of rotation and the maximum velocity deficit if present have been shown

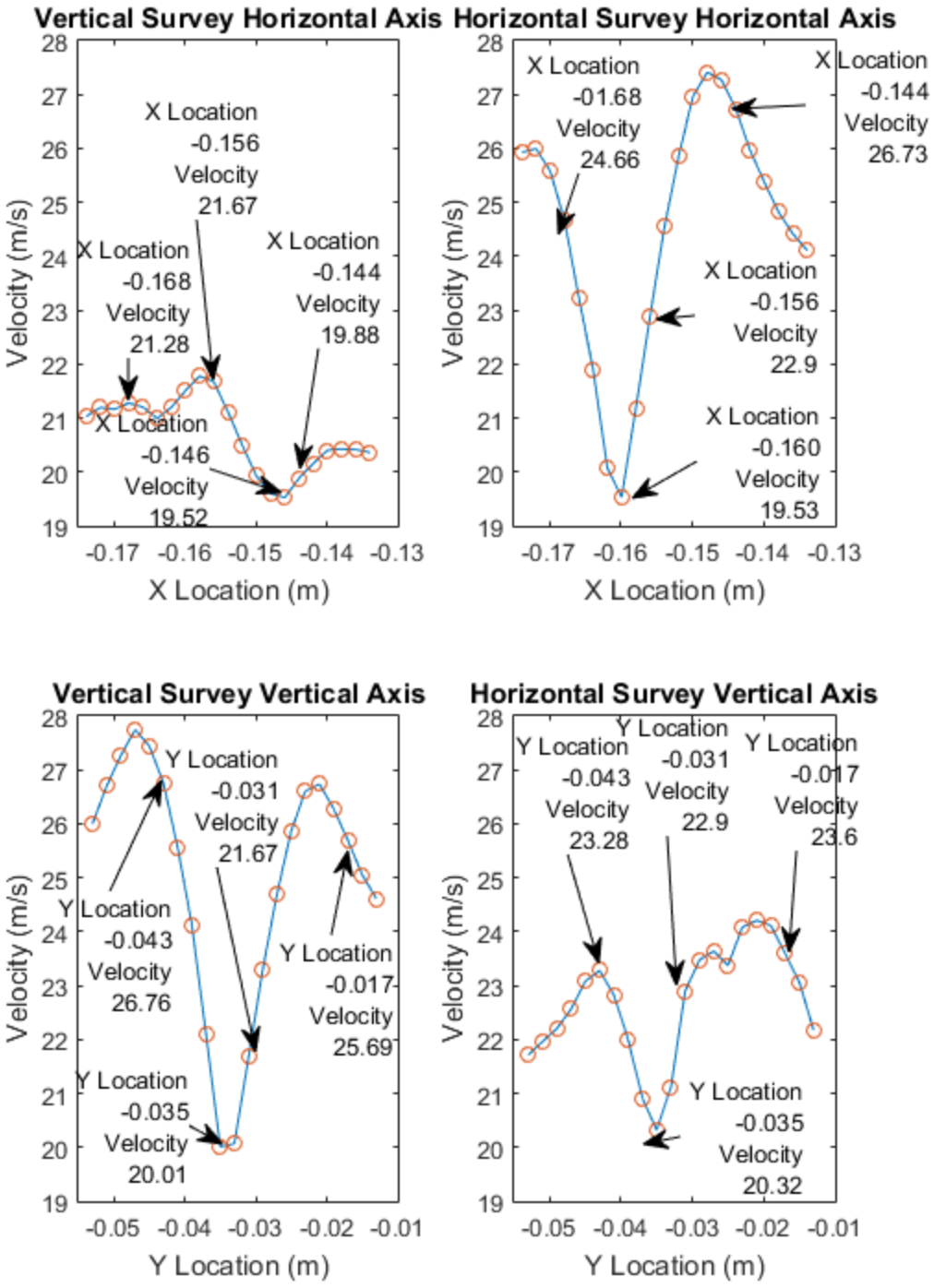

Figure 46 Mean axial velocity profiles at 10.5 chord lengths downstream from the vortex generator and a tunnel velocity of 30 m/s. The locations of the peak azimuthal velocities, center of rotation and the maximum velocity deficit have been shown

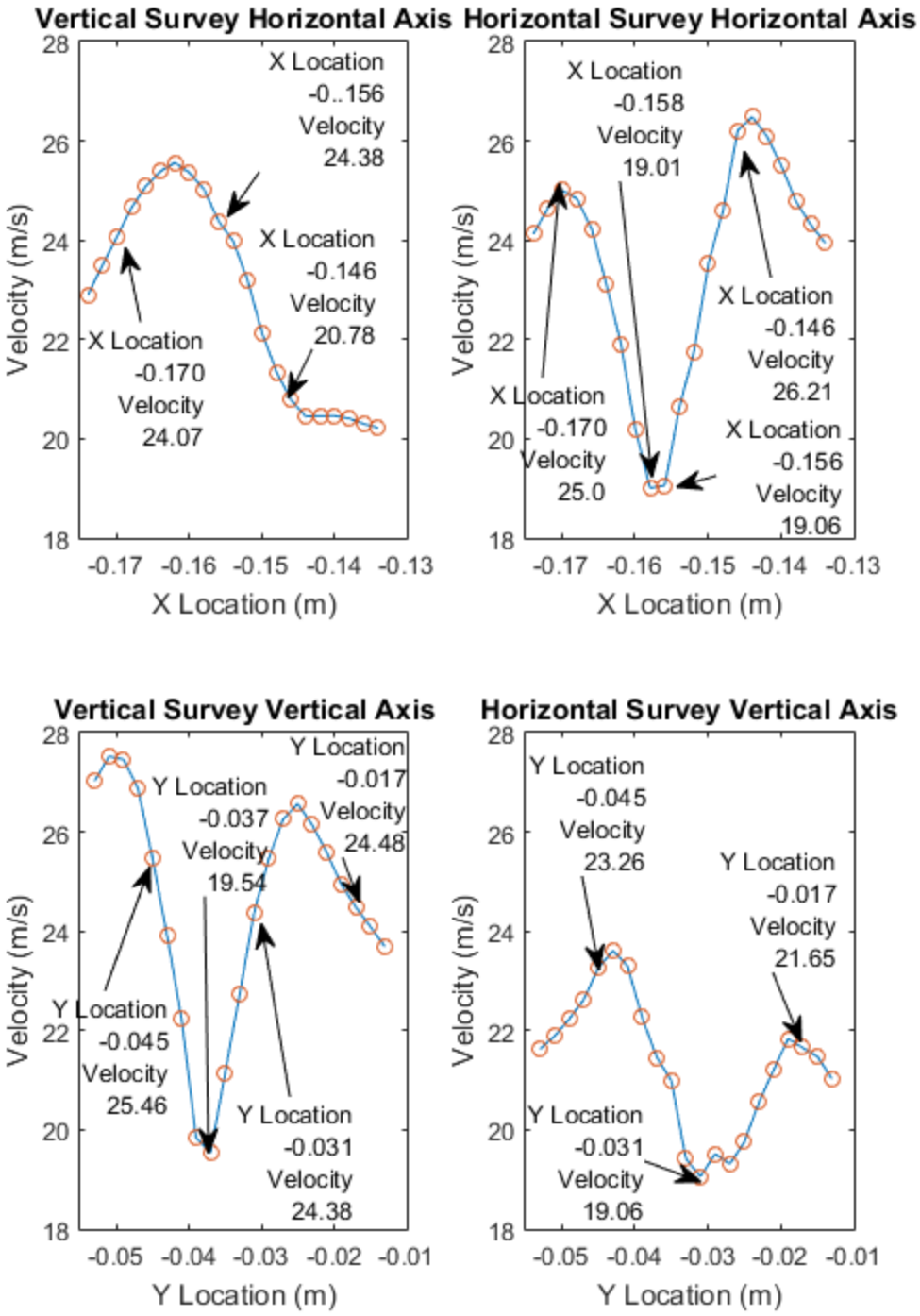

Figure 47 Mean axial velocity profiles at 14 chord lengths downstream from the vortex generator and a tunnel velocity of 30 m/s. The locations of the peak azimuthal velocities, center of rotation and the maximum velocity deficit have been shown.

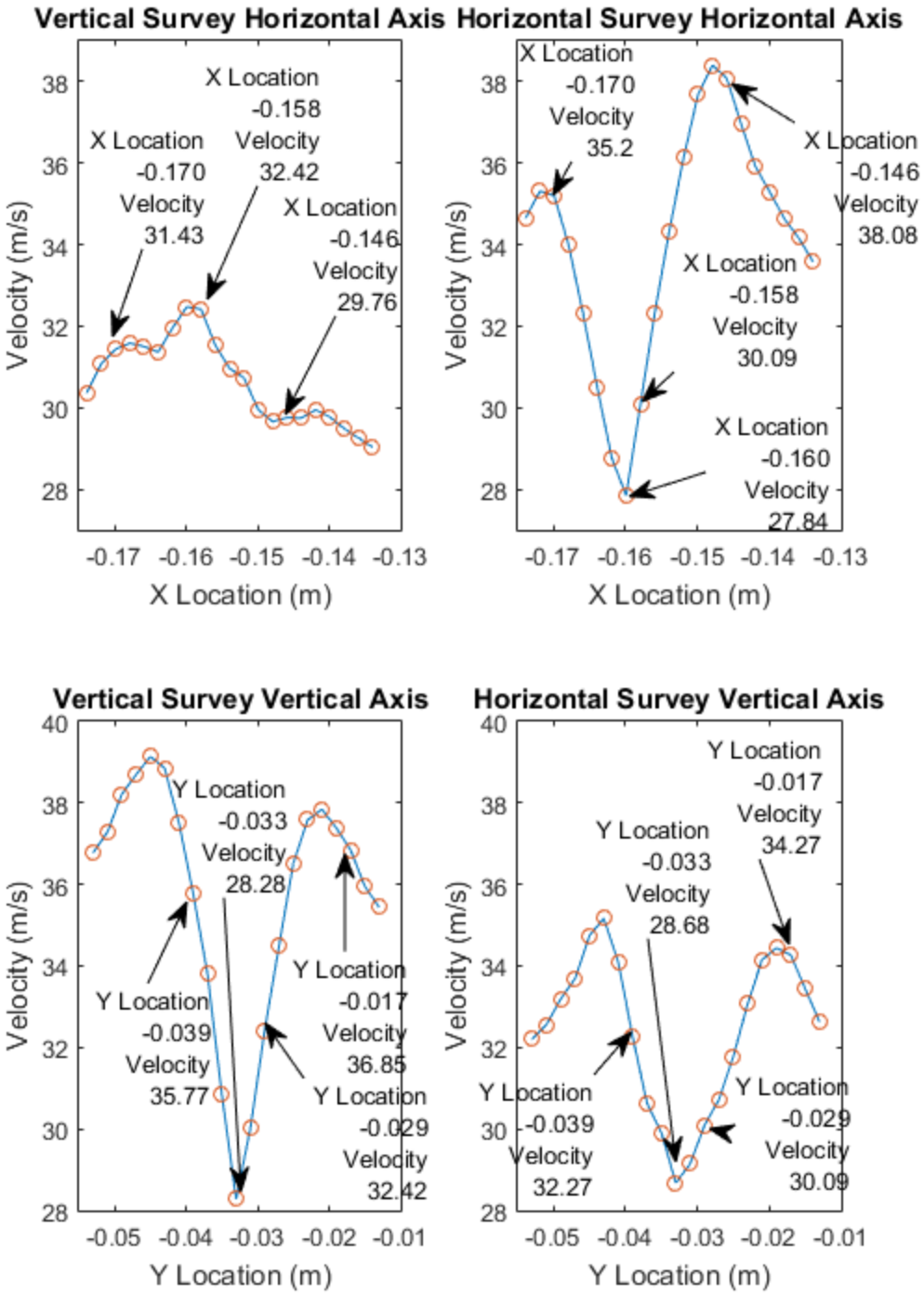

Figure 48 Mean axial velocity profiles at 10.5 chord lengths downstream from the vortex generator and a tunnel velocity of 40 m/s. The locations of the peak azimuthal velocities, center of rotation and the maximum velocity deficit have been shown.

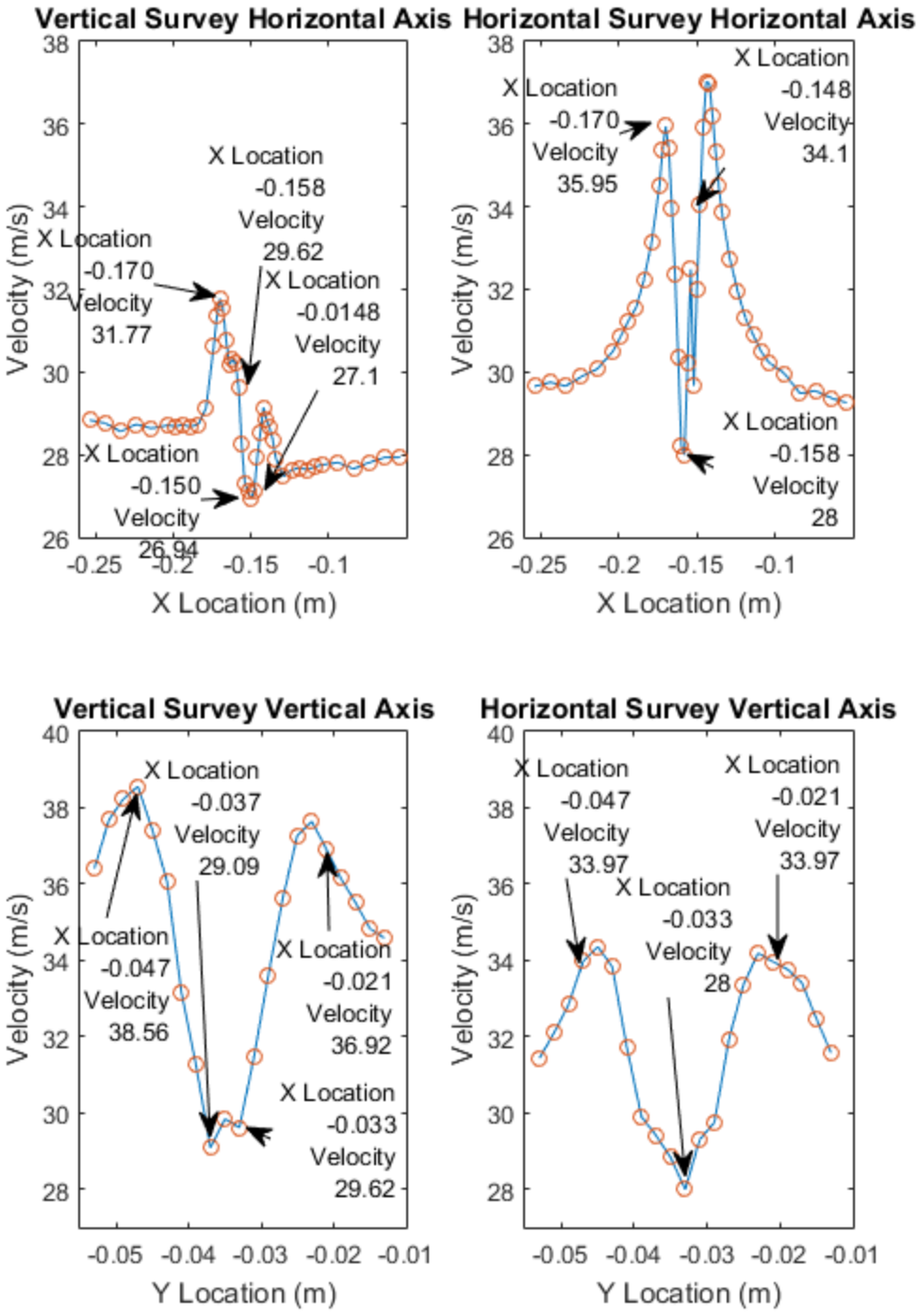

Figure 49 Mean axial velocity profiles at 14 chord lengths downstream from the vortex generator and a tunnel velocity of 40 m/s. The locations of the peak azimuthal velocities, center of rotation and the maximum velocity deficit have been shown.

At 30 m/s, the axial velocity profiles displayed velocities lower than the tunnel velocity through most of the survey with the largest deficits occurring inside the vortex core close to the center of rotation. Most of the profiles display a jet like peak in axial velocity in close proximity to both core boundaries observed in the survey. There were some notable exceptions to this, as can be seen in Figure 47 for the horizontal survey along the vertical axis where the profile is largely flat and during the vertical survey along the horizontal axis where there is one large peak. In Figure 48 where the vertical survey along the horizontal axis is largely flat, and Figure 49 where the vertical survey along the horizontal axis displays a large peak. The combinations of some profiles being largely flat and others only displaying a single peak while the majority displayed two jet like peaks indicated that the generation of these jet like peaks may be cyclical and the peaks were initially generated on one side of the vortex, then convected around the core by the azimuthal velocity.

At 40 m/s, the axial velocity profiles were similar to those observed at 30 m/s. With a large velocity deficit close to the center of rotation and jet like velocity peaks close the core boundary. In Figure 48 the vertical velocity survey along the horizontal axis displayed a largely flat axial velocity profile, the horizontal survey along the vertical axis displayed two peaks of different magnitudes generated along one side of the vortex and convected by the azimuthal velocity around the vortex core, and in figure 49 the vertical survey along the horizontal axis displayed two peaks of different velocities indicating that the jet like peaks are not always constant in strength. The presence of a largely flat velocity profile and peaks of varying velocities further indicated that the jets were formed on one side of the vortex and convected around the vortex core by the azimuthal velocity. The fact that there are jet like peaks in the velocity that are varying in magnitude indicated that the jets weren't always the same strength when they were formed. These peaks observed in

the vortices at both 30 m/s and 40 m/s were likely formed due to the process of merging the two co-rotating wing root vortices.

3.5 Radial Velocity Profile Approximations

The mean radial velocity profile corresponds with the mean horizontal velocity profile when the horizontal mean velocity survey axis passes through the minimum velocity point. This single line of survey data was useful because it represented the best approximation of the mean radial velocity, v_r, since the horizontal or u-component of velocity along that horizontal survey line was $u = v_r$. The mean vertical velocity profiles corresponded with the mean radial velocity profiles along the vertical survey line that passed through the location of the minimum velocity. Like the horizontal survey line of horizontal velocities that passed through the minimum velocity point it represented the best approximation of the mean radial velocity v_r, since the vertical or v-component of velocity along that vertical survey line was $v = v_r$. Since a goal of this research was to examine the interactions of the radial component of velocity, with the azimuthal and axial components of velocity it is useful to know which survey locations coincide with the locations of the peak azimuthal velocities and the center or rotation. Consequently, the most-central vortex survey location and the locations of the maximum and minimum azimuthal velocity peaks which define the core boundary locations have been identified in the plots that follow.

Due to the effects of large velocity means in the insensitive axis of measurement it was necessary to develop a method similar to Shabbir, Beuther, George (1995) in order to use the data gathered during the hotwire surveys to construct an approximation of the radial profiles. The effective cooling velocity can be related to the X-plane velocity components, u and v, and the cross-plane velocity w, using

$$U_{eff}^2 = (u\cos\alpha + v\sin\alpha)^2 + k^2(u\sin\alpha - v\cos\alpha)^2 + w^2 \qquad (28)$$

where α is the angular orientation of a sensing filament with respect to the primary sensing direction of the X-probe, and k is a calibration coefficient. Since it is assumed that the sensing element only responds to X-plane velocities, the effective cooling velocity as measured by a sensing element can be expressed in terms of a so-called "measured velocity components", i.e.

$$U_{eff}^2 = (u_m \cos\alpha + v_m \sin\alpha)^2 + k^2(u_m \sin\alpha - v_m \cos\alpha)^2 \quad (29)$$

Therefore,

$$(u\cos\alpha + v\sin\alpha)^2 + k^2(u\sin\alpha - v\cos\alpha)^2 + w^2 = (u_m\cos\alpha + v_m\sin\alpha)^2 + k^2(u_m\sin\alpha - v_m\cos\alpha)^2 \quad (30)$$

The manufacturer-specified sensing element orientations are ± 45 degrees. Substituting the appropriate ± 45 into the two sensor element equations yields:

$$(u+v)^2 + k^2(u-v)^2 + 2w^2 = (u_m + v_m)^2 + k^2(u_m - v_m)^2 \quad (31)$$

$$(u-v)^2 + k^2(u+v)^2 + 2w^2 = (u_m - v_m)^2 + k^2(u_m + v_m)^2 \quad (32)$$

Treating the actual velocities as known values and the measured velocities as unknowns, these equations can be combined to produce a pair of equations for the measured velocities. One relation between the measured and true u and v velocity components is:

$$u_m v_m = uv \quad (33)$$

Equation (33) was employed to eliminate v_m from equation (31). The resulting quadratic equation for u_m^2 was

$$u_m^4 - u_m^2\left(u^2 + v^2 + \frac{2w^2}{1+k^2}\right) + u^2v^2 = 0 \quad (34)$$

This equation has a positive root given by:

$$u_m^2 = \frac{1}{2}\left(u^2 + v^2 + \frac{2w^2}{1+k^2}\right) + \frac{1}{2}\sqrt{\left(u^2 + v^2 + \frac{2w^2}{1+k^2}\right)^2 - 4u^2v^2} \tag{35}$$

which yields the correct relation when $w = 0$. In order to obtain an equation for the mean measured velocity, we need;

$$u_m = \sqrt{\frac{1}{2}\left(u^2 + v^2 + \frac{2w^2}{1+k^2}\right) + \frac{1}{2}\sqrt{\left(u^2 + v^2 + \frac{2w^2}{1+k^2}\right)^2 - 4u^2v^2}} \tag{36}$$

Now,

$$\begin{aligned}
&\frac{1}{2}\sqrt{\left(u^2 + v^2 + \frac{2w^2}{1+k^2}\right)^2 - 4u^2v^2} \\
&\qquad = \frac{1}{2}\left(u^2 + v^2 + \frac{2w^2}{1+k^2}\right)\sqrt{1 - \frac{4u^2v^2}{\left(u^2 + v^2 + \frac{2w^2}{1+k^2}\right)^2}} \\
&\qquad \approx \frac{1}{2}\left(u^2 + v^2 + \frac{2w^2}{1+k^2}\right)\left(1 - \frac{2u^2v^2}{\left(u^2 + v^2 + \frac{2w^2}{1+k^2}\right)^2}\right) \\
&\qquad = \frac{1}{2}\left(u^2 + v^2 + \frac{2w^2}{1+k^2}\right) - \frac{u^2v^2}{u^2 + v^2 + \frac{2w^2}{1+k^2}}
\end{aligned}$$

Employing this approximation in Equation (36) yields

$$u_{m\approx} \sqrt{\frac{1}{2}\left(u^2 + v^2 + \frac{2w^2}{1+k^2}\right) + \frac{1}{2}\left(u^2 + v^2 + \frac{2w^2}{1+k^2}\right) - \frac{u^2v^2}{u^2 + v^2 + \frac{2w^2}{1+k^2}}} \tag{37}$$

$$= \sqrt{u^2 + v^2 + \frac{2w^2}{1+k^2}}\sqrt{1 - \frac{u^2v^2}{\left(u^2 + v^2 + \frac{2w^2}{1+k^2}\right)^2}}$$

This equation can be approximated further utilizing the following:

$$\sqrt{1-\frac{u^2v^2}{\left(u^2+v^2+\frac{2w^2}{1+k^2}\right)^2}} \approx 1-\frac{u^2v^2}{2\left(u^2+v^2+\frac{2w^2}{1+k^2}\right)^2}$$

$$\sqrt{u^2+v^2+\frac{2w^2}{1+k^2}} = \sqrt{u^2\left(1+\frac{v^2+\frac{2w^2}{1+k^2}}{u^2}\right)} \approx u\left(1+\frac{v^2+\frac{2w^2}{1+k^2}}{2u^2}\right)$$

Employing these approximations in equation (37) yields

$$u_m = \sqrt{u^2+v^2+\frac{2w^2}{1+k^2}}\sqrt{1-\frac{u^2v^2}{\left(u^2+v^2+\frac{2w^2}{1+k^2}\right)^2}} \tag{38}$$

$$\approx u\left(1+\frac{v^2+\frac{2w^2}{1+k^2}}{2u^2}-\frac{\left(v^2+\frac{2w^2}{1+k^2}\right)^2}{8u^4}\right)\left(1 - \frac{u^2v^2}{2\left(u^2+v^2+\frac{2w^2}{1+k^2}\right)^2}-\frac{u^4v^4}{8\left(u^2+v^2+\frac{2w^2}{1+k^2}\right)^4}\right)$$

The quadratic and quartic terms in equation (38) should be negligibly small, leaving

$$u_m \approx u\left(1+\frac{v^2+\frac{2w^2}{1+k^2}}{2u^2}-\frac{\left(v^2+\frac{2w^2}{1+k^2}\right)^2}{8u^4}\right) \tag{39}$$

$$\approx u\left(1+\frac{v^2}{2u^2}-\frac{v^4}{8u^4}+\frac{w^2}{u^2(1+k^2)}-\frac{v^2w^2}{2u^4(1+k^2)} - \frac{w^4}{2u^4(1+k^2)^2}\right)$$

Recognizing that the axial velocity component is much larger than the other velocity components, i.e. u>>v , this equation can be scaled utilizing $v/u << 1$ to write

$$u_m \approx u\left(1+\frac{w^2}{u^2(1+k^2)}-\frac{w^4}{2u^4(1+k^2)^2}\right) \tag{40}$$

Applying the Reynolds decomposition $u_m = \overline{u_m} + u'_m, u = \bar{u} + u', v = \bar{v} + v', w = \bar{w} + w'$

$$(\overline{u_m} + u'_m) \approx (\bar{u} + u')\left(1+\frac{(\bar{w}+w')^2}{(\bar{u}+u')^2(1+k^2)}-\frac{(\bar{w}+w')^4}{2(\bar{u}+u')^4(1+k^2)^2}\right) \tag{41}$$

The two terms in the right parentheses were rewritten using a Taylor series expansion about $u' = 0$, then averaged to get

$$\overline{u_m} = \bar{u}\left(1+\frac{\overline{(\bar{w}+w')^2}}{\bar{u}^2(1+k^2)}-\frac{\overline{2\,u'(\bar{w}+w')^2}}{\bar{u}^3(1+k^2)}+\frac{\overline{3\,u'^2(\bar{w}+w')^2}}{\bar{u}^3(1+k^2)} -\frac{\overline{(\bar{w}+w')^4}}{2\bar{u}^4(1+k^2)^2}\ldots\right) \tag{42}$$

Setting $\bar{w} = 0$ in equation (42) yields an equation that is similar to that of Shabbir, Beuther, and George (1995) for $\overline{u_m}$. Using the same process starting with equation (43) to eliminate u_m from equation (31) yields the following equation for v_m.

$$v_m \approx v\left(1+\frac{w^2}{u^2(1+k^2)}-\frac{w^4}{2u^4(1+k^2)^2}\right) \tag{43}$$

The same process was then used to determine the Reynolds averaged version of the equation to get

$$\bar{v}_m = \bar{v}\left(1 + \frac{\overline{(\bar{w}+w')^2}}{\bar{u}^2(1+k^2)} - \frac{\overline{2\,u'(\bar{w}+w')^2}}{\bar{u}^3(1+k^2)} + \frac{\overline{3\,u'^2(\bar{w}+w')^2}}{\bar{u}^3(1+k^2)} - \frac{\overline{(\bar{w}+w')^4}}{2\bar{u}^4(1+k^2)^2}\ldots\right) \quad (44)$$

It was useful to go through the Reynolds decomposition to check the equations against those derived previously by Shabbir, Beuther, George (1995). However, since there is a large out-of-plane mean flow, it was necessary to apply this correction to the instantaneous velocities using equations 40 and 43.

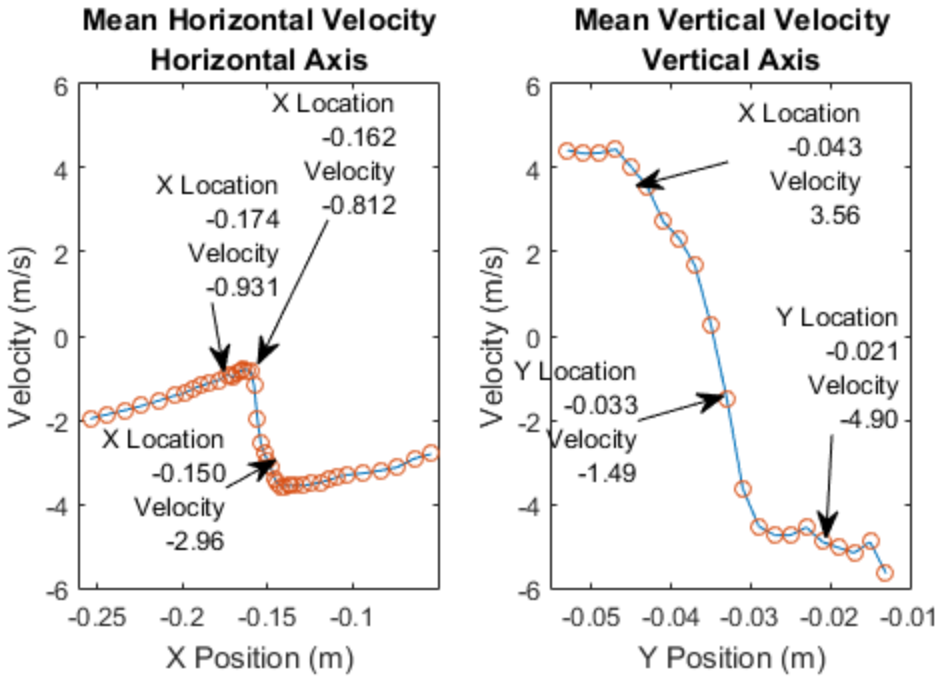

Figure 50 Mean radial velocity profiles at 7 chord lengths downstream of the vortex generator and a tunnel velocity of 30 m/s. The location of the central survey point and the location of the azimuthal velocity peaks have been shown**.**

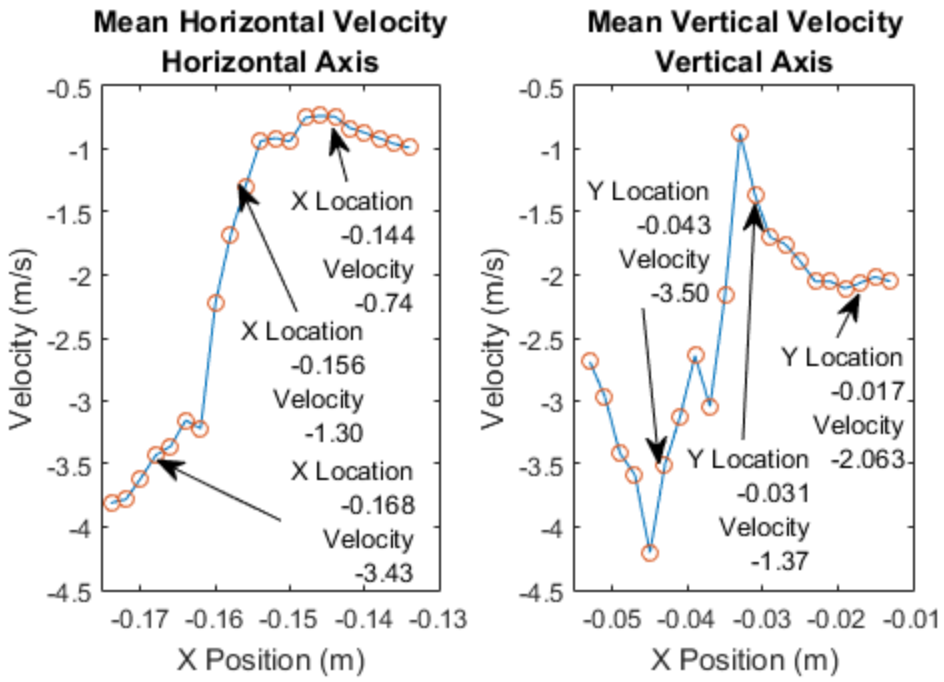

Figure 51 Mean radial velocity profiles at 10.5 chord lengths downstream of the vortex generator and a tunnel velocity of 30 m/s. The location of the central survey point and the location of the azimuthal velocity peaks have been shown.

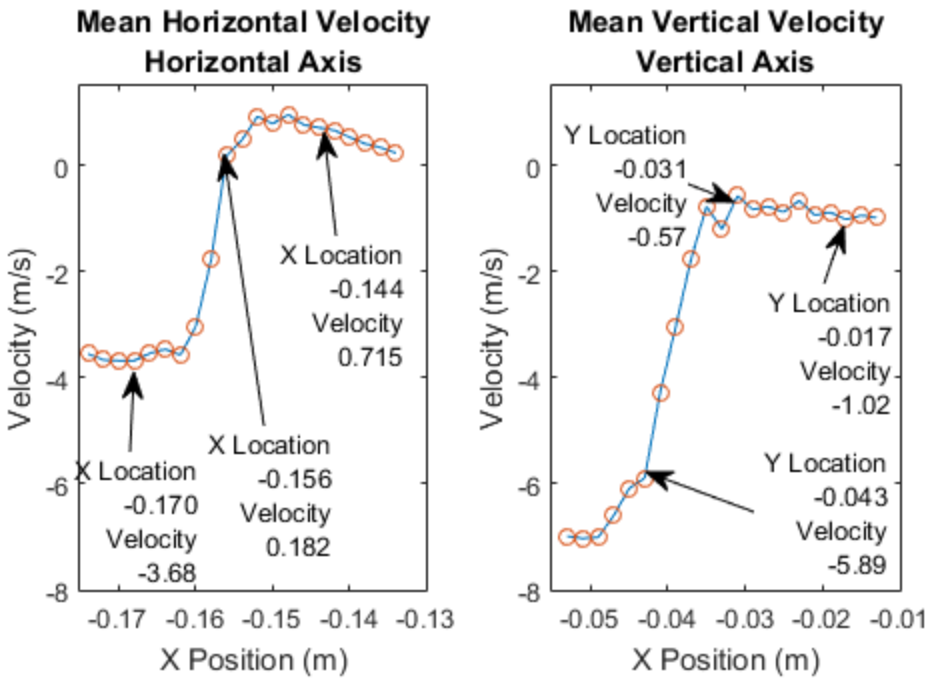

Figure 52 Mean radial velocity profiles at 14 chord lengths downstream of the vortex generator and a tunnel velocity of 30 m/s. The location of the central survey point and the location of the azimuthal velocity peaks have been shown.

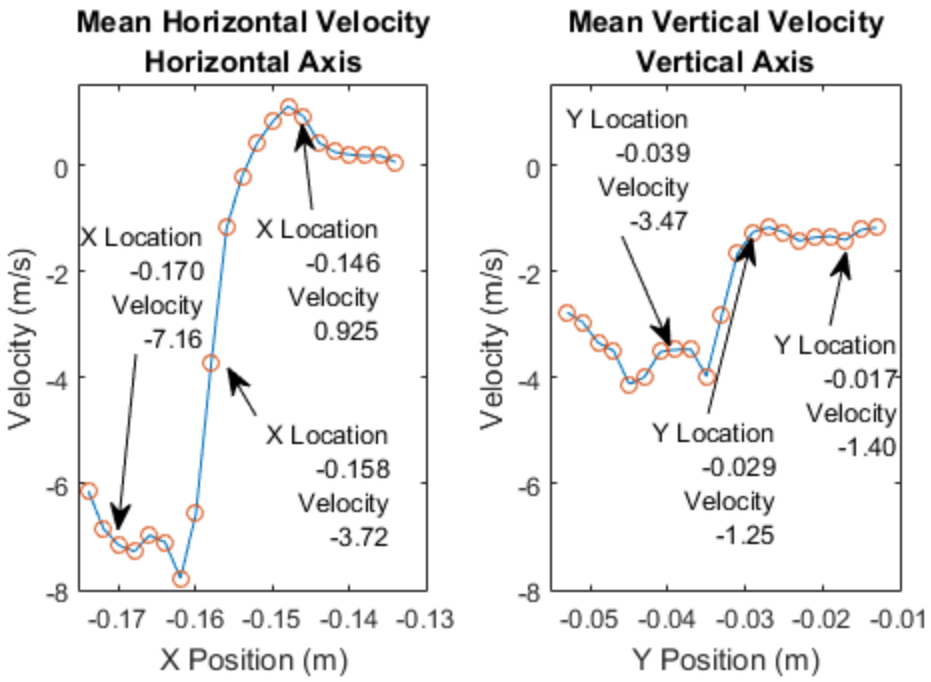

Figure 53 Mean radial velocity profiles at 10.5 chord lengths downstream of the vortex generator and a tunnel velocity of 40 m/s. The location of the central survey point and the location of the azimuthal velocity peaks have been shown.

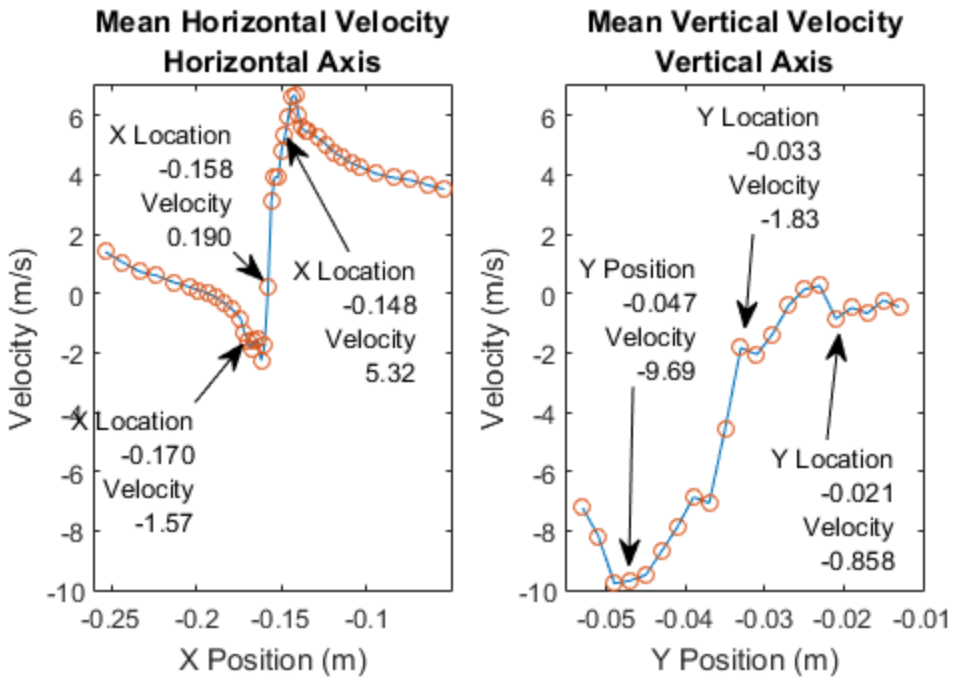

Figure 54 Mean radial velocity profiles at 14 chord lengths downstream of the vortex generator and a tunnel velocity of 40 m/s. The location of the central survey point and the location of the azimuthal velocity peaks have been shown.

Due to the small magnitude of the radial velocity component near the rotational axis (where it must be zero to conserve mass), and the necessity of using the preceding correction, it was not possible to isolate the radial component employing X-wire measurements. In general, the radial flow must be to zero at the center of rotation, but the measured mean centerline velocity never went to zero. There is evidence that the vortex is undergoing a periodic behavior of switching between a radial velocity in the outward direction and a radial velocity in the inward direction. This was indicated by the vertical velocity survey in Figure 50 exhibiting a stable inflow. While other profiles indicated an outflow, decreasing in magnitude, then eventually switching to inflow and a third group indicated an inflow decreasing in magnitude before switching to an outflow. The

behavior observed here is perhaps the gulping phenomena proposed by Bandyopadhya et al (1991). In general, it was not possible to isolate repeatable mean radial velocity profiles.

3.6 Turbulent Kinetic Energy

The inability to measure the mean and fluctuating radial velocity components in the core region of the vortex, along with the dominant nature of the axial velocity prevented this study from measuring accurately the radial-azimuthal component of the Reynolds stress distributions near the vortex core. However, the turbulent kinetic energy at each survey location could be obtained and thus provide insight on the nature of the Reynolds stresses. The turbulent energy was calculated as $Tke = \frac{1}{2}(u'^2 + v'^2 + w'^2)$ and is presented in Figures 55-59.

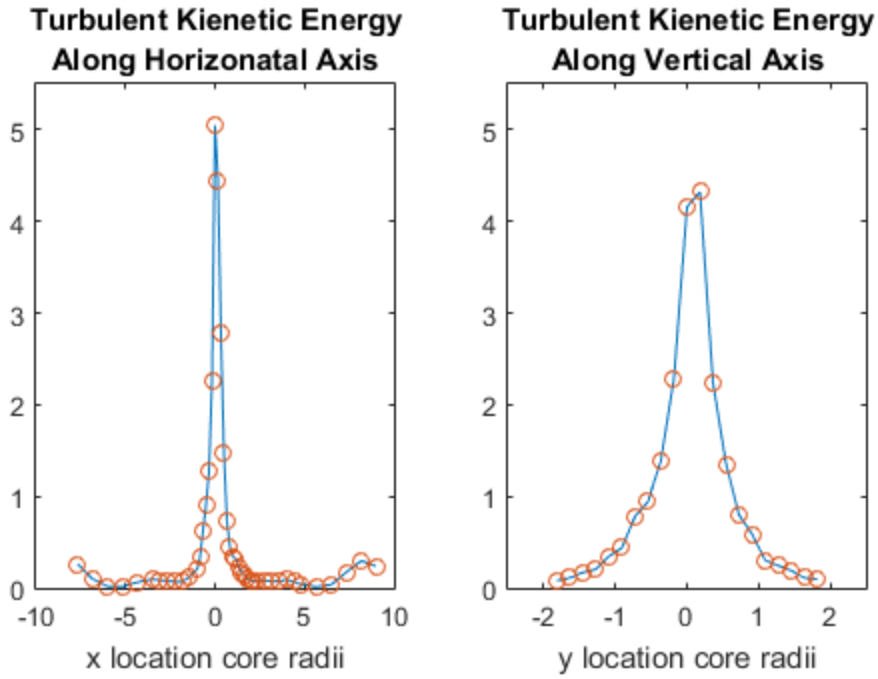

Figure 55 Turbulent Kinetic Energy 7 Chord Lengths downstream of the vortex generator at a tunnel velocity of 30 m/s.

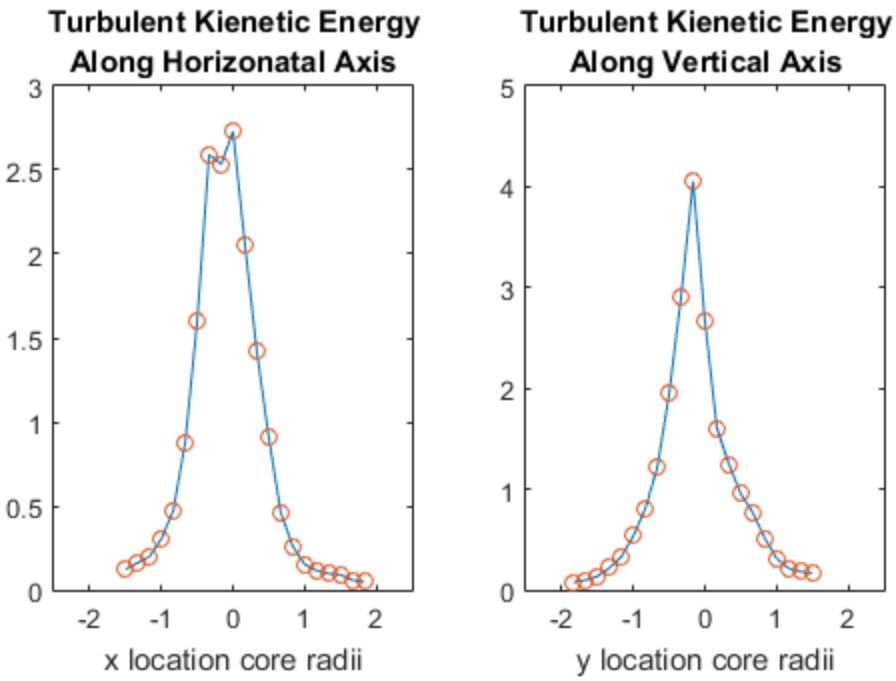

Figure 56 Turbulent Kinetic Energy 10.5 Chord Lengths downstream of the vortex generator at a tunnel velocity of 30 m/s.

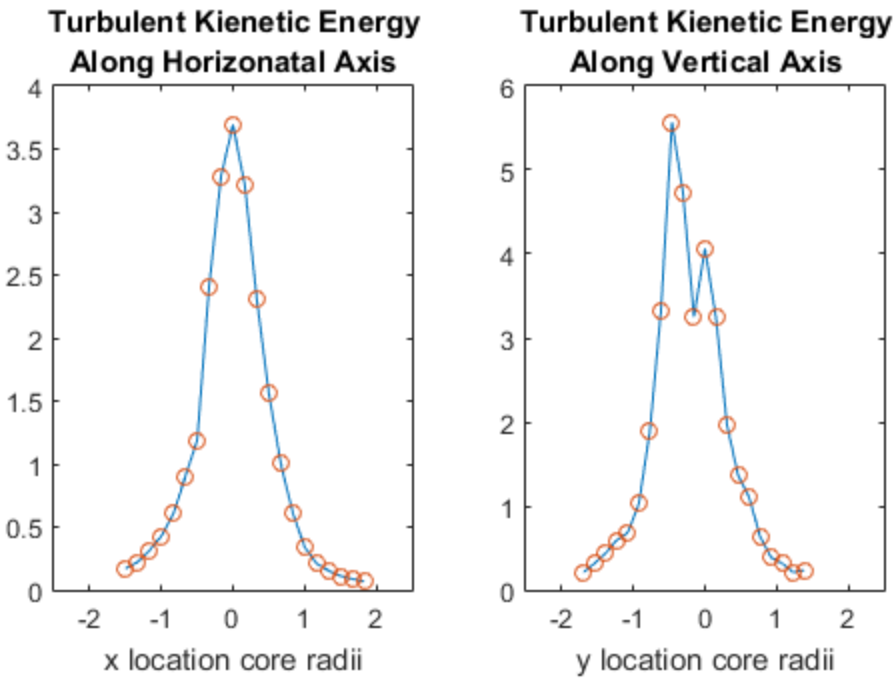

Figure 57 Turbulent Kinetic Energy 14 Chord Lengths downstream of the vortex generator at a tunnel velocity of 30 m/s.

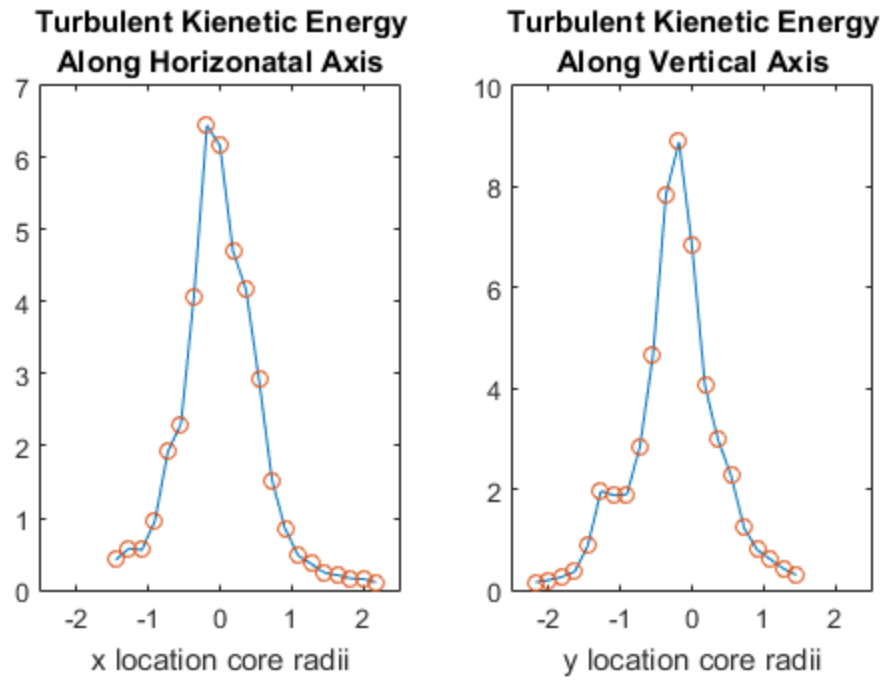

Figure 58 Turbulent Kinetic Energy 10.5 Chord Lengths downstream of the vortex generator at a tunnel velocity of 40 m/s.

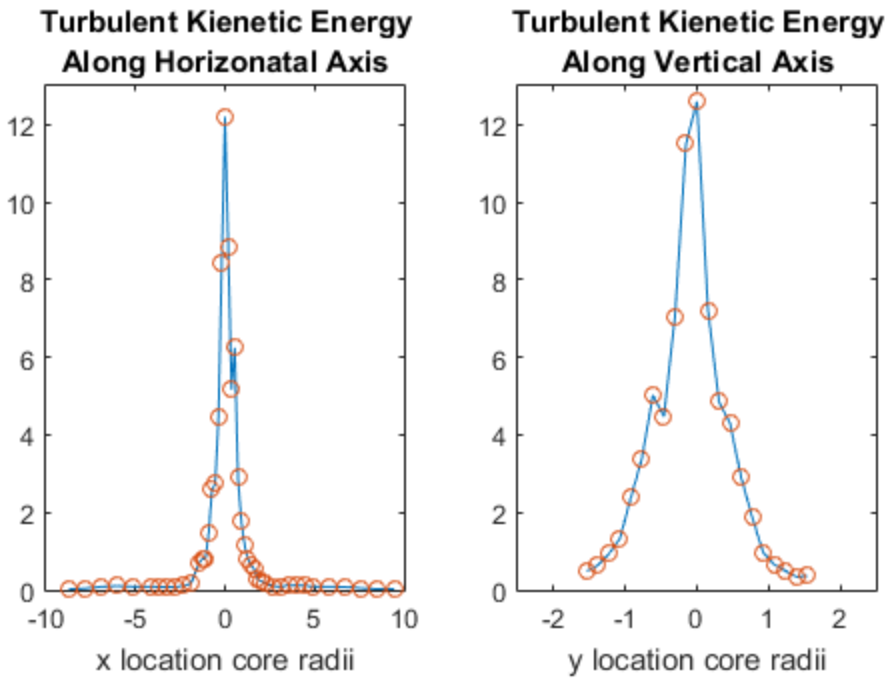

Figure 59 Turbulent Kinetic Energy 14 Chord Lengths downstream of the vortex generator at a tunnel velocity of 40 m/s.

The turbulent kinetic energy was observed to gradually increase as the survey progressed toward the vortex core region. Turbulent kinetic energy increased rapidly within one core diameter of the rotational axis. While the wind tunnel flow itself is weakly-turbulent, the observed turbulent kinetic energy distributions have demonstrated that the core region of the vortex is fully-turbulent.

3.7 Reynolds Stresses

Turbulent Reynolds stresses alter the shear stresses controlling the structure of these axial vortices. Those contributions are gotten from Reynolds averaging of the Navier-Stokes equation, where $\tau_{ij} = -\rho\overline{u_i{}'u_j{}'}$. Unfortunately, X-wire sensors can only measure two-dimensional velocity

fluctuations, and the magnitude of the axial (streamwise) fluctuating velocity component (w') was too large to permit reliable measurements of u'v', along the vertical and horizontal surveys passing nominally through the vortex axis. Only the $\overline{u'w'}$ and $\overline{v'w'}$ Reynolds shear stress components could be measured reliably. Figures 60 through 64 contain plots of the measured Reynolds stresses along each survey axis. Since it was not possible to anticipate the radial and azimuthal coordinate locations corresponding to each mean vortex velocity vector survey location, the Reynolds stress correlations were created in Cartesian coordinates. It should therefore be understood that, in the vertical survey direction, the measured $\overline{u'w'}$ correlations reverse sign when the vortex-based radial fluctuation component crosses the rotational axis. Similarly, the $\overline{v'w'}$ correlations in the horizontal direction, reverse signs after crossing the vortex center. That sign reversal would not occur if the Reynolds stresses were represented employing axial and azimuthal velocity components. Furthermore, the horizontal $\overline{u'w'}$ and vertical $\overline{v'w'}$ survey lines passing through the nominal rotational center of the vortex represent similar vortex surveys. For that reason, the Reynolds stress plots in the horizontal and veritcal survey directions are plotted side-by-side.

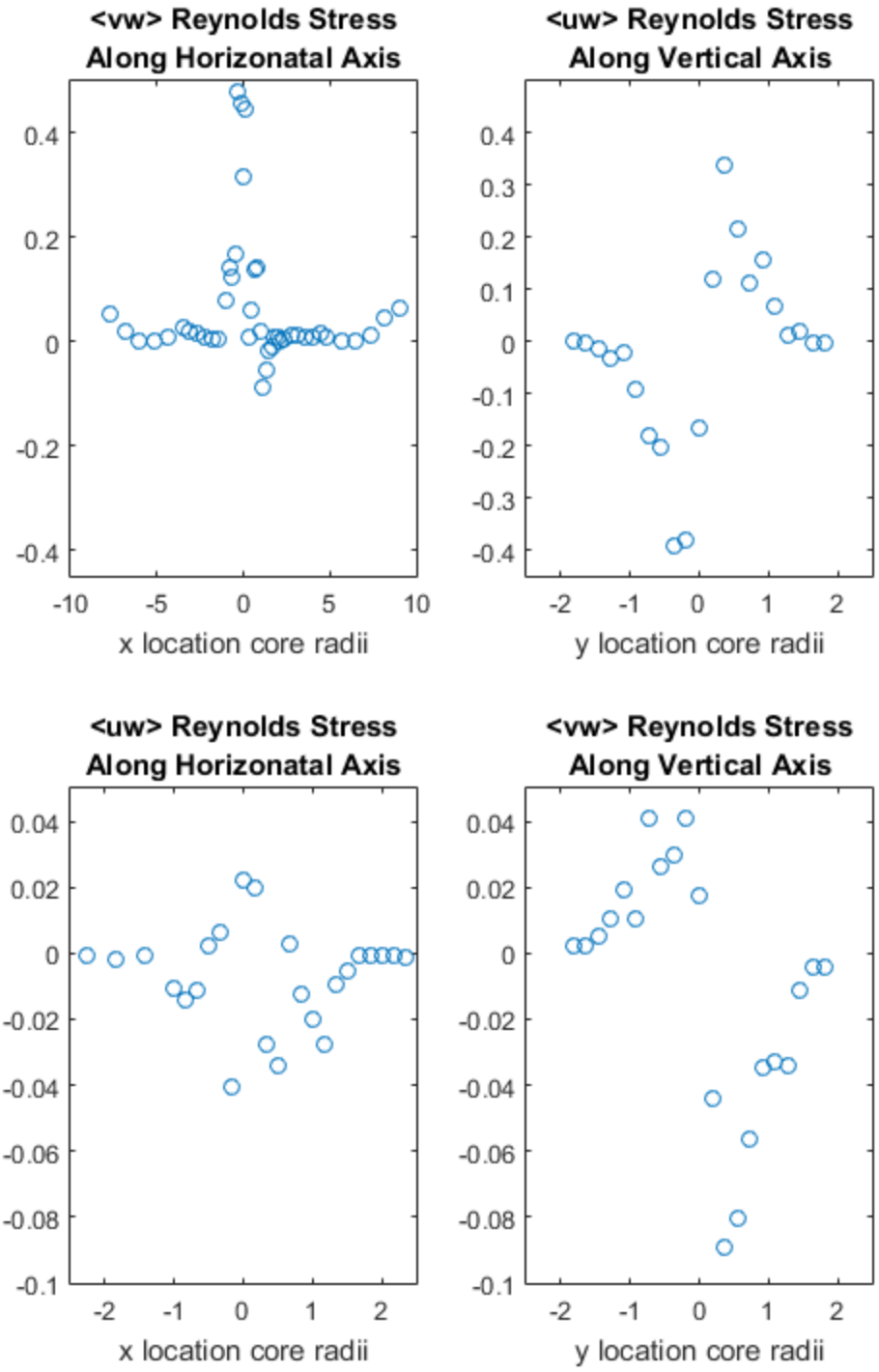

Figure 60 Reynolds stress along each axis at 7 chord lengths from the vortex generator and a wind tunnel speed of 30 m/s.

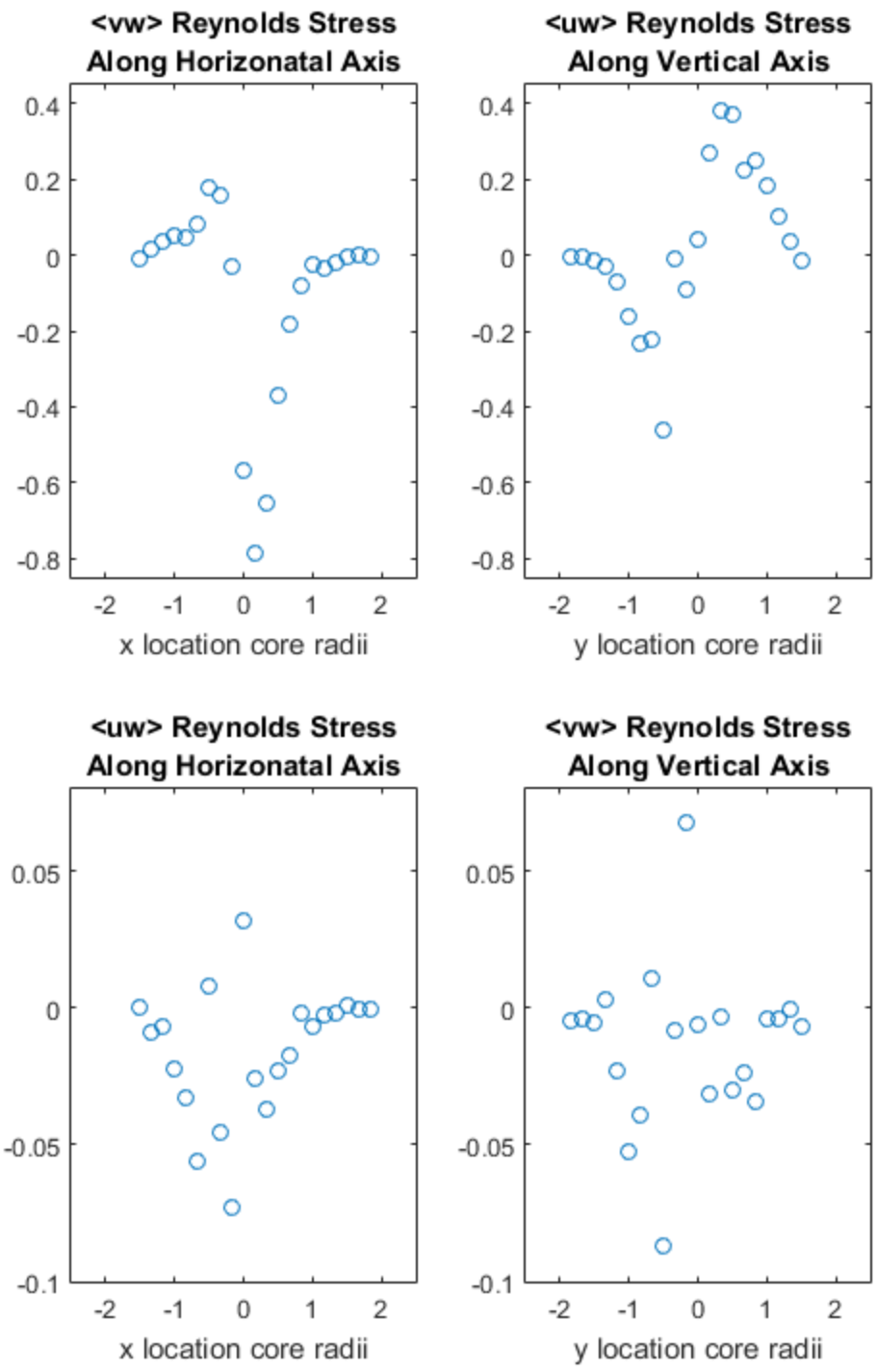

Figure 61 Reynolds stress along each axis at 10.5 chord lengths from the vortex generator and a wind tunnel speed of 30 m/s.

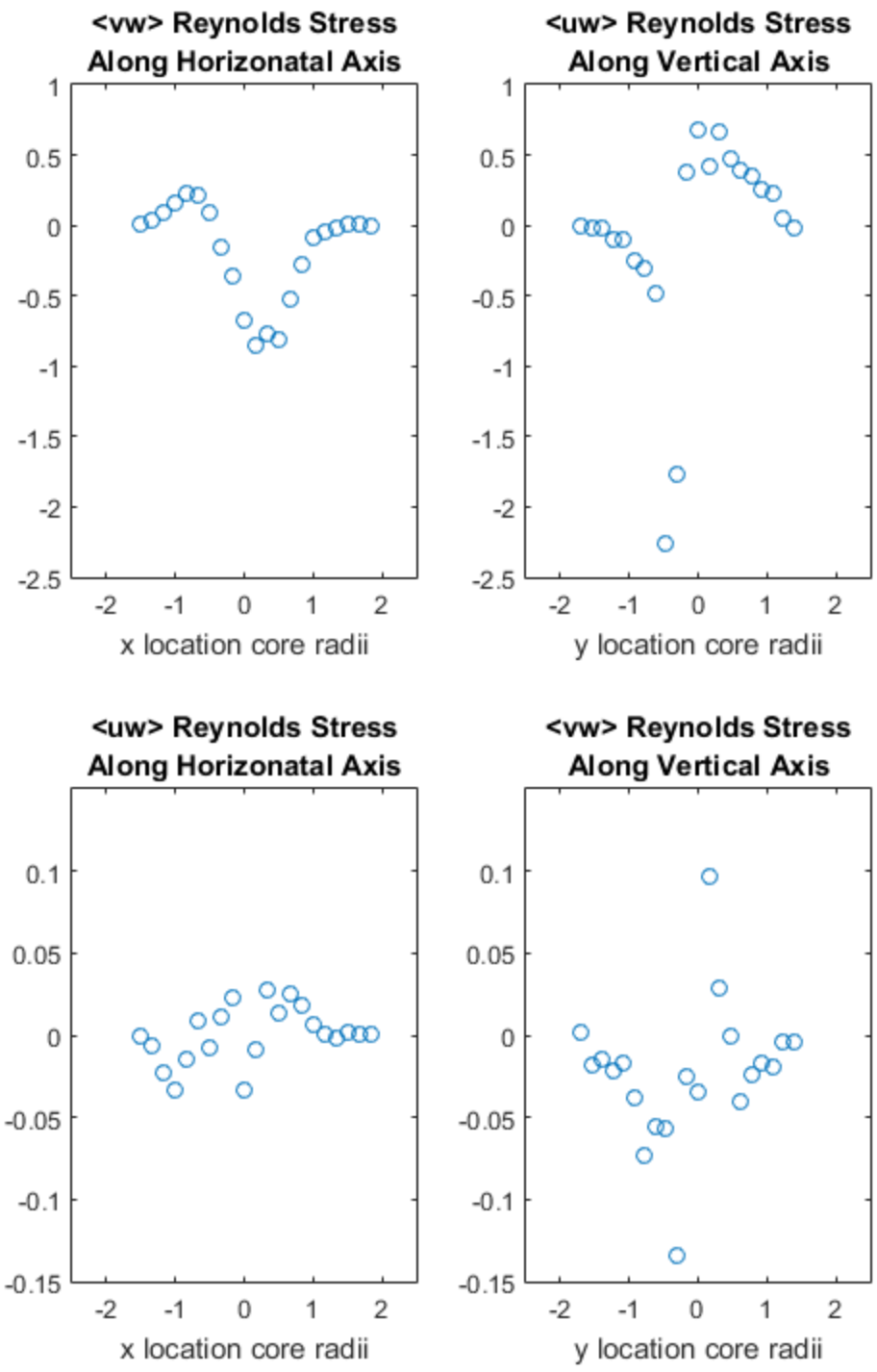

Figure 62 Reynolds stress along each axis at 14 chord lengths from the vortex generator and a wind tunnel speed of 30 m/s.

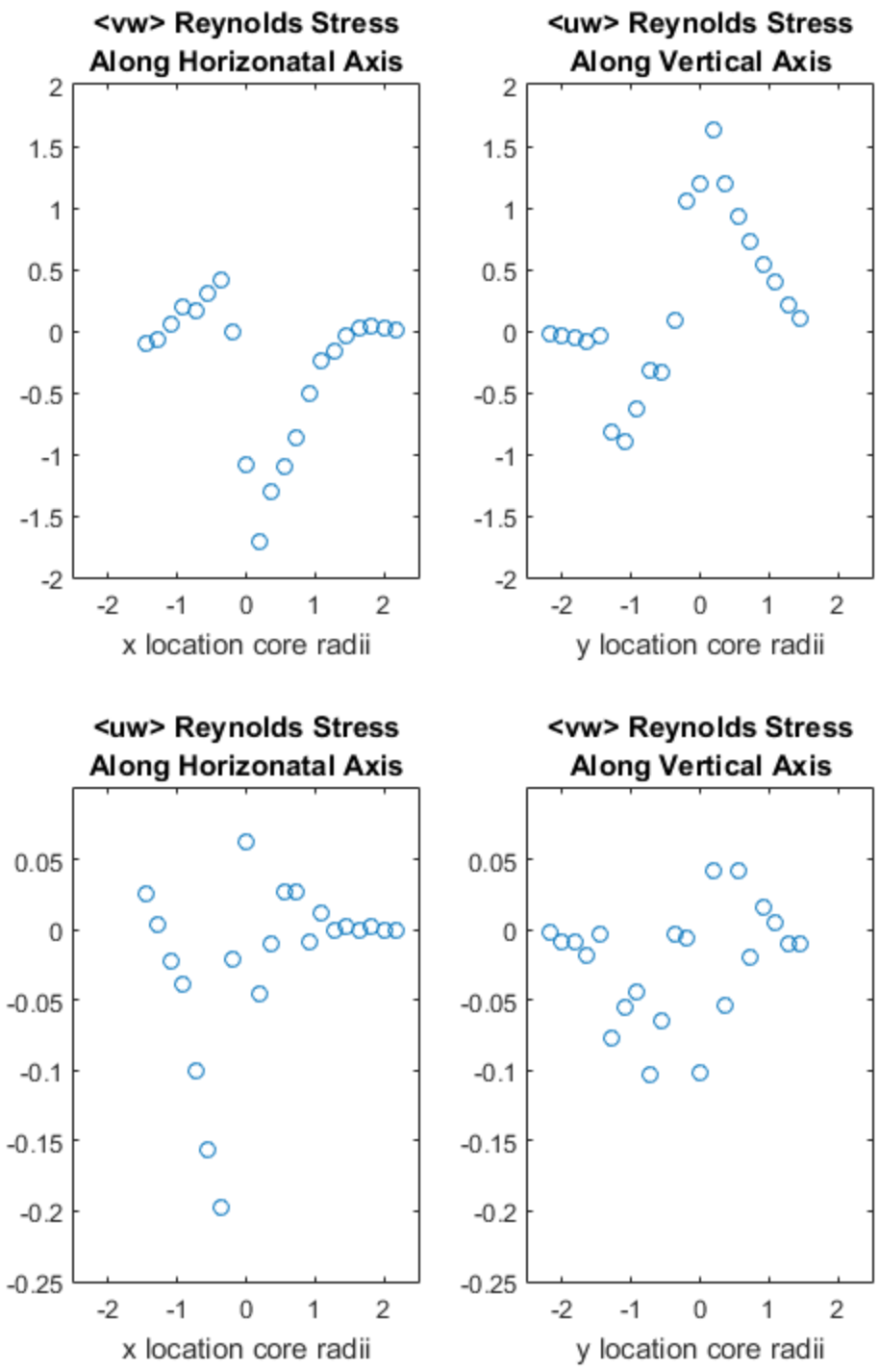

Figure 63 Reynolds stress along each axis at 10.5 chord lengths from the vortex generator and a wind tunnel speed of 40 m/s.

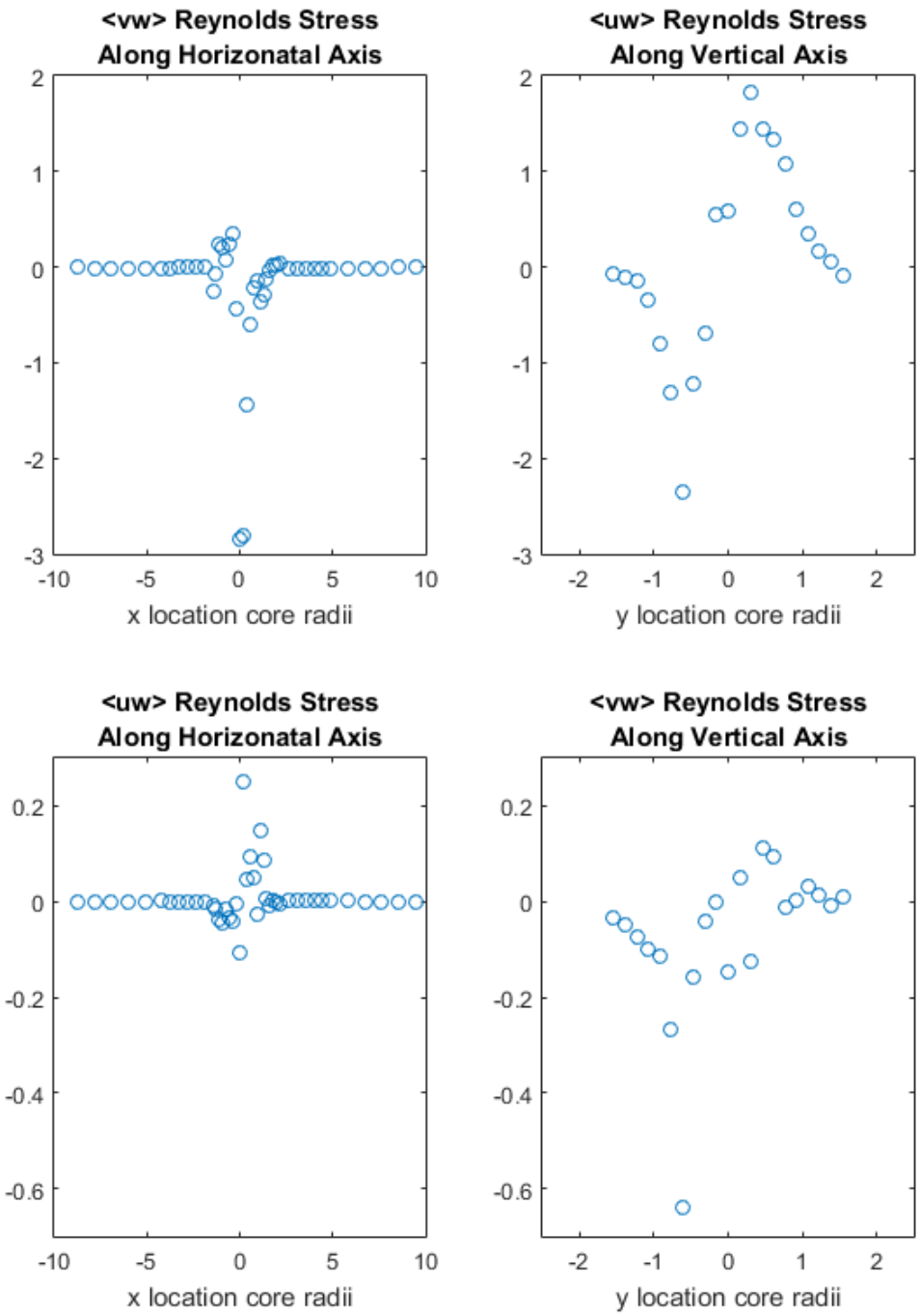

Figure 64 Reynolds stress along each axis at 14 chord lengths from the vortex generator and a wind tunnel speed of 40 m/s.

The data showed that the "axial-radial" Reynolds stress correlation is small at radial locations farther than twice the core radius, and that correlation is approximately zero on the rotational axis, as expected. The "axial-azimuthal" Reynolds stress correlation was observed to again be small farther than twice the core radius and follow a similar pattern of growth inside the core region. The magnitudes of the "axial-azimuthal" Reynolds stress correlation inside the core region were on the order of 10 times larger than "axial-radial" Reynolds stress. While the measured Reynolds stress plots shown here cannot be related directly to "radial-azimuthal" Reynolds stress correlations, the present measurements appear to show: (1) that the Reynolds stresses are not important outside of the core region and (2) that the peak stress levels are observed in the vicinity of the core radius. Since the eddy viscosity model assumes that the "radial-azimuthal" Reynolds stress is proportional to the mean velocity gradient, and the radial gradient of the mean azimuthal velocity is zero at the core radius, the "radial-azimuthal" Reynolds stress should become extremely large in the vicinity of the core radius, and the measured "axial-radial" Reynolds stress correlations appear to be consistent with that type of model.

3.8 Power Spectral Densities

The power spectral densities of the fluctuations of the axial velocity are useful in determining which frequencies of oscillations contain the most energy. These power spectral densities were calculated by taking the absolute value of the fast Fourier transform of the axial velocity fluctuations then multiplying by 1/2T, T being the time over which the sample was taken, to average over the sampling time. Power spectral measurements were each survey location closet to a vortex core radius and the survey point closest to the center of the vortex. The data was sampled at a rate of 100 kHz. Therefore, this allowed for a maximum resolvable frequency of 50 kHz. Through close visual observation of select instantaneous fluctuation outputs it was

determined that there were no identifiable physical oscillations at frequencies above 10 kHz. These plots show the power spectral densities for a range of 0-8kHz.

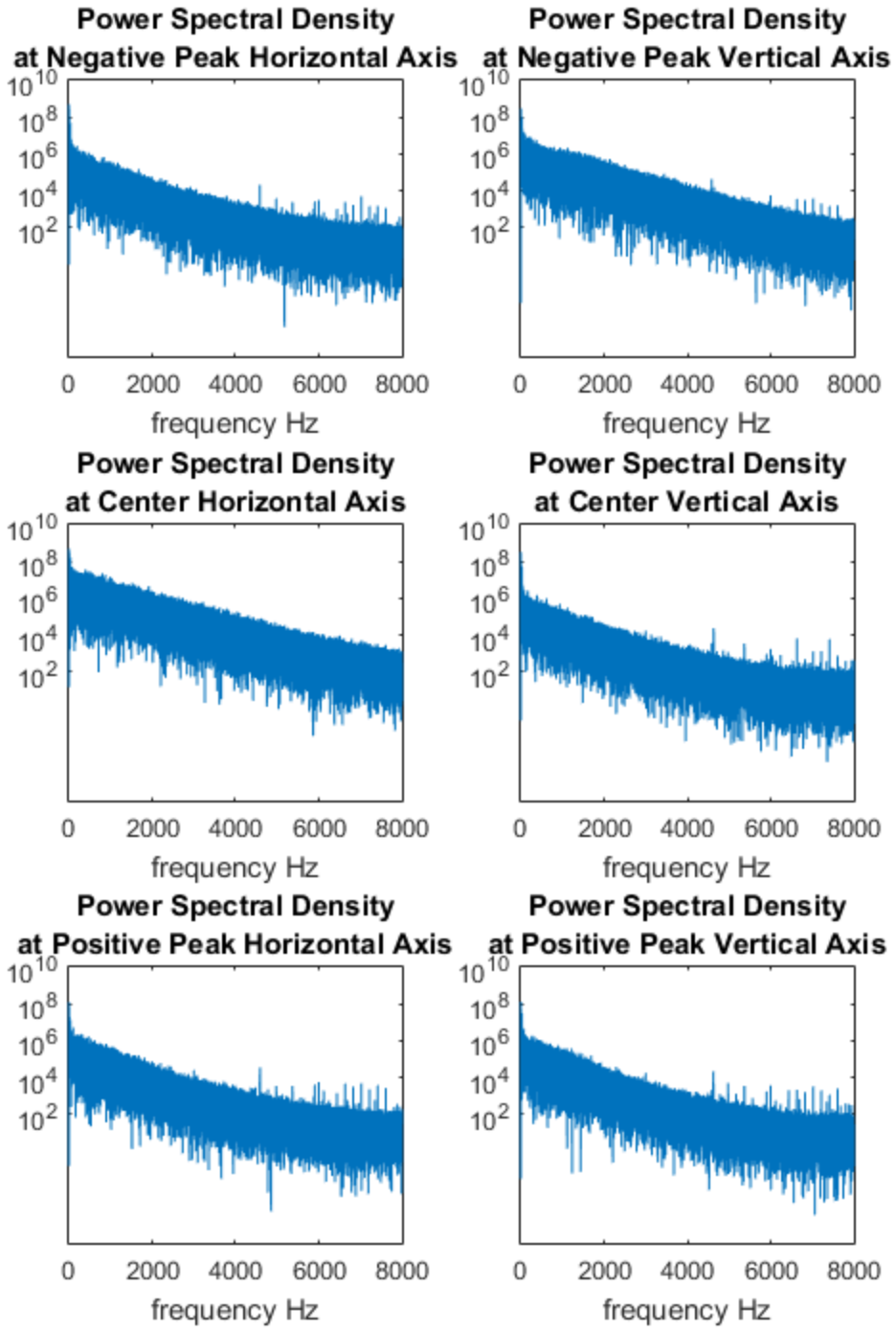

Figure 65 Power Spectral Densities ranging from 0-8kHz at stations in the survey at 7 chord lengths and a velocity 30 m/s.

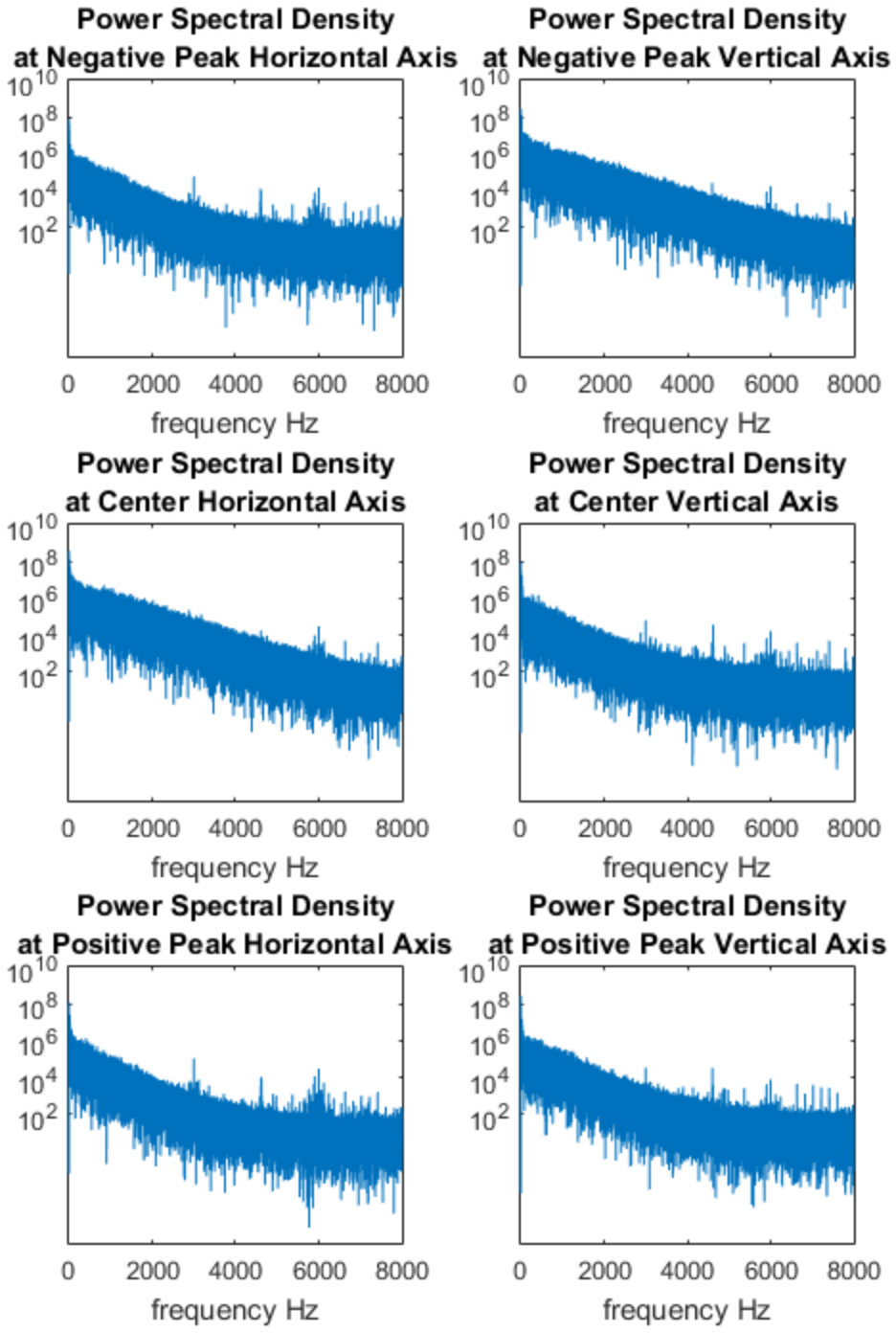

Figure 66 Power Spectral Densities ranging from 0-8kHz at stations in the survey at 10.5 chord lengths and a velocity 30 m/s.

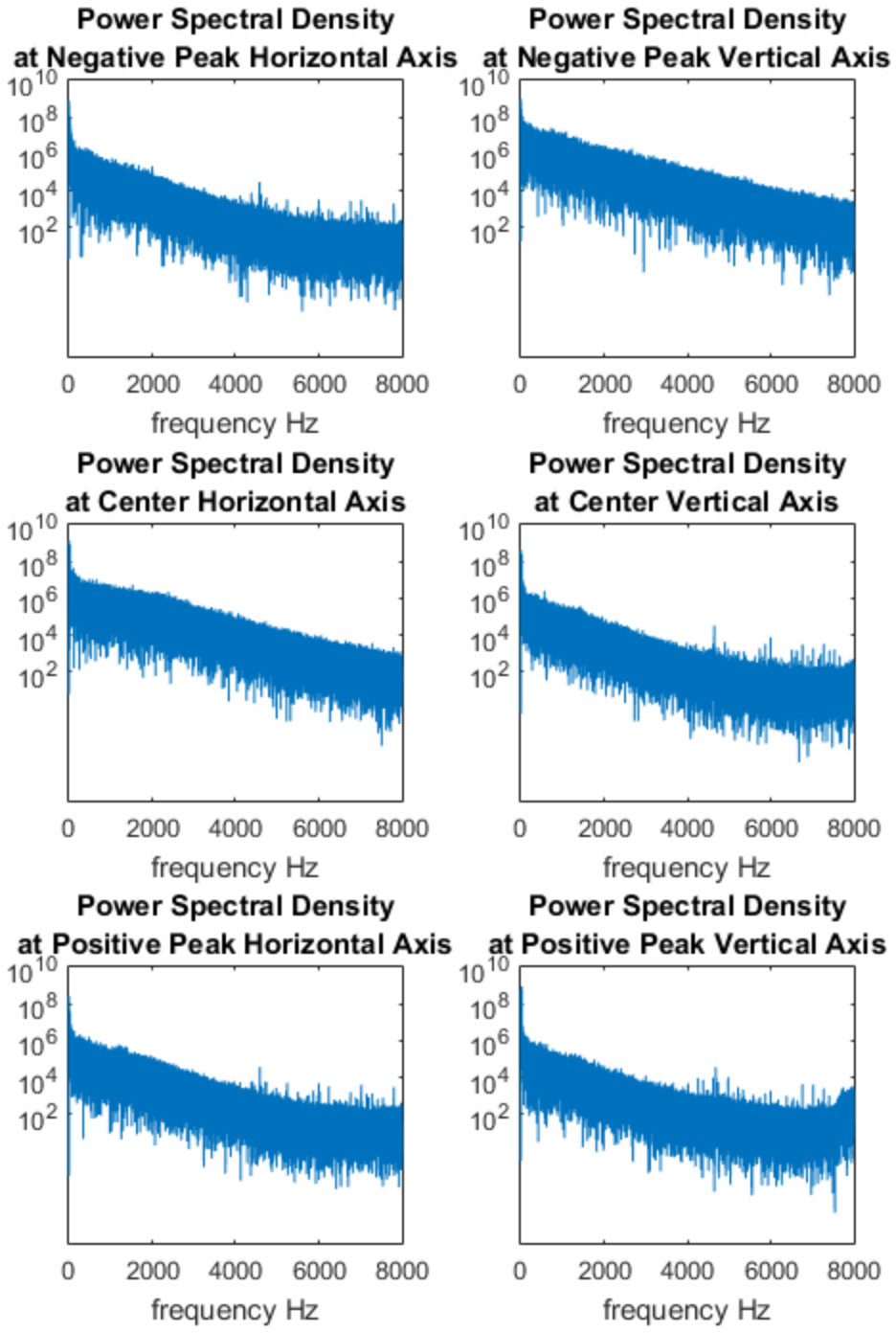

Figure 67 Power Spectral Densities ranging from 0-8 kHz at stations in the survey at 14 chord lengths and a velocity 30 m/s.

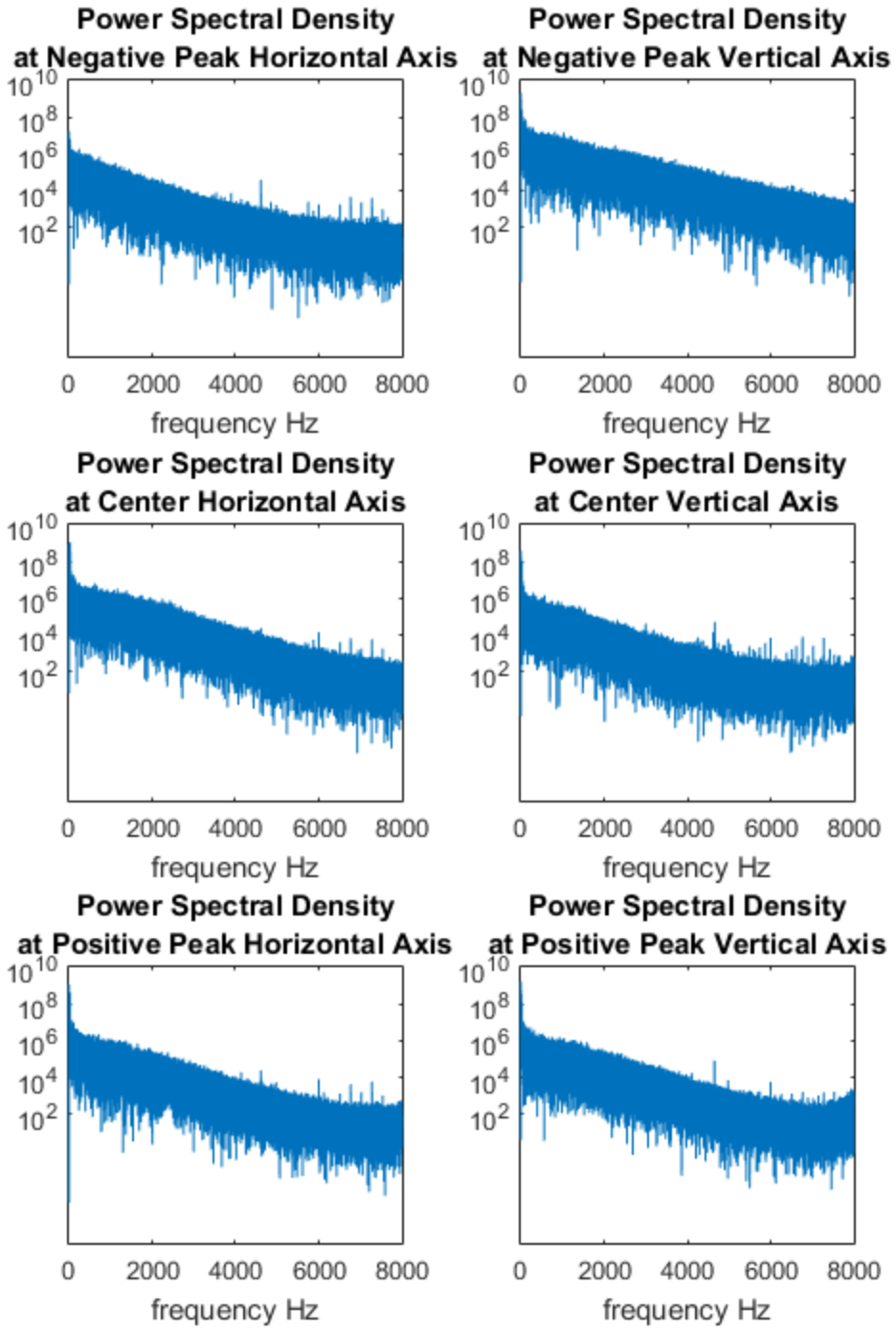

Figure 68 Power Spectral Densities ranging from 0-8 kHz at stations in the survey at 14 chord lengths and a velocity 40 m/s.

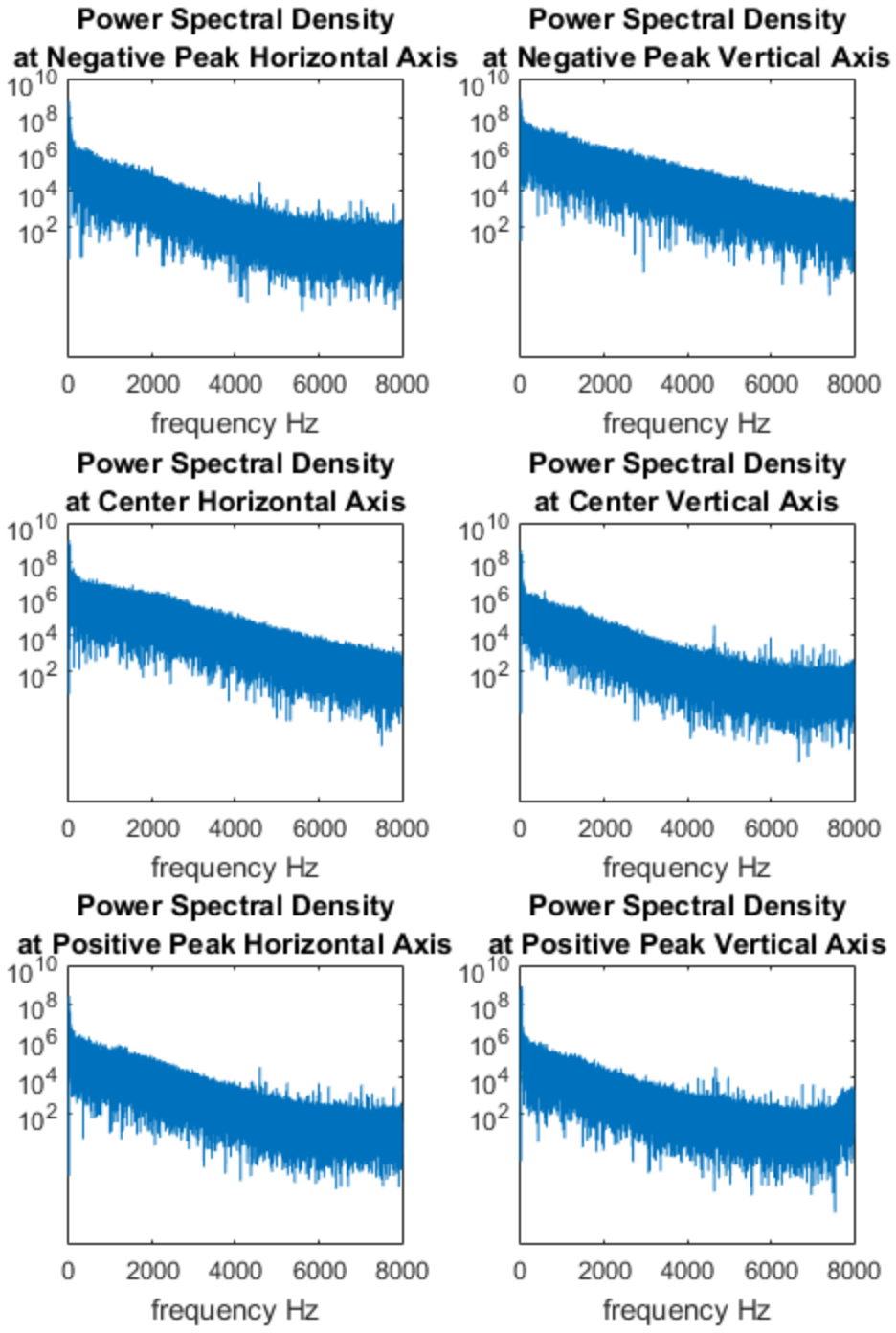

Figure 69 Power Spectral Densities ranging from 0-8 kHz at stations in the survey at 10.5 chord lengths and a velocity 40 m/s.

From 0 to 1000 Hz, the energy contained in the power spectral densities gradually decreased. At 1000 Hz the rate at which the energy contained in the flow dropped off increase. Between 3000 and 8000 Hz the signal decayed to the point it was not discernable from noise. This confirmed the visual inspection of the instantaneous data that indicated there were no flow-based fluctuations occurring at frequencies higher than 10 kHz.

3.9 Azimuthal Velocity Comparisons

One of the primary goals of this research was to investigate possible effects of non-equilibrium pressure on the structure of an axial vortex. It was therefore useful to compare our experimental azimuthal velocity profiles with the theoretical profiles predicted from the work of Ash, Zardadkhan and Zuckerwar (2011). The theoretical azimuthal profile was

$$v_\theta(r) = 2v_{\theta,max}\frac{\frac{r}{r_{core}}}{\left(\frac{r}{r_{core}}\right)^2 + 1} \tag{45}$$

In order to generate an appropriate theoretical profile to compare with the experimental measurements, the peak azimuthal velocity and its associated radial distance from the rotational axis were employed as $v_{\theta,\max}$ and r_{core} respectively. Since the pressure relaxation coefficient, η_p, and the kinematic viscosity are dependent on both humidity and temperature, and those parameter changed from point to point during the velocity surveys. It was necessary to adjust $v_{\theta,\max}$ and r_{core} to compensate for those variations. This was done employing the following equations from Ash, Zardakhan and Zuckerwar (2011), relating the maximum azimuthal velocity and corresponding core radius to vortex circulation and ultimately to the turbulent eddy viscosity and the pressure relaxation coefficient

$$v_{\theta,max} = \frac{\Gamma_\infty}{4\pi r} = \sqrt{2\frac{v_{turb}}{\eta_p}} \tag{46}$$

$$r_{core} = \frac{Re_\Gamma}{2}\sqrt{\frac{v_{turb}\eta_p}{2}} \tag{47}$$

$$\frac{v_{turbinitial}}{v_{intial}} = constant = \frac{v_{turbn}}{v_n} \tag{48}$$

$$\mathrm{Re}_\Gamma = \frac{\Gamma}{2\pi\nu} \tag{49}$$

Equation 46 was employed assuming that the vortex circulation produced by the bi-wing generator, and the turbulent eddy viscosity, were (unknown) constants for a given wind tunnel test condition throughout a survey. Equation 46 could then be employed, along with the pressure relaxation coefficient at the measured temperature and relative humidity associated with each survey point to determine a corrected maximum azimuthal velocity for use in Equation 45. Similarly, Equation 47 was employed, assuming that the circulation-based Reynolds number was constant, to determine the corrected core radius for each survey point. In order to better demonstrate the effects of pressure relaxation on the flow Figures 70 through 74 present two theoretical profiles compared with the data. The first profile treated both eddy viscosity and

pressure relaxation as constants. The second profile adjusted for a variable eddy viscosity but held pressure relaxation constant.

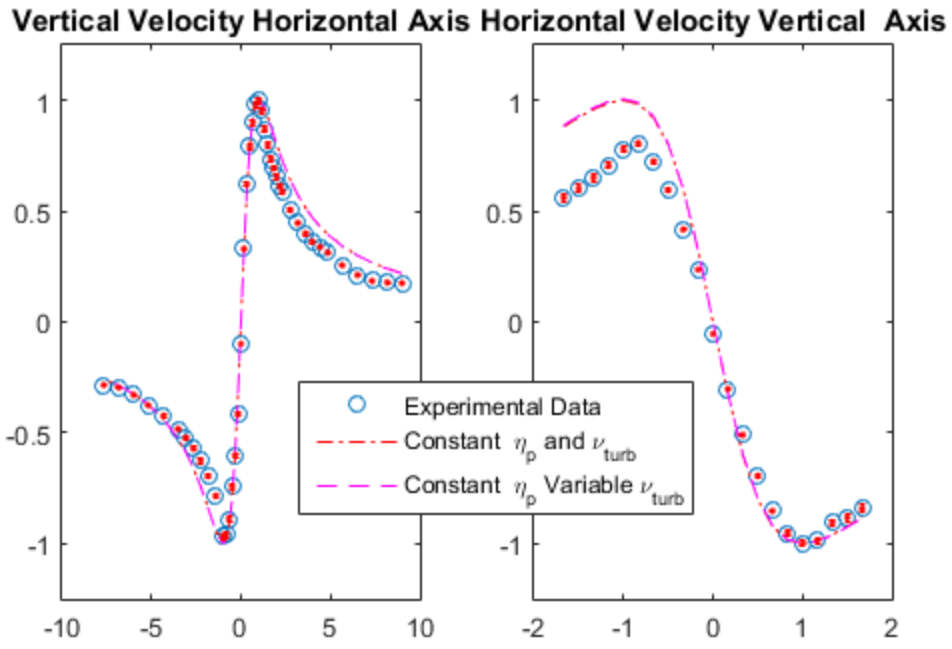

Figure 70 Comparison of the experimentally captured azimuthal velocity profiles to the profiles generated from the non-equilibrium pressure theory at 7 chord lengths downstream of the vortex generator and a tunnel speed of 30 m/s.

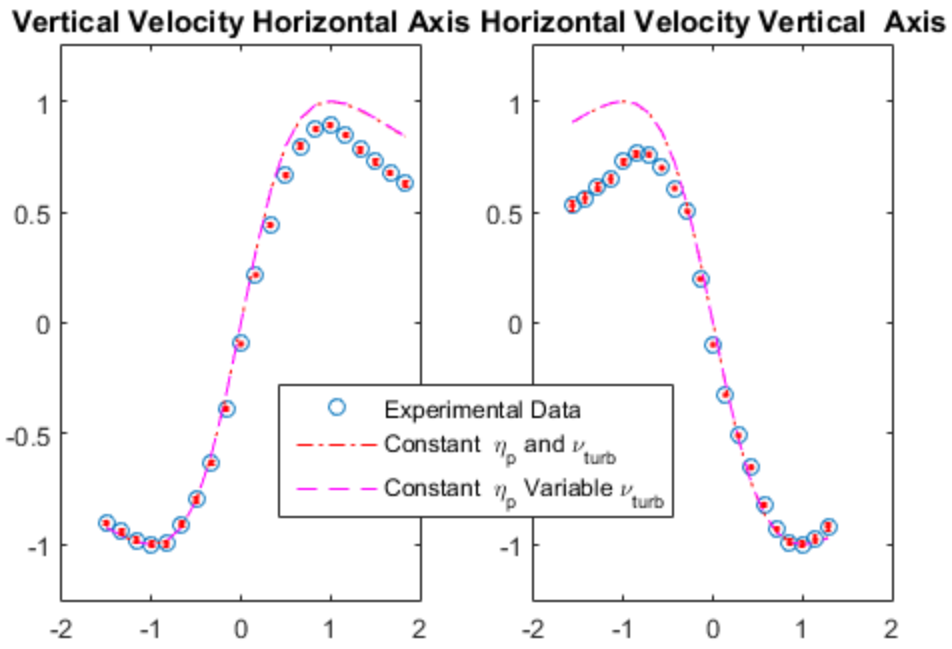

Figure 71 Comparison of the experimentally captured azimuthal velocity profiles to the profiles generated from the non-equilibrium pressure theory at 10.5 chord lengths downstream of the vortex generator and a tunnel speed of 30 m/s.

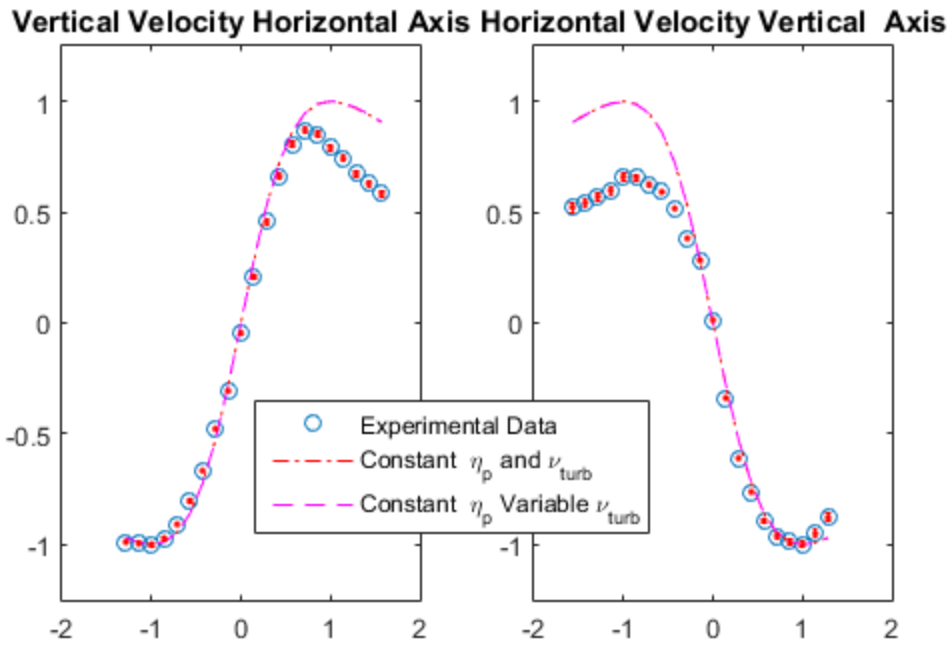

Figure 72 Comparison of the experimentally captured azimuthal velocity profiles to the profiles generated from the non-equilibrium pressure theory at 14 chord lengths downstream of the vortex generator and a tunnel speed of 30 m/s.

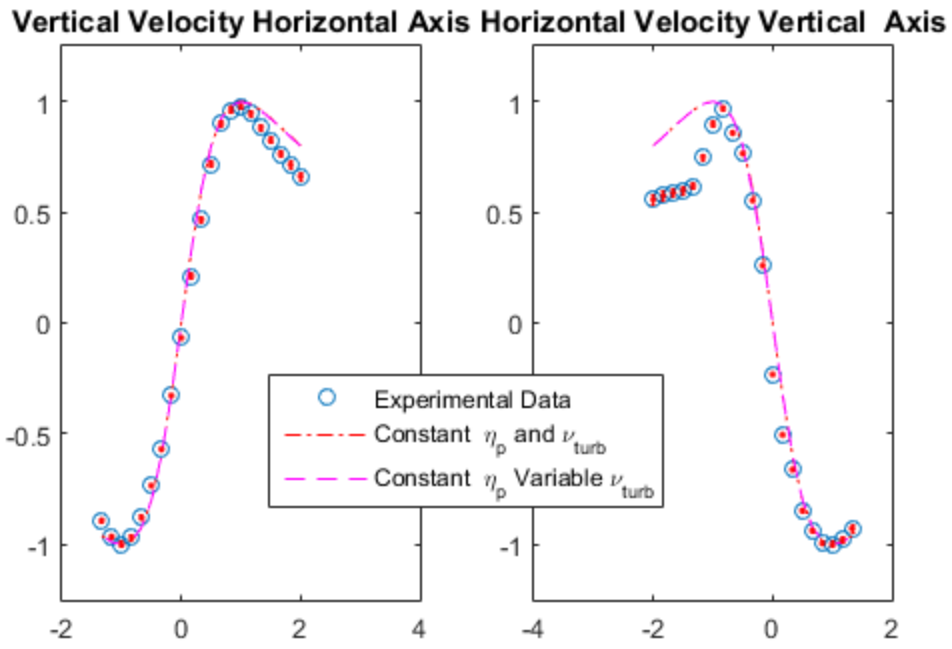

Figure 73 Comparison of the experimentally captured azimuthal velocity profiles to the profiles generated from the non-equilibrium pressure theory at 10.5 chord lengths downstream of the vortex generator and a tunnel speed of 40 m/s.

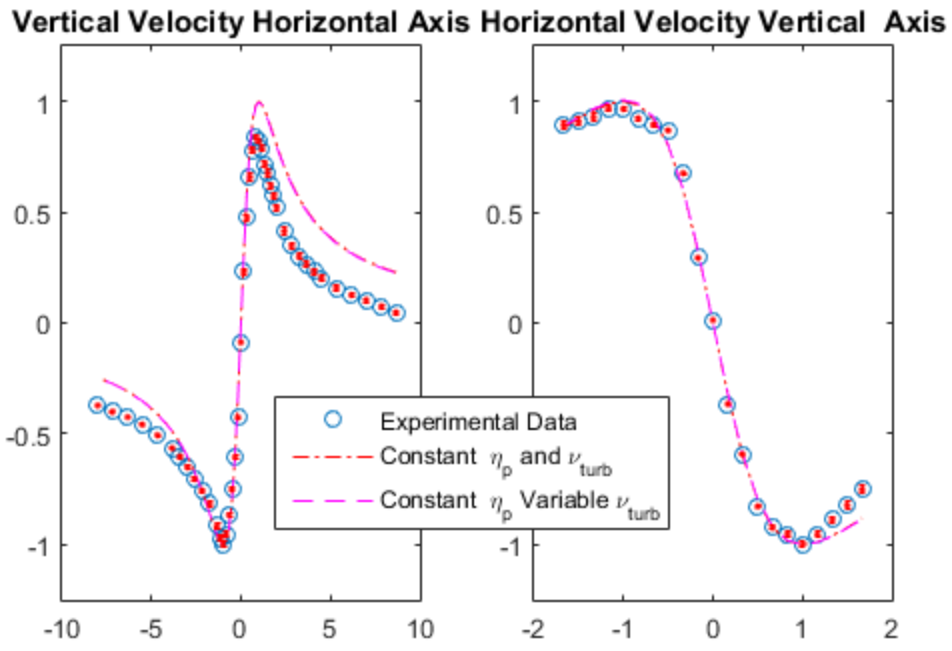

Figure 74 Comparison of the experimentally captured azimuthal velocity profiles to the profiles generated from the non-equilibrium pressure theory at 14 chord lengths downstream of the vortex generator and a tunnel speed of 40 m/s.

The theoretical profiles presented above tended to correlate well in the vicinity of the maximum azimuthal velocity ($v_{\theta,max}$), and inside the core region. However in most cases when the opposite velocity peak varied in magnitude from the one used as $v_{\theta,max}$, the theoretical profiles tended to overestimate the peak velocity and velocities outside of the core on that side of the vortex. This variance grew as the discrepancy between the peak velocity magnitudes grew. On the side of the vortex where $v_{\theta,max}$ occurred the theoretical profile tended to predict the velocities around the core boundary while underestimating the velocities far from the boundary. The theory was developed assuming an infinite flow field, and this contributed to the difference observed here because the vortex interacts with the walls of the tunnel in the far field.

In order to better understand the effects of the tunnel walls it was useful to look at their effect on a potential flow. The potential flow model can provide insight on how the nearness of the tunnel wall influences the maximum strain rate in the vicinity of the observed vortex core. To account for the walls of the wind tunnel it was necessary to construct a stream function via superposition. The first function used was the stream function for a potential vortex in an infinite flow field

$$\psi = \frac{\Gamma_0}{2\pi}\left[\ln\left(\sqrt{x^2+y^2}\right)\right] \tag{50}$$

Superposition was then used to combine this with vortices rotating in the opposite direction mirrored on opposite sides of the vortex at points on each axis such that the walls of the tunnel would be at the midpoint between the primary vortex and the mirrored vortices.

$$\begin{aligned}\psi = {} & \frac{\Gamma_0}{2\pi}\left[\ln\left(\sqrt{x^2+y^2}\right)\right] - \frac{\Gamma_0}{2\pi}\left[\ln\left(\sqrt{(x-4)^2+y^2}\right)\right] \\ & - \frac{\Gamma_0}{2\pi}\left[\ln\left(\sqrt{(x+4)^2+y^2}\right)\right] - \frac{\Gamma_0}{2\pi}\left[\ln\left(\sqrt{x^2+(y-3)^2}\right)\right] \\ & - \frac{\Gamma_0}{2\pi}\left[\ln\left(\sqrt{x^2+(y+3)^2}\right)\right]\end{aligned} \tag{51}$$

Simplifying gives

$$\psi = \frac{\Gamma_0}{2\pi}\left[\ln\left(\sqrt{\frac{x^2+y^2}{((x-4)^2+y^2)((x+4)^2+y^2)(x^2+(y-3)^2)(x^2+(y+3)^2)}}\right.\right. \tag{52}$$

We can then use the following partial derivative to find each component of velocity

$$u = \frac{\partial\psi}{\partial y} = \frac{\Gamma_0}{2\pi}\left(\frac{y}{x^2+y^2} - \frac{y}{(x+4)^2+y^2} + \frac{y}{(x-4)^2+y^2} + \frac{y+3}{x^2+(y+3)^2} + \frac{y-3}{x^2+(y-3)^2}\right) \tag{53}$$

$$v = -\frac{\partial \psi}{\partial x} = \frac{\Gamma_0}{2\pi}\left(-\frac{x}{x^2+y^2} + \frac{x+4}{(x+4)^2+y^2} + \frac{x-4}{(x-4)^2+y^2} + \frac{x}{x^2+(y+3)^2} + \frac{x}{x^2+(y-3)^2}\right) \tag{54}$$

We know the strain rate is

$$\dot{\varepsilon_{xy}} = \frac{1}{2}\left[\frac{\partial u}{\partial y} + \frac{\partial v}{\partial x}\right] \tag{55}$$

So

$$\frac{\partial u}{\partial y} = \frac{\Gamma_0}{2\pi}\left(\frac{y}{x^2+y^2} - \frac{y}{(x+4)^2+y^2} - \frac{y}{(x-4)^2+y^2} - \frac{y+3}{x^2+(y+3)^2} - \frac{y-3}{x^2+(y-3)^2}\right)$$

$$= \frac{x^2-y^2}{(x^2+y^2)^2} - \frac{(x+4)^2-y^2}{((x+4)^2+y^2)^2} - \frac{(x-4)^2-y^2}{((x-4)^2+y^2)^2} - \frac{x^2-(y+3)^2}{(x^2+(y+3)^2)^2} - \frac{x^2-(y-3)^2}{(x^2+(y-3)^2)^2}$$

$$\frac{\partial v}{\partial x} = \frac{\Gamma_0}{2\pi}\left(-\frac{x}{x^2+y^2} + \frac{x+4}{(x+4)^2+y^2} + \frac{x-4}{(x-4)^2+y^2} + \frac{x}{x^2+(y+3)^2} + \frac{x}{x^2+(y-3)^2}\right)$$

$$= \frac{x^2-y^2}{(x^2+y^2)^2} - \frac{(x+4)^2-y^2}{((x+4)^2+y^2)^2} - \frac{(x-4)^2-y^2}{((x-4)^2+y^2)^2} - \frac{x^2-(y+3)^2}{(x^2+(y+3)^2)^2} - \frac{x^2-(y-3)^2}{(x^2+(y-3)^2)^2}$$

$$\dot{\varepsilon_{xy}} = \frac{1}{2}\left[\frac{\partial u}{\partial y} + \frac{\partial v}{\partial x}\right] \tag{56}$$

$$= \frac{\Gamma_0}{2\pi}\frac{1}{2} * 2\left[\frac{x^2 - y^2}{(x^2 + y^2)^2} - \frac{(x+4)^2 - y^2}{((x+4)^2 + y^2)^2} - \frac{(x-4)^2 - y^2}{((x-4)^2 + y^2)^2} - \frac{x^2 - (y+3)^2}{(x^2 + (y+3)^2)^2} - \frac{x^2 - (y-3)^2}{(x^2 + (y-3)^2)^2}\right]$$

$$= \frac{\Gamma_0}{2\pi}\left(\frac{x^2 - y^2}{(x^2 + y^2)^2} - \frac{(x+4)^2 - y^2}{((x+4)^2 + y^2)^2} - \frac{(x-4)^2 - y^2}{((x-4)^2 + y^2)^2} - \frac{x^2 - (y+3)^2}{(x^2 + (y+3)^2)^2} - \frac{x^2 - (y-3)^2}{(x^2 + (y-3)^2)^2}\right)$$

Using the circulation determined from the maximum observed velocity, the strain rate was evaluated along the x and y axis to obtain a theoretical strain rate profile which was compared to the experimentally captured profiles.

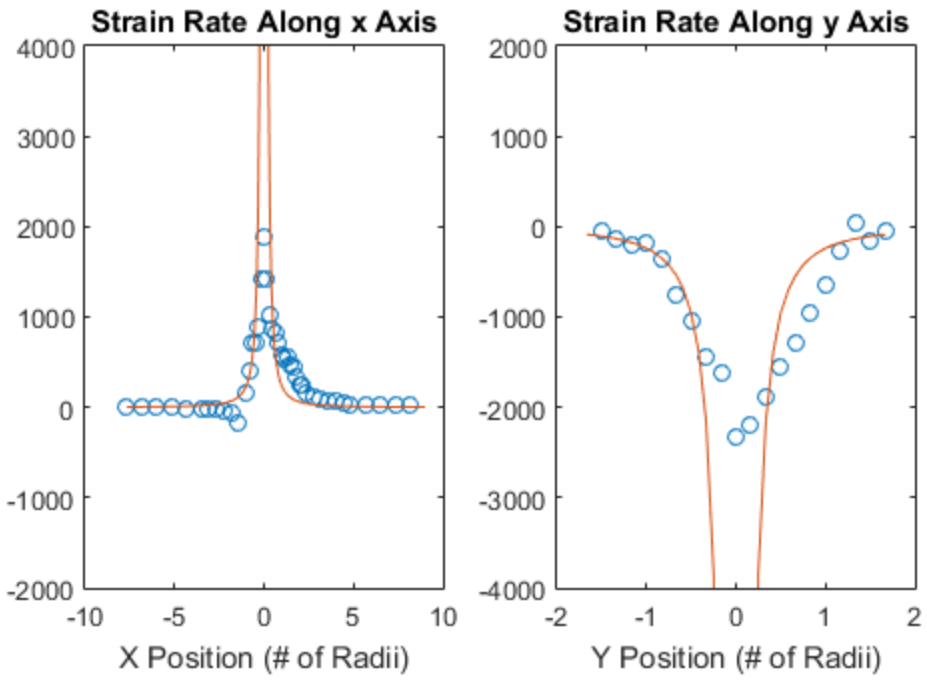

Figure 75 Strain Rate Experimental plotted against potential flow theoretical at 7 chord lengths downstream of the vortex generator and a tunnel velocity of 30 m/s.

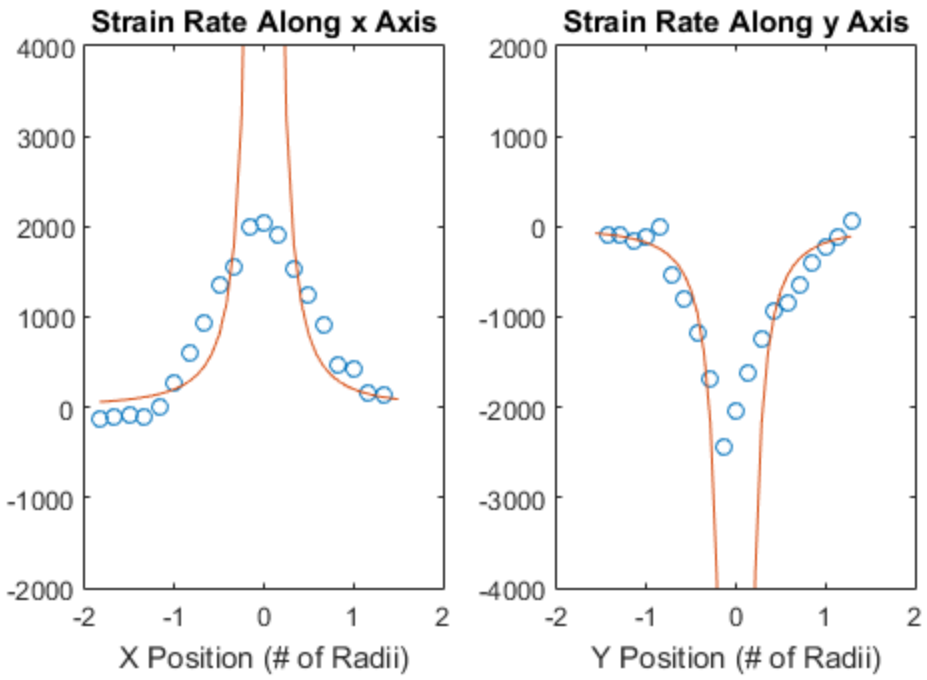

Figure 76 Strain Rate Experimental plotted against potential flow theoretical at 10.5 chord lengths downstream of the vortex generator and a tunnel velocity of 30 m/s.

Survey	Horizontal Strain Rate at 1 radii	Vertical Strain rate at 1 radii
7 CL 30 m/s	234.4	-239.9
10.5 CL 30 m/s	200.9	-177.9
14 CL 30 m/s	226.4	-183.4
10.5 CL 40 m/s	287.2	-250.6
14 CL 40 m/s	274.1	-231

Table 21 strain rate at 1 core radii along each axis for all surveys.

From this analysis, it was clear the sign of the strain rate was related to the direction of the vortex spin. Outside the core, the potential vortex model agrees with the experimental measurements. A clear link can be observed here between the symmetry of the tunnel walls and the symmetry of the potential vortex. From the experimental results it was known the most symmetrical observed vortex was located seven chord lengths downstream from the vortex generator at a tunnel velocity of 30 m/s. The theoretical strain rate at the core radius along both axes closely match. In the less symmetrical vortices the differences between the theoretical strain rates at the core radius increased.

The second set of profiles compared the theoretical velocity profile, employing a constant pressure relaxation coefficient and variable eddy viscosity, to the experimental data; then compared the theoretical profiles taking into account variable pressure relaxation coefficient, based on changes in wind tunnel temperature and relative humidity, and variable eddy viscosity.

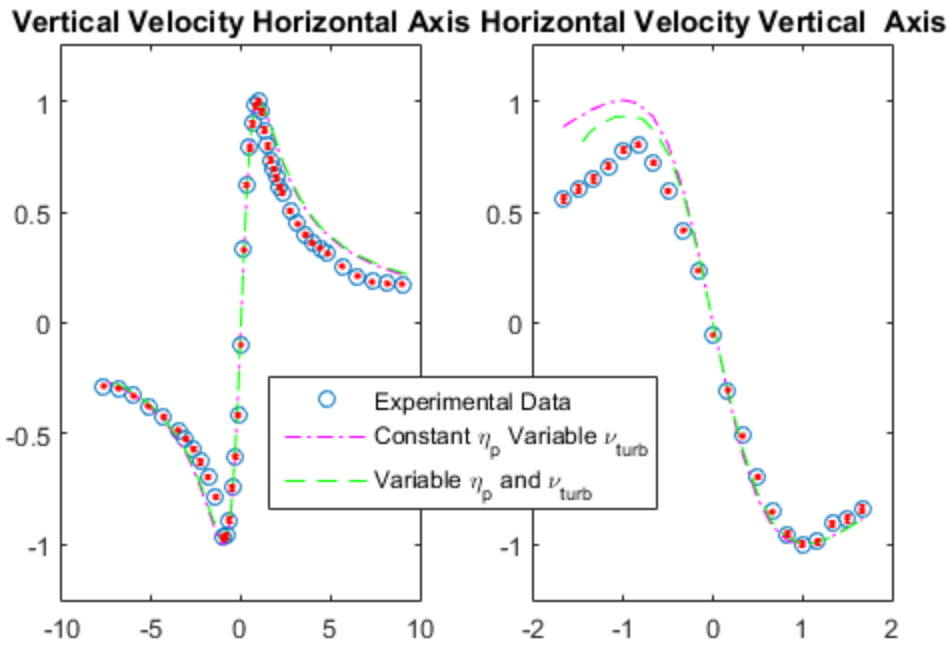

Figure 77 Comparison of the experimentally captured azimuthal velocity profiles to the profiles generated from the non-equilibrium pressure theory at 7 chord lengths downstream of the vortex generator and a tunnel speed of 30 m/s with uncertainty bars.

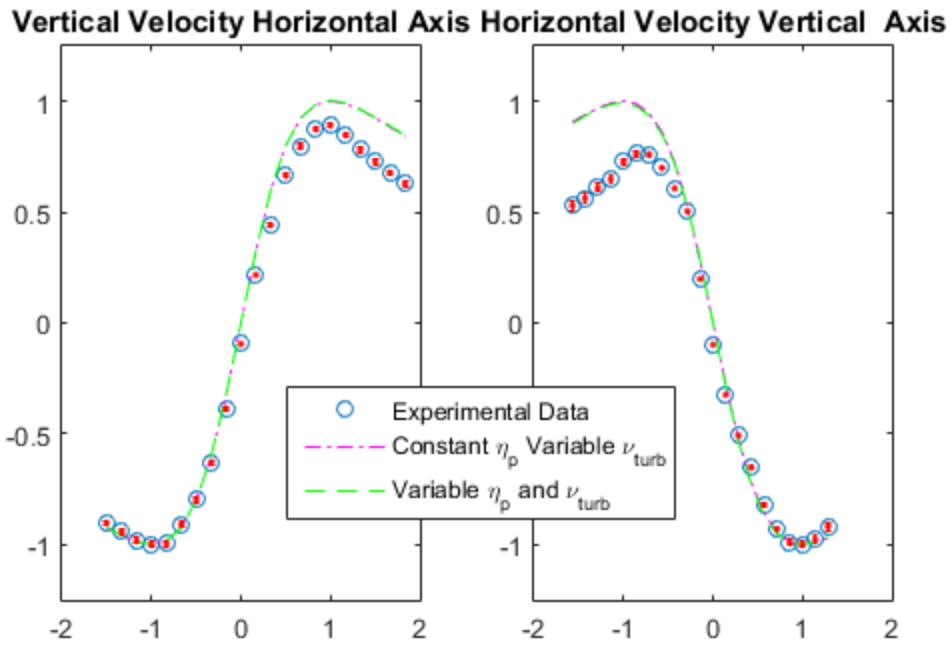

Figure 78 Comparison of the experimentally captured azimuthal velocity profiles to the profiles generated from the non-equilibrium pressure theory at 10.5 chord lengths downstream of the vortex generator and a tunnel speed of 30 m/s with uncertainty bars.

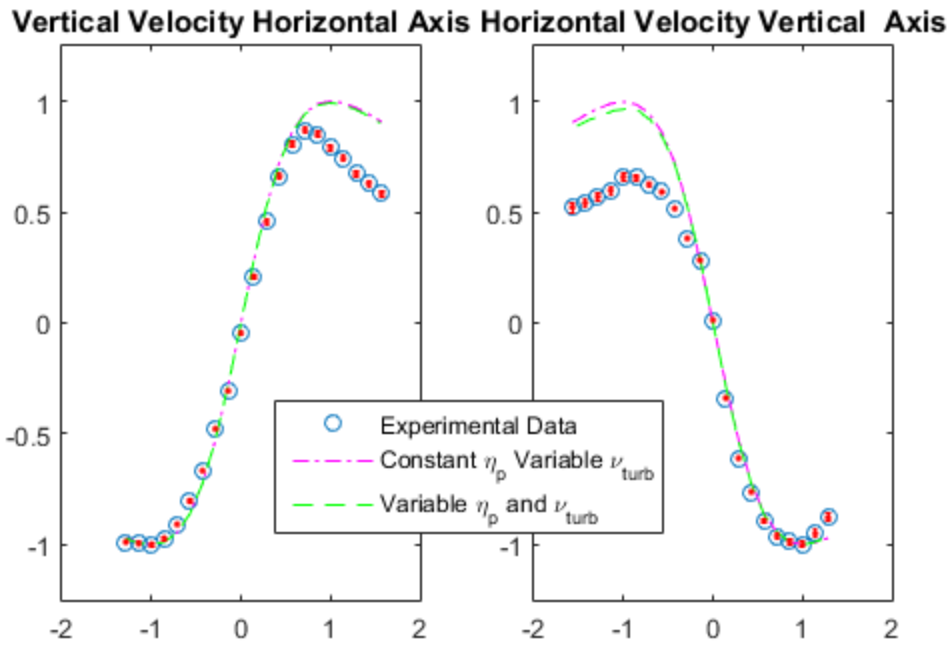

Figure 79 Comparison of the experimentally captured azimuthal velocity profiles to the profiles generated from the non-equilibrium pressure theory at 14 chord lengths downstream of the vortex generator and a tunnel speed of 30 m/s with uncertainty bars.

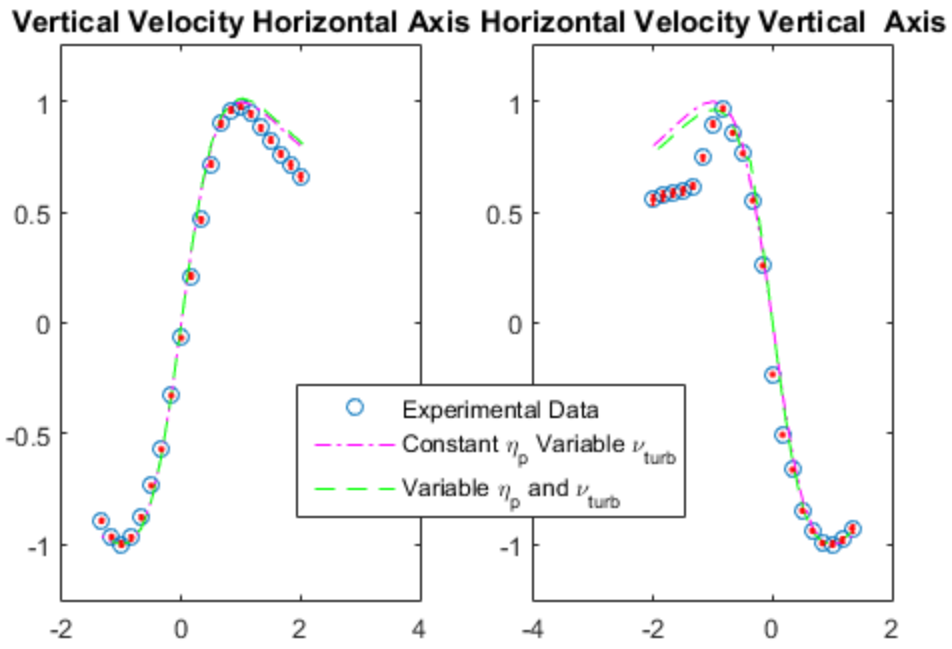

Figure 80 Comparison of the experimentally measured azimuthal velocity profiles to the profiles generated from the non-equilibrium pressure theory at 10.5 chord lengths downstream of the vortex generator and a tunnel speed of 40 m/s with uncertainty bars.

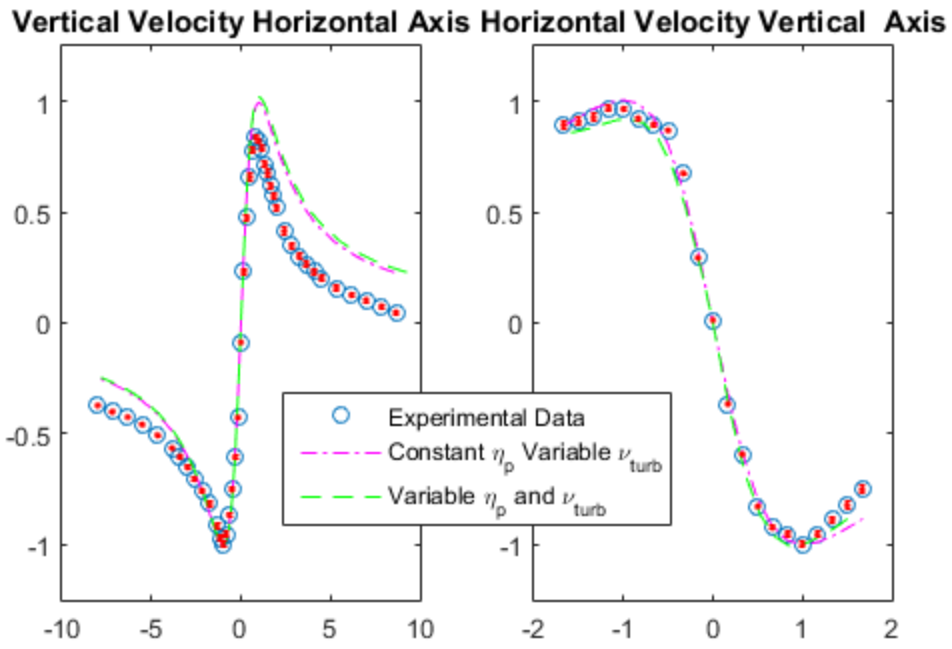

Figure 81 Comparison of the experimentally captured azimuthal velocity profiles to the profiles generated from the non-equilibrium pressure theory at 14 chord lengths downstream of the vortex generator and a tunnel speed 40 m/s with uncertainty bars.

Finally the experimental data and the theoretical profiles taking into account variable eddy viscosity and pressure relaxation was compared to Rankine vortex model and the Lamb-Ossen model.

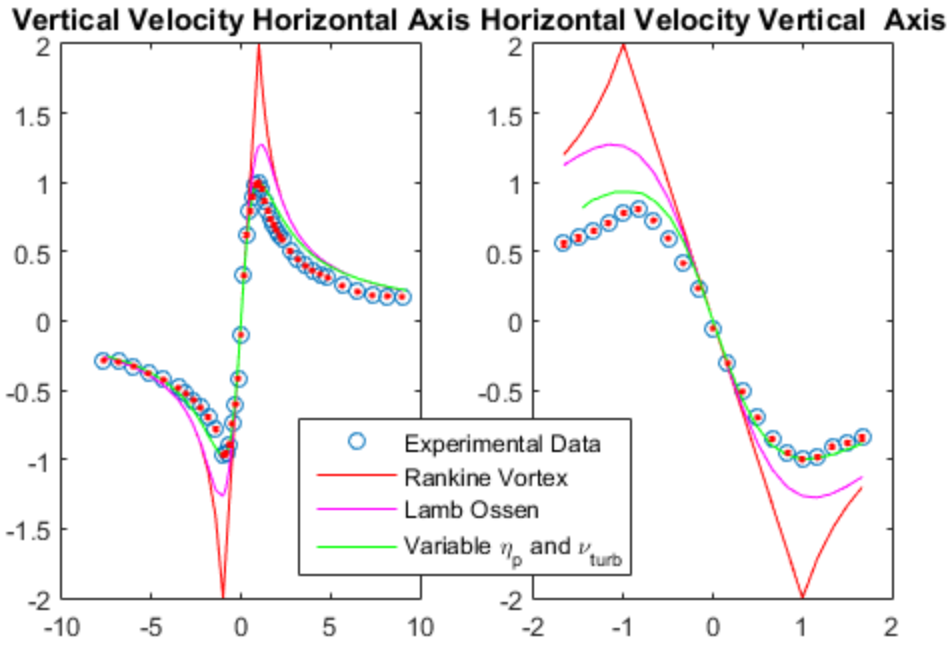

Figure 82 Comparison of experimental data and pressure relaxation model with historical models at 7 chord lengths and 30 m/s with uncertainty bars.

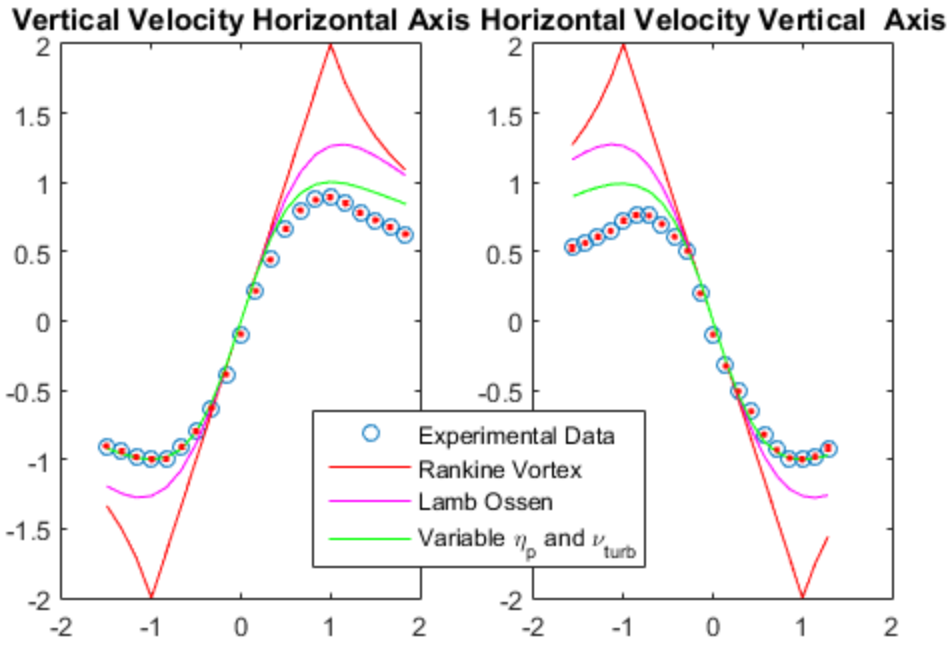

Figure 83 Comparison of experimental data and pressure relaxation model with historical models at 10.5 chord lengths and 30 m/s with uncertainty bars.

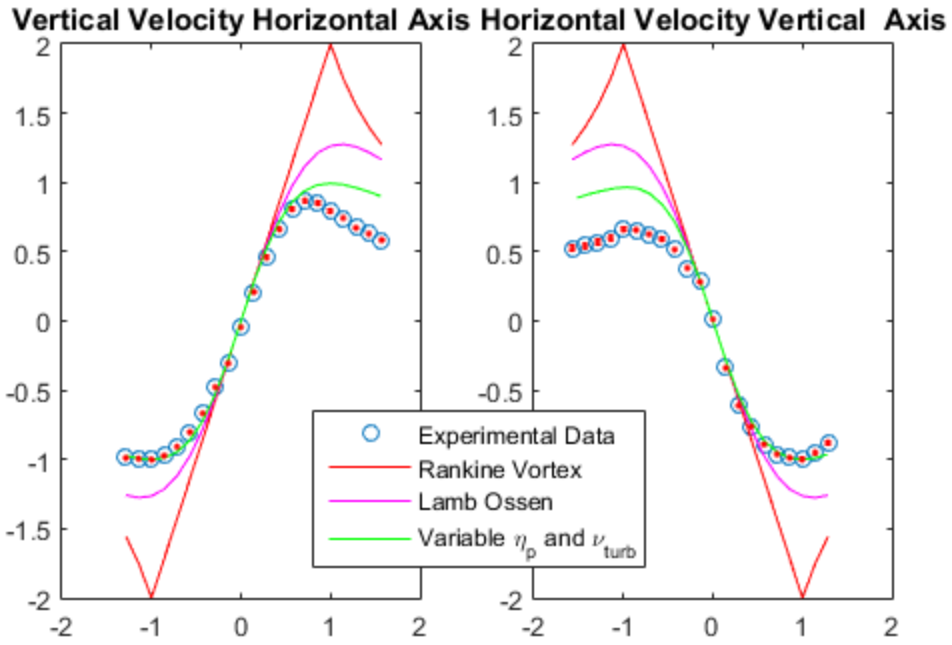

Figure 84 Comparison of experimental data and pressure relaxation model with historical models at 14 chord lengths and 30 m/s with uncertainty bars.

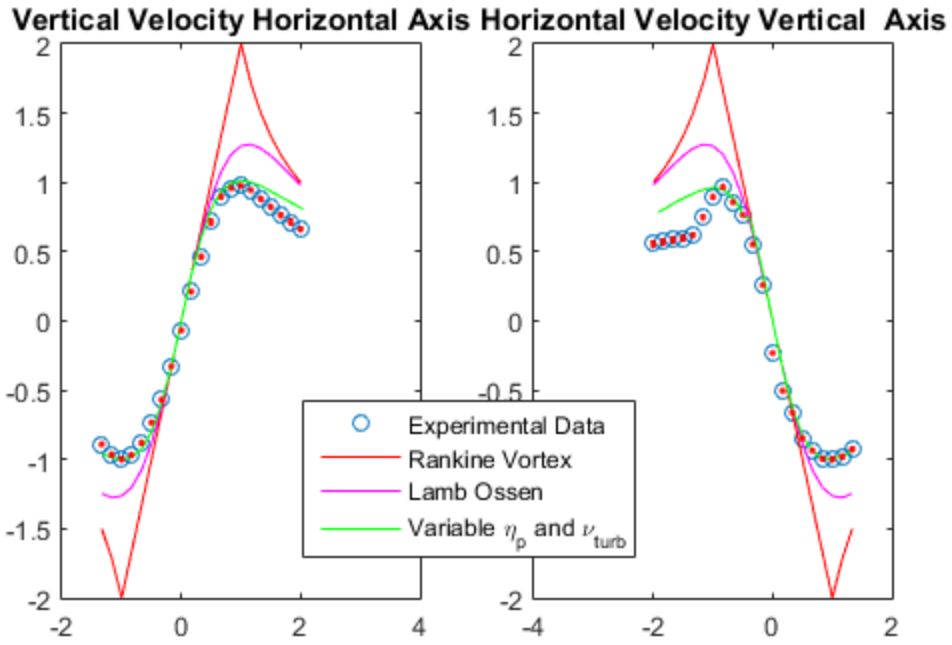

Figure 85 Comparison of experimental data and pressure relaxation model with historical models at 10.5 chord lengths and 40 m/s with uncertainty bars.

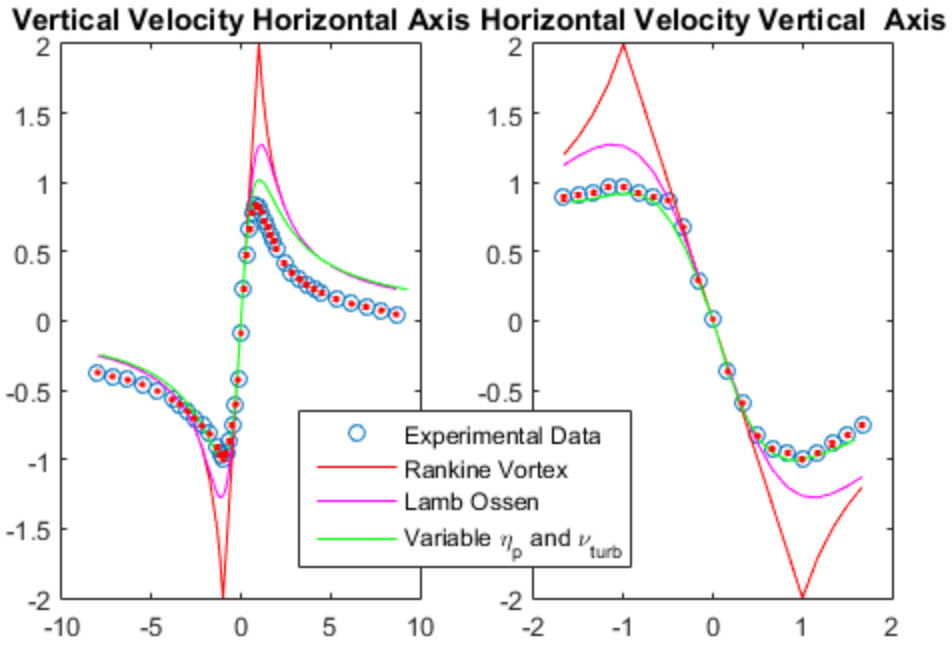

Figure 86 Comparison of experimental data and pressure relaxation model with historical models at 14 chord lengths and 40 m/s with uncertainty bars.

The pressure relaxation model is clearly in much better agreement with the experimental data than the historical models. The theoretical velocity profile that accounts for a variable pressure relaxation coefficient matches the hotwire data better than the profile that does not incorporate a changing pressure relaxation coefficient. It was easiest to see this at the location of the none-referenced peak in azimuthal velocity. The larger the difference in the pressure relaxation coefficient the larger the difference between the two peaks. In most cases the profile taking into account variable eddy viscosity and variable pressure relaxation fit the experimental hotwire data better, in the two cases where the theoretical profile accounting for the changing pressure relaxation coefficient was not a better fit, the pressure relaxation coefficient was small and had a

slightly lower magnitude at the location of the second peak in azimuthal velocity. This led to a profile that matched the shape of the data better but overestimated the magnitude of the peak.

An unusual anomaly was observed in the horizontal velocity survey shown in Figure 77. The mean velocity profile inside the vortex core was inconsistent with all of the other surveys. Interestingly, the adjusted theoretical profile accounting for changes in the pressure relaxation coefficient contains a similar jump. The jump in the experimental profile was associated with the largest observed change in the pressure relaxation coefficient between adjacent data points in any survey—the difference was .454 μs. That particular horizontal survey had a very large elapsed time interval between the "discontinuous" data points. This particular time interval was longer than usual because a circuit breaker tripped between measurements, requiring the tunnel to be restarted. The extended delay and the restarted wind tunnel state resulted in a much larger variation in temperature and relative humidity between data points.

If the opposite peak of the vortex varied from $v_{\theta,max}$ the theoretical model failed to predict this accurately. The model adjusted for variations in the pressure relaxation coefficient but assumed a constant circulation. The assumption of the constant circulation was possibly the cause of the errors on the opposite side of the vortex. This variation was likely caused by the small variance in tunnel set speed.

CHAPTER IV

CONCLUSIONS

This research has focused on characterizing experimentally the behavior of an axial vortex produced by a bi-wing vortex generator in a wind tunnel. The goal of the research was to employ an X-probe hot film anemometer to measure the mean, fluctuating and Reynolds stress velocity components characterizing the core region of an vortex. In addition, this research has attempted to explore and explain the remarkable agreement between the theoretical predictions of Ash, Zardadkhan and Zuckerwar (2011), predicting that a simple eddy viscosity turbulence model, combined with a pressure relaxation coefficient, estimated the vortex core diameter and maximum swirl velocity for this type of vortex accurately. A new bi-wing vortex generator was designed, fabricated and tested to determine optimal combinations of bi-wing angles-of-attack and wind tunnel speeds that produced large-diameter, stable vortices. Unlike a previous bi-wing design, the new generator did not have a center body, in order to minimize the axial velocity defect region along the vortex centerline.

This research demonstrated that a stable, axial vortex could be produced employing the new bi-wing generator, but the axial velocity defect was still observed in the core region, all the way to the downstream limit of the survey apparatus. The best combination of wind tunnel speed and bi-wing angles-of-attack, for producing a stable, relatively large core diameter vortex was ±12 degrees and 30 m/s. These experiments showed that the wing root vortices, shed between the two bi-wing elements had not fully merged at a distance of seven chord lengths behind the generator, at a wind tunnel test speed of 40 m/s.

The mineral oil smoke flow visualization approach for identifying promising test conditions was demonstrated successfully, enabling the hot film survey measurement grid to be planned and laid out in an optimal manner.

The vortex core size and its variation down the wind tunnel test section could be estimated effectively utilizing pixel counts across the dark core region. Unfortunately, it was not possible to relate the number of darkened pixels to a repeatable reference dimension. However, it was possible to visually determine the approximate location of the axis of rotation by maneuvering the hotwire support into the vortex while utilizing smoke illuminated with the laser sheet. Flow visualization also enabled the determination of which bi-wing configuration produced the largest most stable vortex. During streamwise flow visualization the influence of the hot film probe obstruction, on average, caused an estimated local vortex core dilation of less than 0.2 mm at 30 m/s and less than 0.4 mm at 40 m/s. The influence the probe support had on the vortex core was ascertained to be approximately a 0.8 mm dilation of the vortex at the point of interest.

Due to the nature of the X-probe geometry, and uncertainty in the exact location of the local center of rotation, it was necessary to measure the mean and fluctuating velocity components in Cartesian coordinates, then utilize the experimentally-defined rotational centerline to obtain vertical and horizontal velocity measurements along radial rays.

After the survey stations closest to the local mean center of rotation were identified, the mean and fluctuating azimuthal velocity components could be approximated by measuring the vertical or y-velocity component along the horizontal survey line passing nominally through the vortex center and the horizontal or x-velocity component along the vertical survey that passed

closest to the center of rotation. Originally, six survey sets were planned for the X-probe survey stations, at three streamwise locations (7, 10.5 and 14 bi-wing chord lengths), with wind tunnel velocities of 30 and 40 m/s. X-probe measurements taken at the wind tunnel test speed of 40 m/s, showed that a single axial vortex had not yet formed seven chord lengths behind the generator, and that survey was abandoned. The vortex centerline was not located at the exact center of the local wind tunnel cross section. This was probably due to the fact that the bi-wing junction was not located at the precise center of the wind tunnel cross section. However, the vortex centerline migrated toward the centerline of the tunnel as the vortex travelled downstream. The vortex cross section shape was observed to be more elliptical in shape than circular. This was believed to be caused by the geometry of the wind tunnel test section. This thesis demonstrated that the strain rates predicted using a simplified potential flow model indicated that non-equilibrium pressure forces can case the vortex core to have an elliptic shape. The closeness of top and bottom wind tunnel walls, compared with the side-to-side wall spacing, produced strain rate differences that produced different vertical and axial maximum strain rate locations, based on the non-equilibrium theory. . The nominal core diameters were observed to grow at a rate of about 2 mm per 1.5 chord lengths.

The axial velocity profiles displayed characteristic deficits caused by the wake of the vortex generator. The extent of the axial velocity deficit region was observed to extend out to radial distances greater than the core radius. At 1 core radius, jet-like axial velocity peaks that appeared to be periodic in nature were observed. At distances less than 1 core radius, this wake was intensified due to the nature of the vortex.

The radial velocity profiles required a mathematical correction to obtain approximant profiles due to the effects of high out-of-plane velocities and turbulence on an X-wire probe

when attempting to measure these velocities. In general due to this and the small magnitude of the radial velocities it was not possible to resolve repeatable radial velocities profiles. There is some evidence of a periodic phenomenon where the radial flow switches between an inflow and an outflow and back again. This is perhaps the gulping phenomena reported by Bandyopadhya et al (1991).

Turbulent kinetic energy was observed to be small outside of the core region. However, inside the core, the turbulent kinetic energy increased rapidly. This indicated that the most important turbulent effects occurred inside the core region.

The correlation of the "axial-radial" Reynolds stress was observed to be small at locations farther than two core radii from the axis, and grew in magnitude in proximity to the core boundary. The "axial-azimuthal" Reynolds stress was observed to follow similar trends with the "axial-radial" Reynolds stress. Although the measured Reynolds stress plots could not be directly related to the "radial-azimuthal" Reynolds stress, they were useful. They indicated that the Reynolds stresses are not important outside of the core region and the peak stress levels are observed in the vicinity of the core boundary.

The power spectral density plots indicated that the lower frequencies contained the most turbulent energy. It was also observed that the turbulent energy fell off sharply around 1000 Hz. Above a frequency of 10 kHz only electronic noise was observed confirming the visual observation of the instantaneous velocity data that there were no turbulent frequencies above 10 kHz.

One of the primary goals of this research was to determine whether non-equilibrium pressure forces can control axial vortex structure. It was useful to compare the experimental

profiles with the theory of Ash, Zardadkhan and Zuckerwar (2011). Since the pressure relaxation coefficient, η_p, and the kinematic viscosity were dependent on humidity and temperature, and both parameters changed continuously from measurement point to measurement point, it was necessary to adjust the estimated pressure relaxation values employing the equations generated by Ash, Zardadkhan and Zuckerwar (2011) to account for this. Three comparisons were made. First, it was assumed that temperature and kinematic viscosity and thus the pressure relaxation and eddy viscosity were constant throughout the survey, this profile correlated least well with the experimental data. Second, the pressure relaxation coefficient was assumed to be constant throughout the survey but the kinematic viscosity was allowed to vary, to account for changes in temperature and humidity. This theoretical profile showed better agreement with the measurements than the first. Third, the pressure relaxation coefficient and kinematic viscosity were adjusted for each data point. These profiles matched experimental data the best, indicating that pressure relaxation has a meaningful and measurable influence on the structure of an axial vortex. Further experimentation is required to confirm this and to indicate how to further advance the theory.

4.1 Recommendations for Future Work

More extensive experimentation is required to extend the results of this research. A longer wind tunnel test section than the existing low-speed facility at ODU, would be ideal, since it might be possible to obtain "fully-developed" axial vortex measurements with negligible axial wakes. In terms of existing facilities, the most important recommendation is that further study of the vortex structure employing velocity sensors that are capable of simultaneously acquiring all three unsteady components. At least three hot film sensor elements are required, and their physical size must be small enough to measure core structure. Hot film sensors can play a roll,

since local spectral data are important. On the other hand, if Particle Imagery Velocimetry or a similar technique is employed, the power spectral densities obtained in the present study can be useful in determining equipment sampling rates needed in order to capture data on the majority of the energy contained in the flow. If combined with three-sensor anemometer arrays, experiments should be capable of providing a much clearer picture. Future experiments should use a statistical approach to calibrating the hotwire instead of a one factor at a time of approach. This will greatly increase the accuracy of the calibration as well as simplify it from a two-step process to a single set of equations when accounting for temperature.

REFERENCES

Abuharaz, M.M.E, Ash, R.L. (2014) *State Variable Model for Unsteady Two Dimensional Axial Vortex Flow with Pressure Relaxation.* Norfolk: Old Dominion University Theses

ANSI StandardS1.26-1995(1995), *Methods for Calculation of the Absorption of Sound by the Atmosphere,* Standards Secretariat of the Acoustical Society of America, New York

Ash, R. L., Zardadkhan, I. and Zuckerwar, A.J. (2011), *The Influence of Pressure Relaxation on the Structure of an Axial Vortex*, Physics of Fluids 23(12)

Bandyopadhyay, P. R., Stead, D.J., and Ash, R.L.(1991), *Organized Nature of a Turbulent Trailing Vortex*. AIAA Journal, 29(10), 1627-1633

Brown, F.N.M. (1953), *A Photographic Technique for the mensuration and evaluation of aerodynamic patterns.* Photographic Engineering 4, 146-156

Bruun, H.H (1995), *Hot Wire Anemometry: Principles and Signal Analysis. Oxford: Oxford University Press*

Burnham, D. C., and Hallock, J. N. (1982). *Chicago monostatic acoustic vortex sensing system. Volume IV, Wake vortex decay.* National Technical Information Service, Alexandria VA.

Coleman, H. W., and Steele, W. G., (2009). *Experimentation, Validation and Uncertainty Analysis for Engineers.*

Delisi, D.P., Greene G.C., Robins, R.E., Vicroy,D.C., and Wang, F.Y. (2003) *Aircraft Wake Vortex Core Size Measurements.* Proceedings of the 21st AIAA Applied Aerodynamics Conference. John Wiley and Sons inc

Dryden, H.L, and Kuethe, A.M. (1929). *The measurement of fluctuations of air speed by the hot-wire anemometer*. National Bureau of Standards Report No. 320

Garodz, L.J., and Clawson, K.L., (1993) *Vortex wake Characteristics of B757-200 and B767-200 Aircraft using the tower fly-b technique.* NOAA Technical Memorandum ERL ARL

Graham, W.R., (1996) *Experimental Assessment of the Extended Betz Method for Wake Vortex Prediction*, Proceedings of the AGARD 78th Fluid Dynamics Panel Meeting and Symposium, Trondheim Norway

Lamb, H. (1932). *Hydrodynamics* (6th ed.). New York: Dover Publications.

Maltby, R.L., and Keating, R.F.A. (1962) a. *The Surface Oil Flow Technique for use in Low Speed Wind Tunnels.* AGARD-ograph 70, 29-38

Maltby, R.L., and Keating, R.F.A. (1962) b. *Smoke Techniques for use in low Speed Wind Tunnels.* AGARD-ograph 70, 87-109

McAlister K. W., and Takahashi R.K. (1991) *NACA 0015 Wing Pressure and Trailing Vortex Measurements*, NASA Technical Paper 3151 AVSCOM Technical Report 91-A-003

McCormick, B.W., Tangler, J.L. and Sherrier, H. E., (1968) *Structure of Trailing vortices,* Jornal of Aircraft 5,260

Merzkirch,W. (1974) *Flow Visualization.* New York: Academic Press

Merzkirch,W.(1979) *Making FluidFlows Visible.* American Scientist 67, 330-336

Merzkirch, W.(1987) *Technigues of Flow Visualization.* AGARD-ograph 302

Mueller, T.J. (1980). *On the Historical Development of Apparatus and Techniques for Smoke Visualization of Subsonic and Supersonic Flow*. AIAA paper 80

MTS.(2014). *Temposnics Magnetostrictive, Absolute, Non-contact Linear-Position Sensors G-series Models GP and GH Data Sheet*. North Carolina

MTS. (1989). *Temposonics Linear Displacement Transducer System with Analog Output Installation and Instruction Manual.* North Carolina

Hinze, J.O. (1975) *Turbulence*. New York: Mcgraw-Hill

Pope, S.B. (2000) *Turbulent Flows*. Cambridge: Cambridge University Press

Prandtl, L. (1925) *Bericht uber die Entstehung der Turbulenz.* Z. Angew. Math. Mech. 5, 136-139

Rankine, W. J. (1872). *A Manual of Applied Mechanics* (6th ed.). London: Charles Griffin and Company.

Romeos, A., Lemonis, G., Panidis, T., and Papailiou, D.D. (2009) , *Multisensor Hot Wire Vorticity Probe Measurements of the Formation Field of Two Corotating Vortices,* Flow Turbulence and Combustions, 83, 153-183

Romeos, A., and Panidis, T. (2010), *Co-Rotating Vortex Merging*, Symposium on Engineering Turbulence Modelling and Measurements

Settles, G.S., Teng, H.-Y. (1983) *Flow Visualization Methods for Separated Three-Dimensional Shock Wave/Turbulent Boundary Layer Interaction.* AIAA Journal, 21, 390-397

Shabbir, A., Beuther, P.D., George, W.K. (1995) *X-Wire Response in Turbulent Flows of High-Intensity Turbulence and Low Mean Velocities*. New York: Experimental Thermal and Fluid Science, 12, 52-56

Sinclair, P.C (1969) *The lower structure of dust devils*, Journal of Atmospheric Science, *30, 1599-1619*

Squire, H.B. (1965) *The Growth of a Vortex in Turbulent Flow*. Aeronautical Quarterly

Vukoslavcevic, P. Wallace, J. (2013), *Using Direct Numerical Simulation to Analyze and Improve Hot-wire Probe Sensor and Array Configurations for Simultaneous Measurement of the Velocity Vector and the Velocity Gradient Tensor.* Physics of Fluids 25(11)

Vita

MICHAEL P. THOMPSON

1117 Askham Drive • Cary, NC 27511
mthom114@odu.edu • 919-812-6836

EDUCATION

- Old Dominion University – Norfolk, VA
  Masters of Science Aerospace Engineering, (May 2016)

- Appalachian State University – Boone, NC
  Major: Physics | Minor: Mathmatics, (May 2012)

RELEVANT COURSE WORK

- *Graduate Course Work:* Turbulent Flows, Design of Experiments, Response Surface Methodology, Boundary Layer Theory, Advanced Classical Thermodynamics, Aerospace Propulsion, Flight Vehicle Aerodynamics, Fluid Mechanics, Continuum Mechanics
- *Undergraduate Course Work:* Classical Mechanics, Thermal Physics, Analog Electronics, Digital Electronics, Atmospheric Physics

SKILLS

- Leadership experience from organizing and completing Eagle Scout project.
- Experience using Matlab, Labview, Inventor, Design Expert, JMP, Rhinoceros, and PSpice
- Experience using Adobe Illustrator, Photoshop, and Indesign for conceptual design projects.
- Experience with Microsoft Word, Excel, and Power Point.

VOLUNTEER WORK

- *Eagle Scout Project*: Designed a shelf that had to span a 15-foot gap with no support other than the legs at the walls; planned and led the installation of shelf in a large walk-in closet.

AWARDS AND HONORS

- Eagle Scout
- Sigma Pi Sigma honor society of physics students
- Order of The Arrow